

# **US-APWR CONTAINMENT PERFORMANCE FOR PRESSURE LOADS**

**Non-proprietary Version**

**August 2013**

**©2013 Mitsubishi Heavy Industries, Ltd.  
All Rights Reserved**

**Revision History**

Revision	Page	Description
0	All	Original Issue
1	32	Added the response to RAI 764-5805 Rev. 0, Q.19-528; discussion on shear strain criteria
	36	Added the response to RAI 764-5805 Rev. 0, Q.19-527; the effect of tendon relaxation, concrete creep, concrete shrinkage, and anchorage losses.
	4, 5, 41-81	Added the response to RAI 764-5805 Rev. 0 Q.19-530; incorporate Results for Equipment Hatch Local Model.
	82	Added conclusion.
	83-92	Appendix A Added the response to RAI 764-5805 Rev. 0, Q.19-529 and RAI 490-3732 Q 03.08.01-2; Hydrogen Burn Pressure Integrity and pressure at first yield for liner, rebar, and tendons for Hydrogen Burn deterministic analysis.
	93-202	Appendix B Added the response to RAI 490-3732 Q03.08.01-4.
	203-213	Appendix C Added the response to RAI 433-3001 Q19-390.

© 2013

**MITSUBISHI HEAVY INDUSTRIES, LTD.**  
**All Rights Reserved**

This document has been prepared by Mitsubishi Heavy Industries, Ltd. (MHI) in connection with the U.S. Nuclear Regulatory Commission's (NRC) licensing review of MHI's US-APWR nuclear power plant design. No right to disclose, use or copy any of the information in this document, other than that by the NRC and its contractors in support of the licensing review of the US-APWR, is authorized without the express written permission of MHI.

This document contains technology information and intellectual property relating to the US-APWR and it is delivered to the NRC on the express condition that it not be disclosed, copied or reproduced in whole or in part, or used for the benefit of anyone other than MHI without the express written permission of MHI, except as set forth in the previous paragraph.

This document is protected by the laws of Japan, U.S. copyright law, international treaties and conventions, and the applicable laws of any country where it is being used.

Mitsubishi Heavy Industries, Ltd.  
16-5, Konan 2-chome, Minato-ku  
Tokyo 108-8215 Japan

## **Abstract**

The purpose of this technical report is to present the Containment Performance for Pressure Loads. The analyses described herein are provided to establish the fragility of the US-APWR primary containment system for over-pressurization. The fragility is calculated for 3 specified thermal conditions, namely, steady state normal operating temperatures, steady state conditions representing long term accident conditions, and transient thermal conditions for a representative hydrogen burning condition involving much higher temperatures but for much shorter durations. The deterministic analyses are also performed to estimate the pressure capability of the major penetrations. The containment pressure evaluation for more likely severe accident challenges described in RG 1.216 is addressed in this report.

## Table of Contents

<b>List of Tables</b>	<b>iii</b>
<b>List of Figures</b>	<b>iv</b>
<b>List of Acronyms</b>	<b>vi</b>
<b>1.0 SCOPE</b>	<b>1</b>
<b>2.0 APPLICABLE DOCUMENTS</b>	<b>2</b>
2.1 Project Documents	2
2.2 Codes and Standards	2
2.3 Reference Documents	2
<b>3.0 SUMMARY DESCRIPTION</b>	<b>4</b>
<b>4.0 ANALYSIS METHODS</b>	<b>9</b>
4.1 Finite Element Modeling	9
4.2 Loading Conditions	11
4.3 Probabilistic Assessment	11
4.4 Uncertainty in Parameter Variability	12
4.5 Uncertainty in Modeling and Processes	14
4.6 Thermal Conditions	17
4.7 Material Properties	22
4.8 Concrete Performance	28
4.9 Failure Criteria	32
<b>5.0 PRESTRESSED CONCRETE CONTAINMENT</b>	<b>35</b>
5.1 Model Description	35
5.2 Thermal Analyses	41
5.3 Median Capacity Analyses	45
5.4 Evaluation for Uncertainty	55
5.5 Fragility Summary	56
<b>6.0 EQUIPMENT HATCH</b>	<b>60</b>
6.1 Model Description	60
6.2 Thermal Analyses	63
6.3 Median Capacity Analyses	67
6.4 Evaluation for Uncertainty	78
6.5 Fragility Summary	79
<b>7.0 CONCLUSION</b>	<b>82</b>

**Appendices**

<b>APPENDIX A</b>	<b>Pressure Integrity for Hydrogen Generated Pressure Loads</b>	<b>83</b>
<b>APPENDIX B</b>	<b>Containment Performance for Pressure Loads for Containment Penetration</b>	<b>93</b>
<b>APPENDIX C</b>	<b>Containment Pressure Evaluation for More Likely Severe Accident Challenges</b>	<b>203</b>

## List of Tables

<u>Table No.</u>	<u>Title</u>	<u>Page</u>
Table 3-1	Summary of US-APWR Fragility for Over-Pressurization	5
Table 4-1	Summary of Variance for Modeling Uncertainty	15
Table 4-2	Summary of Temperature Conditions	18
Table 4-3	Temperature and Pressure in PCCV for Long Term Accident Thermal Condition	18
Table 4-4	Temperature and Pressure in PCCV for Hydrogen Burning Thermal Condition	19
Table 4-5	Film Coefficients for Thermal Conditions	19
Table 4-6	Summary of Thermal Material Properties	23
Table 4-7	Summary of Elastic Mechanical Properties for Steels	24
Table 4-8	Summary of Plastic Mechanical Properties for Steels	25
Table 4-9	Summary of Concrete Material Properties	26
Table 4-10	Summary of Material Limits and Failure Criteria	34
Table 5-1	Summary of Median Pressure Capacities	45
Table 5-2	Summary of Uncertainty Evaluations in Global Modeling	56
Table 5-3	Summary of Pressure Fragility from Global Modeling	57
Table 6-1	Summary of Median Pressure Capacities for Equipment Hatch	68
Table 6-2	Summary of Uncertainty Evaluations in EH Local Modeling	79
Table 6-3	Summary of Pressure Fragility from EH Local Modeling	80

## List of Figures

<u>Figure No.</u>	<u>Title</u>	<u>Page</u>
Figure 3-1	PCCV Pressure Fragility under Normal Operating Thermal Conditions	6
Figure 3-2	PCCV Pressure Fragility under Long Term Accident Thermal Conditions	6
Figure 3-3	PCCV Pressure Fragility under Hydrogen Burning Thermal Conditions	7
Figure 3-4	EH Pressure Fragility under Normal Operating Thermal Conditions	7
Figure 3-5	EH Pressure Fragility under Long Term Accident Thermal Conditions	8
Figure 3-6	EH Pressure Fragility under Hydrogen Burning Thermal Conditions	8
Figure 4-1	Calculation of Variance due to Modeling Uncertainty	16
Figure 4-2	Thermal Conditions on Exterior Surfaces of PCCV	20
Figure 4-3	Temperature and Pressure for Long Term Accident Condition	21
Figure 4-4	Temperature and Pressure for Hydrogen Burning Condition	21
Figure 4-5	Illustration of Stress-Strain Relations for A615 Grade 60 Rebar	27
Figure 4-6	Illustration of Stress-Strain Relations for A516 Grade 60 Liner Plate	28
Figure 4-7	Crack Initiation Criteria Curve	29
Figure 4-8	Shear Modulus Reduction for Open Cracks	30
Figure 4-9	Example of Shear Stress Capacity Across Open Cracks	30
Figure 4-10	Uniaxial Compressive Strength as Function of Temperature	31
Figure 5-1	Full 3-D Finite Element Modeling for Thermal Analysis	37
Figure 5-2	Full 3-D Finite Element Modeling for Stress Analysis	37
Figure 5-3	Illustration of Modeling for Tendons	38
Figure 5-4	Modeling of Reinforcement, Inside Axial Bars	39
Figure 5-5	Modeling of Reinforcement, Outside Axial Bars	39
Figure 5-6	Modeling of Reinforcement, Inside Hoop Bars	40
Figure 5-7	Modeling of Reinforcement, Outside Hoop Bars	40
Figure 5-8	Modeling of Reinforcement, Other Bars	41
Figure 5-9	Temperature Distribution for Normal Operating Condition	42
Figure 5-10	Temperature Distribution for Long Term Accident Condition	43
Figure 5-11	Temperature Distribution for Hydrogen Burning Condition	44
Figure 5-12	Accumulated Plastic Strain in Liner, Median Pressure Capacity for Long Term Accident Condition	46
Figure 5-13	Maximum Principal Concrete Strains, Median Pressure Capacity for Long Term Accident Condition	47
Figure 5-14	Accumulated Plastic Strain in Hoop Tendons, Median Pressure Capacity for Long Term Accident Condition	48
Figure 5-15	Accumulated Plastic Strain in Liner, Median Pressure Capacity for Normal Operating Condition	49
Figure 5-16	Maximum Principal Concrete Strains, Median Pressure Capacity for Normal Operating Condition	50

Figure 5-17	Accumulated Plastic Strain in Hoop Tendons, Median Pressure Capacity for Normal Operating Condition	51
Figure 5-18	Accumulated Plastic Strain in Liner, Median Pressure Capacity for Hydrogen Burning Condition	52
Figure 5-19	Maximum Principal Concrete Strains, Median Pressure Capacity for Hydrogen Burning Condition	53
Figure 5-20	Accumulated Plastic Strain in Hoop Tendons, Median Pressure Capacity for Hydrogen Burning Condition	54
Figure 5-21	Pressure Fragility with Temperature for PCCV Liner Tearing	58
Figure 5-22	Pressure Fragility with Temperature for PCCV Rebar Failure	58
Figure 5-23	Pressure Fragility with Temperature for PCCV Tendon Failure	59
Figure 5-24	Pressure Fragility with Temperature for PCCV Concrete Failure	59
Figure 6-1	Local Model of Equipment Hatch	61
Figure 6-2	Local Model of Equipment Hatch, Cut Section View	62
Figure 6-3	Local Model of Equipment Hatch, Close-up of Bolted Flange	62
Figure 6-4	Local Model of Equipment Hatch, Studs and Tendons	63
Figure 6-5	Temperature Distribution in EH Model for Normal Operating Condition	64
Figure 6-6	Temperature Distribution in EH Model for Long Term Accident Condition	65
Figure 6-7	Temperature Distribution in EH Model for Hydrogen Burning Condition	66
Figure 6-8	EH Concrete Cracking for Long Term Accident Conditions	69
Figure 6-9	EH Concrete Compressive Stress for Long Term Accident Conditions	70
Figure 6-10	EH Concrete Shear Strain for Long Term Accident Conditions	70
Figure 6-11	EH Liner Plastic Strains for Long Term Accident Conditions	71
Figure 6-12	EH Steel Plastic Strains for Long Term Accident Conditions	71
Figure 6-13	EH Tendon Plastic Strains for Long Term Accident Conditions	72
Figure 6-14	EH Concrete Cracking for Normal Operating Conditions	72
Figure 6-15	EH Concrete Compressive Stress for Normal Operating Conditions	73
Figure 6-16	EH Concrete Shear Strain for Normal Operating Conditions	73
Figure 6-17	EH Liner Plastic Strains for Normal Operating Conditions	74
Figure 6-18	EH Steel Plastic Strains for Normal Operating Conditions	74
Figure 6-19	EH Tendon Plastic Strains for Normal Operating Conditions	75
Figure 6-20	EH Concrete Cracking for Hydrogen Burning Conditions	75
Figure 6-21	EH Concrete Compressive Stress for Hydrogen Burning Conditions	76
Figure 6-22	EH Concrete Shear Strain for Hydrogen Burning Conditions	76
Figure 6-23	EH Liner Plastic Strains for Hydrogen Burning Conditions	77
Figure 6-24	EH Steel Plastic Strains for Hydrogen Burning Conditions	77
Figure 6-25	Pressure Fragility with Temperature for EH Rebar Failure	80
Figure 6-26	Pressure Fragility with Temperature for EH Sleeve Tearing	81
Figure 6-27	Pressure Fragility with Temperature for EH Cover Failure	81

## List of Acronyms

The following list defines the acronyms used in this document.

<b>3-D</b>	<b>three-dimensional</b>
<b>ACI</b>	<b>American Concrete Institute</b>
<b>AL</b>	<b>airlock</b>
<b>ASME</b>	<b>American Society of Mechanical Engineers</b>
<b>CCWS</b>	<b>component cooling water system</b>
<b>DCD</b>	<b>design control document</b>
<b>DV</b>	<b>depressurization valve</b>
<b>EH</b>	<b>equipment hatch</b>
<b>ESWS</b>	<b>essential service water system</b>
<b>FTT</b>	<b>fuel transfer tube</b>
<b>HC</b>	<b>high confidence</b>
<b>LOCA</b>	<b>loss of coolant accident</b>
<b>LOOP</b>	<b>loss of operation power</b>
<b>LTA</b>	<b>long term accident</b>
<b>NRC</b>	<b>U.S. Nuclear Regulatory Commission</b>
<b>PRA</b>	<b>probabilistic risk assessment</b>
<b>PCCV</b>	<b>prestressed concrete containment vessel</b>
<b>MS</b>	<b>main steam</b>
<b>RCP</b>	<b>reactor coolant pump</b>
<b>RCS</b>	<b>reactor coolant system</b>
<b>RG</b>	<b>regulatory guide</b>
<b>SNL</b>	<b>Sandia National Laboratories</b>

## 1.0 SCOPE

The analyses described herein are provided to establish the fragility of the US-APWR primary containment system for over-pressurization. Fragility is defined as the cumulative probability of failure for increasing internal pressure. Here, failure is taken to be a breach in the primary containment boundary, consisting of the steel lined Prestressed concrete containment vessel (PCCV) walls and the operable penetrations, such as personnel airlocks (ALs) and equipment hatch (EH). Sufficient test evidence and experience exists to exclude the fixed penetrations, such as electrical, feed water, and steam lines, as the limiting components in the pressure capacity. A breach in the boundary can be caused from tearing of the steel liner, flange distortion at the bolted connections, tearing of the steel components in the penetrations, loss of anchorage for the penetrations, or a structural failure of the concrete walls away from the penetrations. Because excessive internal pressure is related to extreme accident conditions, this fragility is also a function of elevated temperatures, which develop in tandem with increasing pressure. The fragility is calculated for 3 specified thermal conditions, namely, steady state normal operating temperatures, steady state conditions representing long term accident (LTA) conditions, and transient thermal conditions for a hydrogen burning condition as representative of a severe accident involving much higher temperatures but for much shorter durations. This range of fragility with temperature can then be coupled in the probabilistic risk assessment with the hazard rates for the probabilities that these thermal conditions and the associated pressure levels will occur during the life of the plant.

The probabilistic based pressure fragility analyses employ both a global model of the complete PCCV and a local model of the EH. The global PCCV model is used to determine pressure capacity due to global response of the PCCV structural system, and the local EH model is used to identify limiting pressure capacities associated with the EH components using more detailed modeling of these components. For example, the global model includes the EH penetration but does not include the EH cover while the EH local model includes the cover, the closure bolts, and mating flanges as well as more refined meshing for the EH components. The local EH model uses boundary conditions extracted from the global model to impose the global deformation response on the local model.

A deterministic analysis is performed to demonstrate that the pressure capability of the steel lined prestressed concrete boundary of the containment system meets the regulatory requirements in 10CFR50.44(c)(5) per Draft Regulatory Guide DG-1203. This analysis, as discussed in Appendix A, is based on the same global model used in the fragility analyses for consistency in establishing pressure capacities.

In addition, deterministic analyses are performed to estimate the pressure capability of the major penetrations (i.e., AL, Main Steam (MS) and Feedwater (FW) piping penetrations and fuel transfer tube (FTT) penetration) per Regulatory Guide 1.216. These analyses are discussed in Appendix B.

Regulatory Guide 1.216 describes the methods that the U.S. Nuclear Regulatory Commission (NRC) staff considers acceptable for predicting the internal pressure capacity for containment structures above the design-basis accident pressure. Appendix C provides the containment pressure evaluation results to satisfy the NRC staff's specification described in Regulatory Guide 1.216.

## 2.0 APPLICABLE DOCUMENTS

### 2.1 Project Documents

- 2.1.1 Design Control Document for US-APWR, Chapter 3, Design of Structures, Systems, Components and Equipment, MUAP-DC003, Revision 3, March 2011.
- 2.1.2 Equipment Hatch Design Report, N0-FH00208 Rev.4 November 2010
- 2.1.3 Pressure and Thermal Conditions for Draft Technical Report of PCCV Ultimate Pressure Capacity, MHI Drawing 4DS-UAP-20100038, Revision 1, 2013.

### 2.2 Codes and Standards

- 2.2.1 ASME 2001 through 2003 addenda: Boiler and Pressure Vessel Code, Section III – Rules for Construction of Nuclear Power Plant Components, Division 2 – Code for Concrete Reactor Vessels and Containments, Subsection CC- Concrete Containments, Article CC 3000 – Design.
- 2.2.2 ASME 2001 through 2003 addenda: Boiler and Pressure Vessel Code, Section II, Part A – Ferrous Material Specifications.
- 2.2.3 ACI 349-06, Code Requirements for Nuclear Safety Related Concrete Structures.
- 2.2.4 ASME 2001 through 2003 addenda: Boiler and Pressure Vessel Code, Section III – Rules for Construction of Nuclear Power Plant Components, Division 1 – Subsection NE – Class MC Components.

### 2.3 Reference Documents

- 2.3.1 ABAQUS/Standard, Version 6.9, Dassault Systemes Simulia Corp., Providence, RI.
- 2.3.2 ANACAP-U, Version 2.5, Theory Manual, ANA-QA-145, ANATECH Corp., San Diego, CA, 1998.
- 2.3.3 Rodabaugh, E. C., and Desai, K. D., “Realistic Seismic Design Margins of Pumps, Valves, and Piping,” NUREG/CR-2137, USNRC, Washington, DC, June 1981.
- 2.3.4 Chu, T. Y., Pilch, M. M., et. al., “Lower Head Failure Experiments and Analyses,” NUREG/CR-5582, USNRC, Washington, DC, February 1999.
- 2.3.5 Brister, P. M., “Code Design Criteria in the USA, Evaluation of Strength Properties,” Proceedings of the 3rd International Conference on Pressure Vessel Technology, Tokyo, Japan, April 18-22, 1977.
- 2.3.6 Luecke, W. E., et. al., “Mechanical Properties of Structural Steels,” NIST NCSTARR 1-3D, Federal Building and Fire Safety Investigation of the World Trade Center Disaster, National Institute of Standards and Technology, Washington, DC, September 2005.
- 2.3.7 Bournonville, M., Dahnke, J., and Darwin, D., “Statistical Analysis of the Mechanical Properties and Weight of Reinforcing Bars,” Report SL 04-1, Structural Engineering and Engineering Mechanics, University of Kansas, December 2004.
- 2.3.8 Specification Sheets for PC Strand to ASTM A416, Sumiden Wire Products Corporation (SWPC), Stockton, CA.

- 2.3.9 Freskakis, G. H., "State-of-the-Art Report on High Temperature Concrete Design," Burns and Roe, Inc., Oradell, NJ, for U. S. Department of Energy, DOE/CH/94000-1, November 1985.
- 2.3.10 James, R. J., Rashid, Y. R., Liu, A. S., and Gou, B., "Fragility Analysis for the Pressure Capacity of ESBWR Primary Containment System," Proceedings of the 2007 International Congress on Advances in Nuclear Power Plants, ICAPP07, Nice, France, May 13-18, 2007.
- 2.3.11 James, R. J., Zhang, L., Rashid, Y. R., "Impact of High Velocity Objects into Concrete Structures – Methodology and Application," Proceedings of ASME International Mechanical Engineering Congress and Exposition, Washington, D. C., November, 2003.
- 2.3.12 James, R. J. and Rashid, Y. R., "Severe Impact Dynamics of Reinforced Concrete Structures," Sixth European Conference on Structural Dynamics, Paris, France, September, 2005.
- 2.3.13 James, R. J., Zhang, L., Rashid, Y. R., Cherry, J. L., "Seismic Analysis of a Prestressed Concrete Containment Vessel Model," NUREG/CR-6639, U. S. Nuclear Regulatory Commission, Washington, D. C., August 1999.
- 2.3.14 James, R. J., Zhang, L., Rashid, Y. R., Cherry, J. L., "Seismic Analysis of a Reinforced Concrete Containment Vessel," NUREG/CR-6707, U. S. Nuclear Regulatory Commission, Washington, D. C., August 1999.
- 2.3.15 Dameron, R. A., Dunham, R. S., Rashid, Y. R., Sullaway, M. F., "Criteria and Guidelines for Predicting Concrete Containment Leakage," Fourth Workshop on Containment Integrity, Sponsored by USNRC, Arlington, VA, June 1988.
- 2.3.16 Pfeiffer, P. A., Kennedy, J. M., and Marchertas, A. H., "Thermal Effects in Concrete Containment Analysis," NUREG/CP-0095, and Fourth Workshop on Containment Integrity, Sponsored by USNRC, Arlington, VA, June 1988.
- 2.3.17 Dameron, R. A., Zhang, L., Rashid, Y. R., Vargas, M. S., "Pretest Analysis of a 1:4-Scale Prestressed Concrete Containment Vessel Model," NUREG/CR-6685, U. S. Nuclear Regulatory Commission, Washington, D. C., October 2000.
- 2.3.18 Dameron, R. A., Hansen, B. E., Parker, D. R., Rashid, Y. R., "Posttest Analysis of the NUPEC/NRC 1:4-Scale Prestressed Concrete Containment Vessel Model," NUREG/CR-6809, U. S. Nuclear Regulatory Commission, Washington, D. C., February 2003.
- 2.3.19 Ang, A. H-S. and Tang, W. H., Probability Concepts in Engineering, Emphasis on Applications to Civil and Environmental Engineering, John Wiley & Sons Inc., New Jersey, 2007.
- 2.3.20 Draft Regulatory Guide, DG-1203 "Containment Performance for Pressure Loads", U. S. Nuclear Regulatory Commission, December 2008.
- 2.3.21 "Nonlinear, Incremental Structural Analysis of Massive Concrete Structures", ETL 1110-2-365, U. S. Army Corps of Engineers, Department of the Army, Washington, DC, August 1994.

### 3.0 SUMMARY DESCRIPTION

The fragility of the US-APWR primary containment system to over-pressurization under accident conditions is summarized in Table 3-1. This table provides the median value and a 95% high confidence (HC) value for the failure pressures causing the various failure modes that lead to a breach in the containment boundary. The first 4 failure modes and corresponding pressure capacities are determined from the global PCCV modeling, and the last 3 failure modes and corresponding pressure capacities are determined in the local EH modeling. The limiting pressure capacities for each temperature condition are highlighted in yellow. Figures 3-1, 3-2, and 3-3 plot the fragilities for these failure modes for the global PCCV for normal operating, LTA, and hydrogen burning thermal conditions, respectively. Figures 3-4, 3-5, and 3-6 plot the fragilities for the failure modes associated with the EH for normal operating, LTA, and hydrogen burning thermal conditions, respectively.

The analyses indicate that for all three temperature conditions, the pressure capacity is limited by liner tearing, which is found to first initiate at the transition to the thickened concrete section or at the rebar transition region for the EH. The expected or median pressure to initiate tearing is found to be 223.6 psig or 3.29 times the design pressure ( $P_d$ ) of 68 psig for the steady state thermal conditions associated with a LTA condition. This limitation in pressure capacity due to liner tearing is consistent with the  $\frac{1}{4}$  scale PCCV tests performed at Sandia National Labs, References 2.3.17 and 2.3.18. The 95% confidence value for liner tearing under long term accident conditions is determined to be 176 psig or  $2.59 \cdot P_d$  in these analyses. A slightly lower pressure of 171 psig ( $2.51 \cdot P_d$ ) is found for the 95% confidence value for rebar failure around the EH. Here the median pressure capacity is 237.4 psig ( $3.49 \cdot P_d$ ) but this failure mode has more uncertainty than that for liner tearing. However, this failure develops in the local reinforcement on the outside surface of the PCCV around the EH. Because of the ductility available from the extra reinforcement around the EH, a sudden failure of the PCCV or EH due to rupture of the outer local reinforcing bar is not indicated in the analysis, and thus leakage is not immediate, but will develop at somewhat higher pressure when the liner plate on the inside surface tears. The local EH model indicates that local liner tearing around the EH will not develop before the PCCV liner tearing, and thus it is concluded that the PCCV liner tearing would be the limiting pressure capacity near the 95% value (176 psig) determined for that failure mode.

For ultimate capacity based on rebar and tendon rupture, the median pressure capacity for long term design accident conditions is found to be 243.6 psig or  $3.58 \cdot P_d$ . It is also determined that the ultimate capacity is not limited by the concrete strength. These results are again consistent with the Sandia National Laboratories (SNL) test for the  $\frac{1}{4}$  scale PCCV model. These analyses also indicate that the ultimate capacity does not strongly depend on temperature. The median ultimate capacity at normal operating temperature is determined to be  $3.65 \cdot P_d$  and the median ultimate capacity under hydrogen burning conditions is  $3.64 \cdot P_d$ .

**Table 3-1 Summary of US-APWR Fragility for Over-Pressurization**

Failure Mode	Failure Pressure Pressure (psig) Followed by Factor on P <sub>d</sub>					
	Normal Operating Conditions		Long Term Accident Conditions		Hydrogen Burning Conditions	
	Median	95%HC	Median	95%HC	Median	95%HC
PCCV Liner Tearing	230.0	184.9	223.6	176.0	237.7	183.1
	3.38	2.72	3.29	2.59	3.50	2.69
PCCV Rebar Rupture	250.0	195.9	243.6	187.2	247.7	186.6
	3.68	2.88	3.58	2.75	3.64	2.74
PCCV Tendon Rupture	248.0	200.0	246.0	194.2	249.0	192.3
	3.65	2.94	3.62	2.86	3.66	2.83
PCCV Concrete	252.0	203.7	255.6	202.2	253.7	196.4
	3.71	3.00	3.76	2.97	3.73	2.89
EH Rebar Failure	236.8	173.2	237.4	171.0	240.4	170.3
	3.48	2.55	3.49	2.51	3.54	2.50
EH Sleeve Tearing	263.0	202.5	251.0	189.7	262.0	194.3
	3.87	2.98	3.69	2.79	3.85	2.86
EH Cover Failure	263.0	201.7	252.0	189.8	260	192.2
	3.87	2.97	3.71	2.79	3.82	2.83

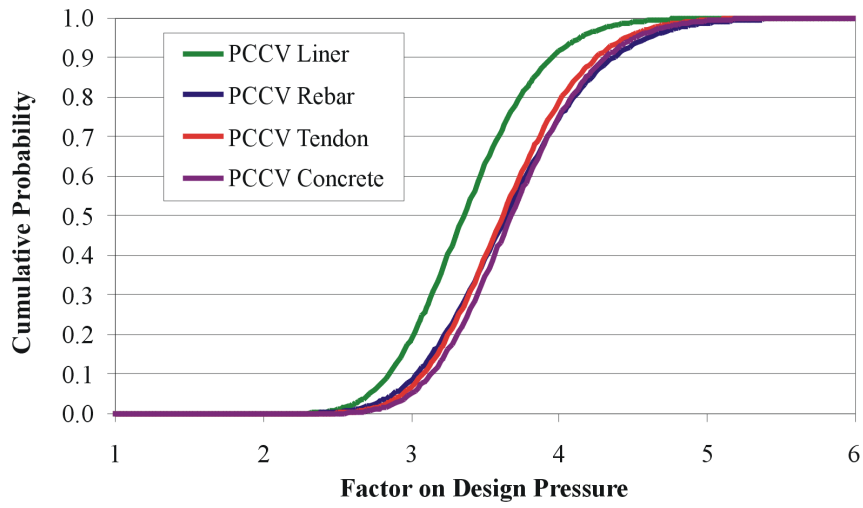


**Figure 3-1 PCCV Pressure Fragility under Normal Operating Thermal Conditions**

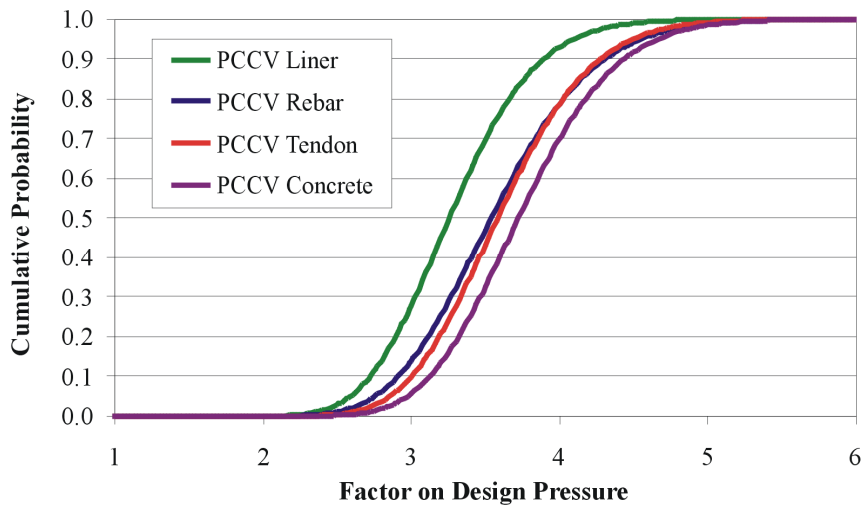


**Figure 3-2 PCCV Pressure Fragility under Long Term Accident Thermal Conditions**

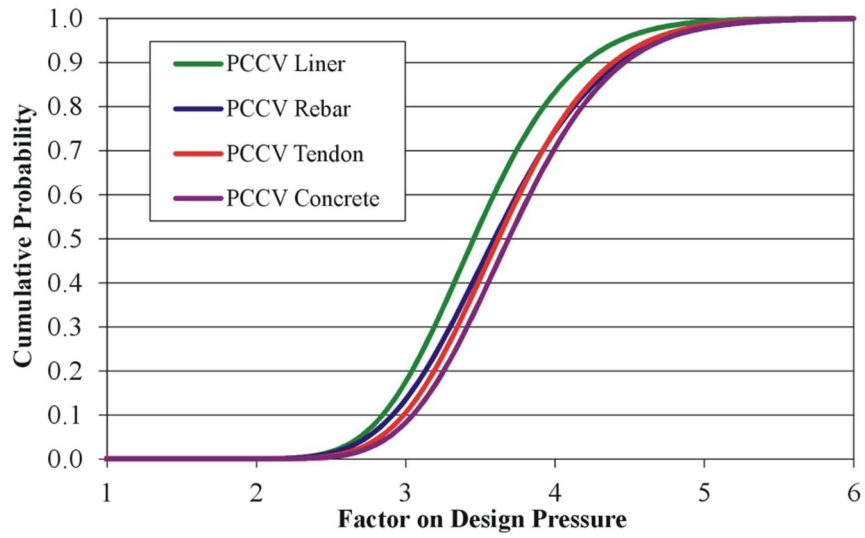


Figure 3-3 PCCV Pressure Fragility under Hydrogen Burning Thermal Conditions

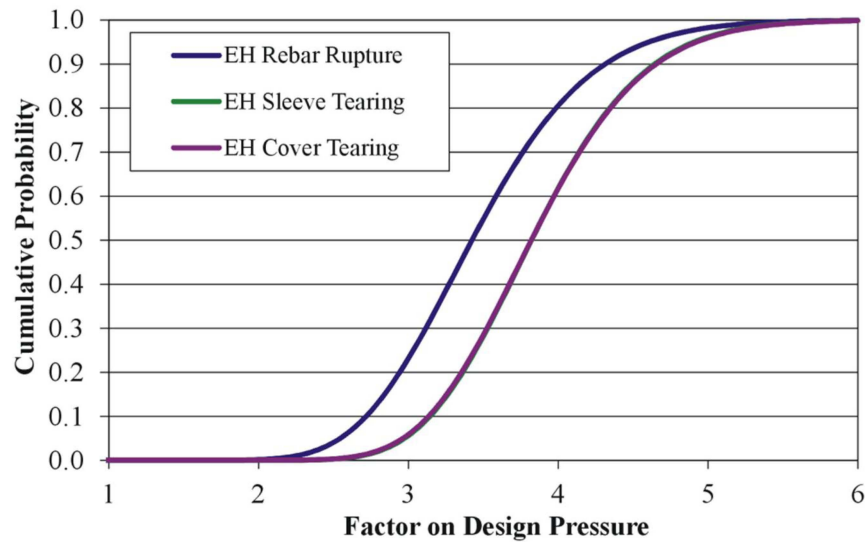


Figure 3-4 EH Pressure Fragility under Normal Operating Thermal Conditions

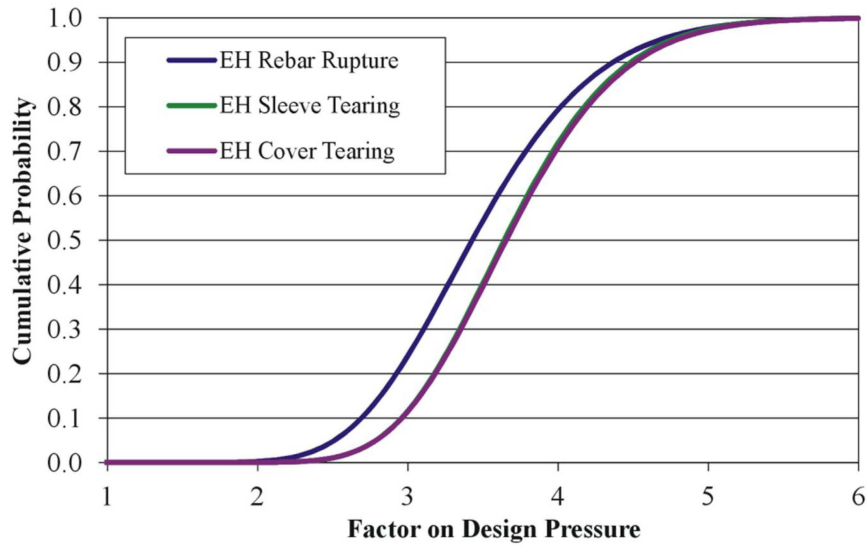


Figure 3-5 EH Pressure Fragility under Long Term Accident Thermal Conditions

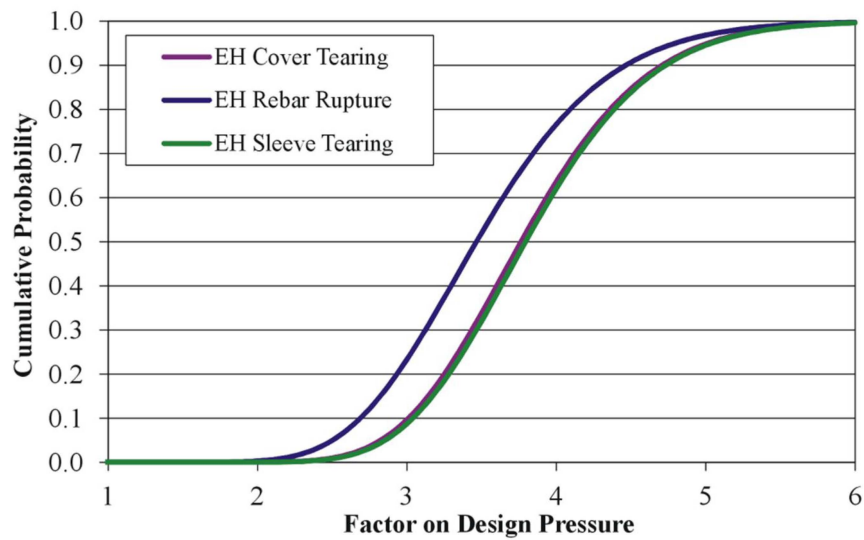


Figure 3-6 EH Pressure Fragility under Hydrogen Burning Thermal Conditions

## 4.0 ANALYSIS METHODS

These analyses use the ABAQUS/Standard finite element computer program, Reference 2.3.1, coupled with the ANACAP-U concrete constitutive model, Reference 2.3.2. This software has been used in similar previous work for reinforced concrete containments, Reference 2.3.10.

The geometry and configurations used in the analyses are based on References 2.1.1 and 2.1.2. These analyses are based on detailed three dimensional (3-D) finite element modeling, advanced material constitutive relations including material degradation with temperature, and an assessment of uncertainties within a probabilistic framework. The uncertainties in the analysis results are associated with the finite element modeling (such as mesh fidelity and constitutive modeling), material properties of the in-situ structure at the time of the over-pressurization, failure criteria or limit states used in establishing pressure capacity, and loading conditions that lead to pressurization of the containment. The uncertainties are evaluated by first identifying those parameters that are likely to have a significant effect on the analysis results and then evaluating the effect of variations in these parameters using the 95% confidence value of the specific parameter while keeping all other parameters at the median values. In some cases, such as material property variations, additional analytical calculations are needed to evaluate the uncertainty. In other cases, such as variation in failure criteria, re-evaluation of existing analyses can be performed. By assuming that the structural response is best characterized by a lognormal probability density function for variations in these parameters (as allowed in DG-1203, Reference 2.3.20), the standard deviation or variance for the lognormal distribution for each important parameter is determined. The overall variance is determined by using a square root of the sum of the squares combination of the lognormal deviations for the individual parameters. Having the median value and lognormal deviation for the pressure capacity, a cumulative probability of failure for increasing pressure is established by integrating the lognormal probability density function.

Accident conditions leading to over-pressurization will also include elevated temperatures. Because of thermal induced stresses and material property degradation at elevated temperatures, the fragility for over-pressurization is also a function of temperature. Thus, the fragility analyses are conducted for three different thermal conditions, 1) normal operating steady state conditions, 2) a LTA condition, and 3) a severe accident condition. For the LTA condition, the temperature distribution is based on a steady state condition where the PCCV atmosphere has reached 438 °F over about 120 hours representative of a bounding loss of coolant accident (LOCA) event. For the severe accident condition, the temperature distribution for the pressure capacity is based on a transient thermal condition using a snapshot of the temperatures when the PCCV liner reaches 1000 °F in a few seconds due to a hydrogen burn scenario. These thermal conditions are described in more detail in Section 4.6 below.

### 4.1 Finite Element Modeling

Failure of the containment is defined here as a breach in the containment boundary, which can occur as a result of structural failure in the PCCV walls, liner tearing at discontinuities, such as anchorages or thickened plates at penetrations, tearing in the steel components of the penetrations, or due to distortion of the bolted flanges in the closure connections of the operable penetrations. A global, 3-D finite element model is used to determine the pressure capacity of the PCCV structure assuming no leakage or failure in the steel penetration components. Previous work and experimental data, References 2.3.17 and 2.3.18, indicate

that liner tearing will likely constitute the limiting component for pressure capacity in the primary containment system.

A full 3-D global model is used as the basis for establishing the pressure capacity of the PCCV under global structural response. Because of the EH and other penetrations with thickened concrete sections, the containment structure does not have a true plane of symmetry. The thermal conditions leading to over-pressurization are also not symmetric around the containment due to partial coverage of the PCCV by the reactor building. The model is free standing and includes a portion of the basemat for anchoring the axial tendons. Continuum (solid) elements with embedded truss-like sub-elements for the reinforcement are used for the reinforced concrete sections. Truss elements with appropriate constraints to the concrete are used for the axial and hoop tendons. Plate elements are used for the steel liners and the penetration sleeves. In this global model, these liner elements are “glued” to the concrete surfaces without explicitly modeling the anchorage system. The global model includes representations for the EH and personnel AL penetrations, but the global analysis is performed assuming that leakage does not occur in these components.

A local 3-D model of the EH and the PCCV wall around the EH is used to identify pressure capacities that are limited by the local performance of EH components using more detailed modeling of these components. For example, the global model includes the EH penetration but does not include the EH cover while the EH local model includes the cover, the closure bolts, and mating flanges as well as more refined meshing for the EH components. The local EH model uses boundary conditions extracted from the global model to impose the global deformation response on the local model.

Each analysis requires a thermal and a stress version of the model. The thermal model is used to determine the temperature distribution within the structure for each of the 3 thermal conditions, and the stress model is used to determine the pressure capacity based on the temperature distribution of interest and the combinations of the other parameter values. The temperature distributions are assumed to be independent of the stress solution, that is, the temperatures do not depend on displacements. The thermal analyses use bi-linear 8-node brick elements to avoid convergence issues associated with bi-quadratic elements and the implicit formulation used in the thermal solution. Steady state temperature solutions are used for the normal operating and LTA cases. A transient thermal solution is used for the hydrogen burning case with the initial conditions set to the steady state operating conditions. The appropriate temperature distribution is then transferred to the stress model, and the internal pressure is incrementally increased to find the failure pressure with that temperature distribution. The stress analyses use bi-quadratic (20-node) brick elements with reduced Gaussian quadrature integration. From past experience, these elements perform the best for concrete cracking analyses for a given level of mesh refinement or nodal degrees of freedom. Thus, the thermal analyses use models with 8 times as many elements, where each 20-node, quadratic element is divided into eight 8-node linear elements. The temperature distributions at the nodes for the specified time points are read into the stress analysis from the thermal models. The stress analysis is based on static equilibrium, ignoring inertia effects. At each of the load increments for increasing internal pressure, equilibrium iterations are used to redistribute the loads and section stresses as cracking develops. The stress analyses are then evaluated per the failure criteria described in Section 4.9 below to establish the failure pressure.

## 4.2 Loading Conditions

The analyses are performed by initializing the stress solution to be stress free at a uniform ambient temperature of 70 °F (21.1 °C) and then applying gravity loads and tendon prestressing. A thermal analysis (either steady state or transient, as appropriate) is performed to establish the temperature distributions within the structure for each particular thermal condition. The temperature distribution and pressures corresponding to that temperature condition are then incrementally applied to the stress model. Finally, the internal pressure is then slowly increased with static equilibrium iterations, holding the temperature distribution constant, to determine the pressure at which failure or leakage occurs for that thermal condition and combination of material and parameter values.

## 4.3 Probabilistic Assessment

The analytical procedure used to develop the fragility, defined as the cumulative probability of failure for increasing pressure, for the various temperature conditions is summarized as follows.

1. Determine the pressure capacity ( $P_m$ ) using median values of all material properties and other conditions having significant influence on the structural capacity. This requires definition of various failure criteria or limit states, such as rupture strain in rebar or shear strain across concrete sections, as discussed in Section 4.9. This median pressure capacity will also use the median values for these failure criteria.
2. For all material or structural limit states used as failure criteria in judging the ultimate pressure capacity, a median value of the limit state and a value having a 1.645 standard deviation (95% confidence level for the value) are defined. For each of these failure criteria, the pressure capacity is evaluated using the 95% confidence value together with the median values for all other failure conditions. The logarithmic standard deviation for the pressure capacity due to variation in the failure criteria is then calculated as,

$$\beta_f^i = \frac{\text{Ln}(P_f^i / P_m)}{-1.645}$$

where  $P_f^i$  is the pressure capacity when evaluated using the 95% confidence value for the  $i^{\text{th}}$  failure criteria. The assumptions are that the natural logarithm of the failure pressure has a normal distribution for variations in the parameters, and that all the parameters considered are independent of each other. Note that several values of  $P_m$  are calculated in Step 1 corresponding to different failure modes or limit states of various components. The appropriate median pressure associated with the capacity for the failure criteria under evaluation is used to determine the standard deviation for that parameter.

3. For all material properties having significant influence on the structural pressure capacity, a median and 95% confidence value are defined. These parameters are discussed further in Section 4.4 below. An additional analysis with the appropriate model is performed for each of these parameters using the 95% confidence value for the parameter under consideration and with median values for all other parameters, including the failure criteria. The logarithmic standard deviation for the pressure capacity due to variation in these parameters is then calculated as,

$$\beta_s^i = \frac{\ln(P_s^i / P_m)}{-1.645}$$

where  $P_s^i$  is the pressure capacity when evaluated using the 95% confidence value for the  $i^{\text{th}}$  parameter or material property. Again the median failure pressure associated with the parameter under investigation is used in this equation.

4. Assign a logarithmic standard deviation for the pressure capacity due to modeling uncertainties ( $\beta_m$ ), including such things as mesh refinement, constitutive modeling, geometric tolerances, and manufacturing/construction imperfections. This variance for uncertainty is developed using comparisons of analytical predictions to test data results using similar modeling techniques from past work. This is discussed further in Section 4.5 below.
5. Calculate a composite lognormal standard deviation for the pressure capacity as the square root of the sum of the squares of all individual standard deviations, as

$$\beta = \sqrt{\sum (\beta_f^i)^2 + \sum (\beta_s^i)^2 + \beta_m^2}$$

6. Steps 1-5 are performed only for the “median” temperature condition, identified as the steady state LTA case. The lognormal standard deviations so computed are then used in evaluating the fragility for the other temperature cases. The median pressure capacity for the other temperature cases is calculated using the median values of all parameters but under the temperature distributions corresponding to the temperature condition specified. The assumption here is that the uncertainty in the analyses does not change significantly for the different thermal conditions. Only the median pressure capacity is significantly affected by the temperature condition. This is to bring the computational effort in line with the level of effort needed for the scope of the project.
7. The fragility will be based on a lognormal probability density function (Reference 2.3.19) for the failure pressure defined as

$$p_f(p) = \frac{1}{p\beta\sqrt{2\pi}} \exp\left[-\frac{1}{2}\left(\frac{\ln(p/P_m)}{\beta}\right)^2\right] \text{ for } p > 0, \text{ and } p_f(p) = 0 \text{ otherwise,}$$

where  $p$  is the failure pressure,  $P_m$  is the mean value of failure pressure, and  $\beta^2$  is the variance of the normally distributed natural log of  $p$ . The cumulative probability or fragility is determined from integration of the probability density function, so that the probability that the failure pressure is less than  $\bar{P}$  is defined by

$$P = \int_0^{\bar{P}} p_f(p) dp$$

#### 4.4 Uncertainty in Parameter Variability

To address aleatory uncertainty associated with variability of parameters for which a range of values can be determined, variations in key analysis parameters are considered. The following parameters are identified as significant in affecting the calculated structural capacity for internal pressure and requiring an evaluation of the uncertainty involved.

- $f'_c$  Concrete compressive strength. This also affects the concrete stiffness (modulus), shear performance, and cracking characteristics. This is deemed an important material variable in determining the pressure capacity of the PCCV from the global modeling.
- $F_T^{conc}$  The factor for degradation of concrete material properties with increasing temperature. This is considered an important material modeling variable in determining the pressure capacity of the PCCV from the global modeling.
- $\sigma_y^{rebar}$  Yield stress for rebar. This is deemed an important material variable in determining the pressure capacity of the PCCV from the global modeling. Generally, variations in yield stress also correspond to changes in ultimate tensile strength.
- $\sigma_y^{steel}$  Yield stress for the steel components, again with some corresponding variation in tensile strength. This is deemed an important material variable in determining the pressure capacity of the steel components.
- $\sigma_y^{weld}$  Yield stress (and tensile strength) of welded joints. This could affect the failure pressure in the EH modeling. Variations in this parameter will be accounted for in determining the 95% confidence band for the rupture strain in assessing the failure of components with welded joints.
- $F_T^{st}$  The factor for degradation of steel material properties with increasing temperature, but is deemed a small effect relative to the 95% confidence value that will be applied to the yield stress, that is, the effect of temperature on yield stress is not that significant (~82.5% of median at 500 °F). Variations for this parameter will be considered in determining the 95% confidence value for yield stress.
- $\sigma_{pre}^{tendon}$  Level of prestressing in PCCV concrete. This is deemed an important parameter in determining the pressure capacity of the PCCV from the global modeling. Variations will include the effects of tendon relaxation, concrete creep, and loss at anchorages. The 95% confidence value will be based on the 50 year value of pre-stressing used in the design of the PCCV.
- $\sigma_y^{tendon}$  Yield stress (and tensile strength) of the tendons. This is considered an important material variable in determining the pressure capacity of the PCCV from the global modeling.
- $\sigma_y^{bolt}$  This is the yield strength for the bolts in the bolted connections in the EH. This is a material parameter used for establishing the failure pressure for leakage at the bolted connection.
- $\sigma_{pre}^{bolt}$  This is the pre-stress in the bolts for the bolted connections in the EH. This parameter can affect the pressure capacity due to flange distortion.

- $\epsilon_r^{reb}$  The level of plastic strain used to define rupture of rebar. This is an important failure criteria parameter, and will be considered as a parameter variation to determine a corresponding  $\beta_f$ . The rebar rupture strain is determined by factoring uniaxial test data to account for strain concentrations at concrete cracks, which is below the refinement level of the analytical model.
- $\gamma_s^{conc}$  The level of shear strain across a section of pre-stressed concrete causing shear failure of the section. This is an important failure criteria parameter in establishing shear capacity, and will be considered as a parameter variation to determine a corresponding  $\beta_f$ .
- $\epsilon_r^{st}$  The level of effective plastic strain used to define failure of structural steel components, and is factored from uniaxial test data to account for mesh refinement and biaxial loading. This is deemed an important failure criteria parameter for which a  $\beta_f$  will be determined.
- $\epsilon_r^{liner}$  The level of effective plastic strain used to define tearing in steel liner material, determined by factoring uniaxial test data to account for mesh refinement and biaxial loading. This is a failure criteria parameter, and will be lumped with SCF below in determining a standard deviation for uncertainty. Reduced ductility due to welding of the liner will also be taken into account in developing the 95% confidence value.
- SCF This is a strain concentration factor to evaluate liner tearing at liner discontinuities, such as anchorages, that are not included in the model. This will be derived based on previous work. This is a failure criteria parameter to be lumped with the tearing strain level above to determine a standard deviation for liner tearing.
- $\epsilon_r^{tendon}$  The level of plastic strain used to define rupture of tendons. This is an important failure criteria parameter, and will be considered as a parameter variation to determine a corresponding  $\beta_f$ .

#### 4.5 Uncertainty in Modeling and Processes

There is also epistemic uncertainty associated with unknown processes and the modeling and analytical limitations used in the analyses for determining the failure pressures for any given set of material properties, geometry, or other problem parameters. This uncertainty concerns the mesh fidelity, the type of element formulations used, the robustness of the constitutive models, the equilibrium iteration algorithms and convergence tolerances, geometric imperfections, construction exactness, rebar placement locations, and the like. This modeling uncertainty must be quantified as part of the fragility calculation. Generally, this uncertainty is based on experience and judgment of the analyst because the analytical effort needed to consider variations in these modeling parameters is prohibitive. However, for this effort, some engineering judgment is invoked, but the modeling uncertainty is primarily based on previous work where similar modeling has been used to predict structural performance that can be compared to test data. This procedure has been employed in similar previous work, Reference 2.3.10. Several pretest analytical predictions have been performed for structural specimen tests using the same software and modeling philosophy, namely mesh fidelity, element formulations, convergence algorithms, and so forth. Many of these predictions and

tests concern the pressure capacity of concrete containments, for example, the 1:4 scale PCCV model tested to over-pressurization failure at Sandia National Laboratories, References 2.3.17 and 2.3.18. Thus, the modeling uncertainty can be determined by comparing the predicted analysis results with the test results. A list is constructed of about 20 such comparisons, and the ratio of the test result to the predicted result is determined for each. These data points are sorted into ascending order and plotted for cumulative probability versus the ratio of test result to analysis prediction. The cumulative probability is then calculated for each point as  $n/(N+1)$  where  $n$  is  $n^{\text{th}}$  point in the series and  $N$  is the total number of data points. For example, the probability that the test-to-analysis ratio will be less than that defined by the  $n^{\text{th}}$  point is  $n/(N+1)$ . A cumulative probability function, based on a lognormal probability distribution function, can then be fitted to the data through a least squares analysis for the 2 parameters defining the lognormal probability density function. This is illustrated in Figure 4-1, and the so determined lognormal variance is the uncertainty in the modeling used for these analyses. Note that the mean for the fitted lognormal probability density function is a measure of the shift from a ratio of 1.0 for the test results to the analysis predictions. The calculated value shows that the analysis predictions are in general slightly smaller than the test results, i.e. that the median value of the ratio is 1.004. This means that a calculated median failure pressure is likely to be slightly below the actual value for the modeling procedures employed. Therefore, the modeling techniques employed are comfortably accurate and, if anything, are slightly conservative. Because the test data and analyses are all at ambient temperatures, the calculated  $\beta$  for modeling uncertainty is increased by 10% for the analyses associated with the LTA thermal conditions and by 20% for the analyses of the hydrogen burning thermal conditions. Also, because the local modeling for the EH takes boundary conditions from the global model and performs additional analyses, the respective modeling uncertainties are increased by an additional variance of  $\beta = .06$  that is typical for analyses of steel components. The values of lognormal standard deviations for modeling uncertainties are summarized in Table 4-1.

**Table 4-1 Summary of Variance for Modeling Uncertainty**

Analysis Type	Lognormal Standard Deviations		
	Normal Operating	Long Term Accident	Hydrogen Burning
Global Modeling	.1232	.1355	.1478
Local Modeling	.1370	.1482	.1596

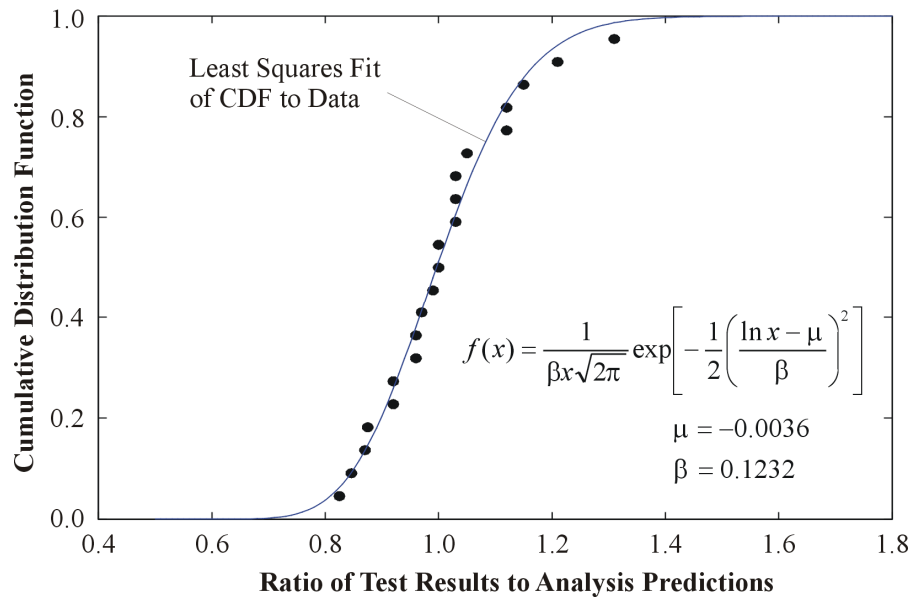


**Figure 4-1 Calculation of Variance due to Modeling Uncertainty**

#### 4.6 Thermal Conditions

As mentioned above, the fragility to over-pressurization is a function of temperature because internal pressure is associated with an accident condition involving elevated temperatures, and the capacity also depends on thermal stresses and material property degradation at elevated temperatures. The variation and uncertainty in the thermal conditions is considered here by defining a range of thermal conditions used in determining the fragility. The thermal conditions are intended as bounding cases for the type of accident under consideration. The associated probability of failure with pressure level can then be evaluated in the risk assessment by considering the probability that a given internal pressure can exist for a given thermal condition and the probability that the combination will occur during the life of the structure.

The pressure capacity is thus calculated at 3 different thermal conditions, 1) normal operating steady state conditions, 2) steady state long term accident conditions, and 3) severe accident transient conditions (hydrogen burning) where high temperatures develop for a short duration. These thermal conditions are assumed to develop in extreme winter ambient conditions where larger thermal gradients through the structure would develop, as a conservative measure to help minimize the number of analyses needed. The interior of the PCCV has uniform atmospheric temperature that acts over all interior surfaces. The exterior of the PCCV has some surface area exposed to ambient (open air) temperatures and some surface area exposed to room temperatures where the reactor building covers parts of the PCCV. These areas for the exterior surface of the PCCV are defined in Figure 4-2. The actual boundaries in the model are approximate based on element sizing and spacing. The interior surfaces of the penetration collars through the PCCV wall will also be exposed to room temperatures because these are covered by the reactor building, and the closure lids for the penetrations are on the inside of the containment. The inside surface of the closure lid and flanges are exposed to the PCCV atmosphere temperature. Table 4-2 provides a summary of the temperature conditions for the various surfaces for the 3 thermal conditions based on Reference 2.1.1. The film coefficients to be used for heat convection on the various surfaces, as summarized in Table 4-5, are based on relations taken from Reference 2.3.21.

The PCCV interior atmosphere temperature representing the long term design basis accident is based on the data provided loss of coolant in loss of operation power(LOOP) or loss of component cooling water system (CCWS) / essential service water system (ESWS) and reactor coolant pump(RCP) seal LOCA. A simplified fit to this data is provided in Table 4-3 and plotted in Figure 4-3. For this thermal condition, the temperature distribution is based on a steady state solution with the PCCV atmosphere at 438 °F, which develops around 100 hours. The conditions for the severe accident are based on the conditions described in Reference 2.1.3 for the case of hydrogen burn. Table 4-4 provides the tabular data for this hydrogen burning condition with the corresponding plot in Figures 4-4. The temperature distribution for this case is based on a transient thermal analysis with a snapshot of the temperature distribution taken when the liner reaches 1000 °F.

**Table 4-2 Summary of Temperature Conditions**

<b>Condition</b>	<b>PCCV Interior Temperature (°F)</b>	<b>PCCV Open Air Temperature (°F)</b>	<b>PCCV Room Temperature (°F)</b>	<b>Ground<sup>a</sup> Temperature (°F)</b>
Normal Operating Steady State	105	-40	50	35
Long Term Accident Steady State	438	-40	50	35
Hydrogen Burning Transient	1000	-40	50	35

Note:

- a The ground temperature is the temperature assumed at the bottom of the basemat.

**Table 4-3 Temperature and Pressure in PCCV for Long Term Accident Thermal Condition**

--

**Table 4-4 Temperature and Pressure in PCCV for Hydrogen Burning Thermal Condition**

--

**Table 4-5 Film Coefficients for Thermal Conditions**

<b>Surface</b>	<b>Film Coefficient (BTU/hr-ft<sup>2</sup>-°F)</b>	<b>Comments</b>
Interior Steel Surfaces	infinite	Use large coefficient so that temperature of steel surface tracks PCCV atmosphere temperature
Exterior Concrete Surfaces	2.5	Concrete exposed to ambient elements and wind
Interior Concrete Surfaces	1.0	Concrete exposed to controlled room circulation inside Reactor Building

**Security-Related Information – Withheld Under 10 CFR 2.390**

**Figure 4-2 Thermal Conditions on Exterior Surfaces of PCCV**



**Figure 4-3 Temperature and Pressure for Long Term Accident Condition**



**Figure 4-4 Temperature and Pressure for Hydrogen Burning Condition**

#### 4.7 Material Properties

The analyses for establishing the pressure fragility of the primary containment system are best estimate calculations and are based on median or expected material properties. Analyses using the 95% confidence value of important material properties are used to assess the effect of uncertainty in the actual material properties. As described above, the variation in the thermal conditions leading to over-pressurization is handled by defining the fragility at various thermal conditions that are chosen a-prior to cover the temperature regimes of interest. Thus, variations in the thermal material properties are not considered in the uncertainty evaluation, for example, variations in the thermal conductivity or film coefficients will have little effect on the steady state temperature distribution through the PCCV wall for a given thermal condition where interior and exterior temperatures are defined. The thermal properties are based on commonly accepted values and summarized in Table 4-6. The heat transfer or film coefficients used for heat convection from surfaces exposed to temperatures are summarized in Table 4-5 in Section 4.6.

By contrast, the mechanical material properties and their variation with temperature can have a significant effect on determining the pressure capacity. The strength, stiffness, and shear capacity of concrete along with the yield stress and ultimate strength of reinforcement and tendons will directly affect the pressure resisting capacity of the PCCV. The yield stress, strain hardening characteristics, and ductility of the steel material will directly affect the performance of the liner and penetration components. Thus, median and 95% confidence values must be developed for the elastic and plastic material properties, all as a function of temperature. While a set of 3 discrete thermal conditions are identified for the range of temperatures of interest, the temperatures within the structural components will have a continually varying distribution. Thus, the material properties must cover the entire range of temperatures from ambient to 1000 °F. A summary of the snapshot values for 3 discrete temperatures are provided in Table 4-7 for the elastic properties and Table 4-8 for the plastic properties for the steel materials. This data has been collected and synthesized from a variety of sources, as noted in the tables. Typically, data for the median and distribution of a property at room temperature is available, and some data for the variation of the median value with temperature is found. The 95% confidence values at elevated temperatures are then determined using the distribution at room temperature but with increasing uncertainty for increasing temperature. For the steel materials, continuous curves for the effective stress versus effective strain plasticity relations are developed for both the median and 95% confidence values and for temperatures of 150, 250, 500, 800, and 1000 °F. In the analysis, linear interpolation between these values is used for intermediate temperatures, so these temperatures are chosen to provide a relatively good piecewise linear fit to the degradation shapes of the properties with temperature. Figure 4-5 illustrates the engineering stress strain relations with temperature for A615 Grade 60 reinforcing bars for median and 95% confidence values. Figure 4-6 illustrates the engineering stress strain relations with temperature for A516 Grade 60 material used for the liner plate for both median and 95% confidence values.

For concrete, the elastic modulus, shear modulus, and tensile strength are functions of the compressive strength. The 95% confidence value for the compressive strength is taken as the design strength, namely 7 ksi concrete for the PCCV and 4 ksi concrete for the basemat. Because this should be the minimum value delivered in the field, the median value for compressive strength is based on the American Concrete Institute (ACI) requirements (Ref 2.2.3) linking the delivered strength to cylinder specimen testing accounting for variability. One requirement is that the average 28-day test cylinder strength,  $f'_c$ , is to exceed the

specified design strength by the amount  $1.34*s$ , where  $s$  is the standard deviation of the strength for the set of test specimens. Another requirement is that the cylinder test strength must equal or exceed a value of  $0.9*f'_c + 2.33*s$ . The delivered strength is similar for these 2 requirements for coefficient of variations around 10% in the concrete batches. For the PCCV concrete, the 7 ksi design strength is based on the 90 day value, and the median value is determined using the same ACI relations. A variation of 10% in compressive strengths for any batch of concrete is assumed as a basis for deriving the standard deviation and calculating the median value of compressive strength at ambient temperature. From this median value of compressive strength, the elastic modulus is calculated from the ACI relationship,  $E = 57,000\sqrt{f'_c}$ . The variations of compressive strength and tensile strength with temperature are based on the data in Reference 2.3.9. No aging effects, which will strengthen the concrete over time, are included in these analyses. A summary of the concrete properties at these discrete temperatures is provided in Table 4-9. The behavior of the compressive strength with temperature is illustrated in Figure 4-10.

**Table 4-6 Summary of Thermal Material Properties**

Material	Weight Density (lb/ft <sup>3</sup> )	Specific Heat (BTU/lb-°F)	Conductivity (BTU/hr-ft-°F)	Coefficient of Expansion (/°F)
Concrete	150	0.21	1.0	5.5E-6
Carbon Steel Liner	490	0.11	31	6.5E-6
Structural Steel	490	0.11	31	6.5E-6
Reinforcement <sup>1</sup>	--	--	--	6.5E-6
Tendons <sup>1</sup>	--	--	--	6.5E-6

Note:

- 1 Reinforcement and Tendons take on the temperatures of the surrounding concrete

**Table 4-7 Summary of Elastic Mechanical Properties for Steels**

	Normal Operating Conditions (150 °F)		Long Term Accident Conditions (500 °F)		Hydrogen Burning Conditions (1000 °F)		Ref
	Median	95 %	Median	95 %	Median	95 %	
SA 516 Carbon Steel							
Modulus (xE6 psi)	29.5	29.0	26.8	26.4	17.7	17.4	2.2.2
Poisson's Ratio	0.289	0.289	0.295	0.295	0.304	0.304	2.3.6
Prestressing Tendons							
Modulus (xE6 psi)	28.6	28.4	26.9	26.4	25.2	24.4	2.3.8
Poisson's Ratio	--	--	--	--	--	--	
SA 193 Gr B7 Bolting							
Modulus (xE6 psi)	29.7	29.2	27.6	26.7	23.5	21.5	2.2.2
Poisson's Ratio	0.3	0.3	0.3	0.3	0.3	0.3	

**Table 4-8 Summary of Plastic Mechanical Properties for Steels**

	Normal Operating Conditions (150 °F)		Long Term Accident Conditions (500 °F)		Hydrogen Burning Conditions (1000 °F)		Ref
	Median	95 %	Median	95 %	Median	95 %	
SA516 Grade 70							
Yield Stress (ksi)	48.62	42.8	43.8	38.5	37.9	30.6	2.3.3
Tensile Strength (ksi)	77.04	71.3	70.9	66.7	63.6	50.8	2.3.4
Elongation (%)	20.3	17.0	20.5	16.4	33.7	24.0	2.3.5
SA516 Grade 60							
Yield Stress (ksi)	40.94	36.06	36.85	32.39	31.94	25.79	Based on Gr 70
Tensile Strength (ksi)	66.03	61.14	60.75	57.20	54.48	43.52	
Elongation (%)	25.1	21.0	25.4	20.3	41.7	29.7	
A615 Grade 60 Rebar							
Yield Stress (ksi)	68.6	63.5	54.9	45.7	39.1	29.0	2.3.6 2.3.7
Tensile Strength (ksi)	105.0	97.0	104.0	86.4	64.1	47.3	
Elongation (%)	12.5	8.6	13.0	9.0	14.0	10.0	
A416 Grade 1860 Tendons							
Yield Stress (ksi) @ 1%	259.5	243	249.1	231.0	233.5	212.1	2.3.8
Tensile Strength (ksi)	278.2	270	269.9	260.8	256.0	244.5	
Elongation (%)	3.66	3.50	3.80	3.60	4.00	3.74	
SA 193 Gr B7 Bolting							
Yield Stress (ksi) @ .2%	111.6	105.0	95.7	88.5	58.8	50.9	2.2.2
Tensile Strength (ksi)	131.6	125.0	131.3	125.0	86.3	78.4	
Elongation (%)	18.5	16.0	19.8	17.3	21.1	18.7	

**Table 4-9 Summary of Concrete Material Properties**

Material/Property	Normal Operating Conditions (150 °F)		Long Term Accident Conditions (500 °F)		Hydrogen Burning Conditions (1000 °F)		Ref
	Median	95 %	Median	95 %	Median	95 %	
PCCV Concrete (7 ksi)							
Comp Strength (psi)	8891	7000	6757	5233	4817	3298	2.3.9
Strain at Peak Comp (%)	0.19	0.20	0.27	0.36	0.46	0.68	
Modulus (xE6 psi)	5.375	4.769	2.922	1.912	1.243	0.617	
Tensile Strength (psi)	707.2	627.5	537.4	416.3	383.1	262.4	
Fracture Strain (xE-6)	131.6	99.1	183.9	138.5	308.2	232.2	
Poisson's Ratio	0.22	0.18	0.22	0.18	0.22	0.18	
Basemat Concrete (4 ksi)							
Comp Strength (psi)	5081	4000	3818	2948	2722	1858	2.3.9
Strain at Peak Comp (%)	0.19	0.20	0.27	0.36	0.46	0.68	
Modulus (xE6 psi)	4.063	3.605	2.167	1.407	0.922	0.454	
Tensile Strength (psi)	534.6	474.3	401.7	310.1	286.4	195.5	
Fracture Strain (xE-6)	131.6	99.1	185.3	139.6	310.6	234.0	
Poisson's Ratio	0.22	0.18	0.22	0.18	0.22	0.18	

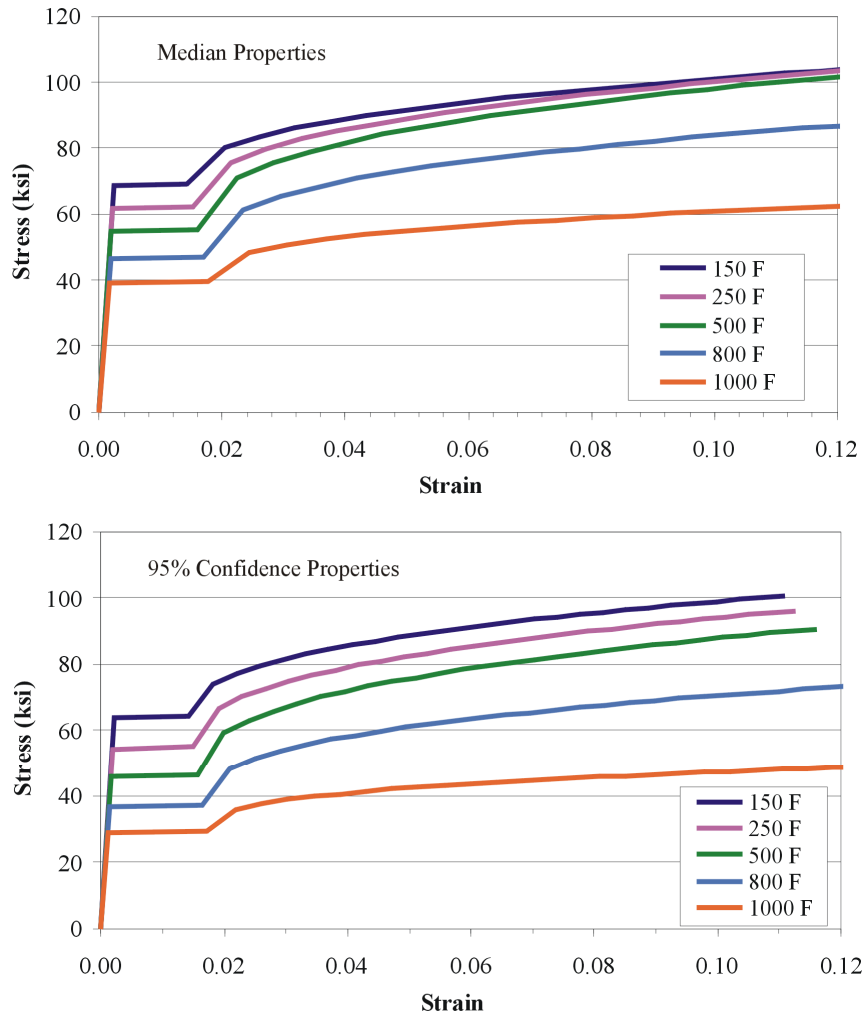
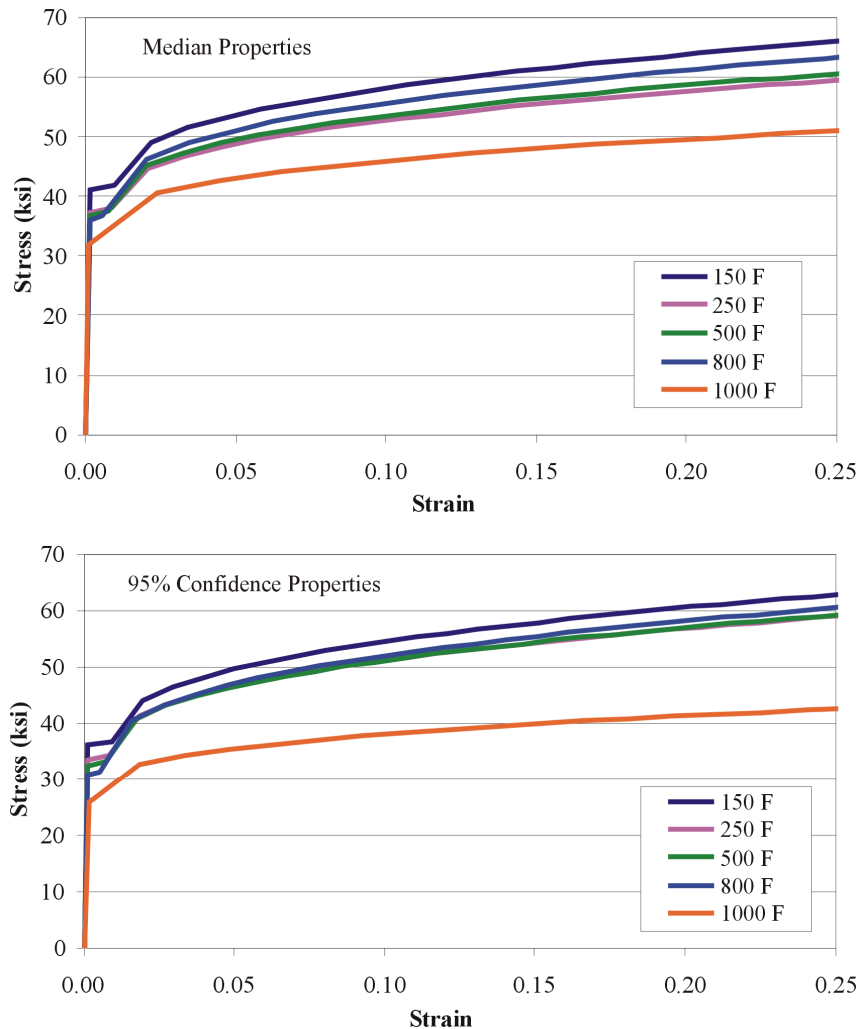


Figure 4-5 Illustration of Stress-Strain Relations for A615 Grade 60 Rebar



**Figure 4-6 Illustration of Stress-Strain Relations for A516 Grade 60 Liner Plate**

#### 4.8 Concrete Performance

The modeling of the concrete is a key ingredient for the ultimate strength analyses and is provided through the ANACAP-U constitutive model. The behavior of concrete is highly nonlinear with a small tensile strength, shear stiffness and strength that depend on crack widths, and compressive plasticity. The main components of the concrete model for these analyses are tensile cracking, post-cracking shear performance, and compressive yielding when the compressive strength is reached. A summary description of the modeling for concrete behavior used in this software is described below.

Tensile cracking in the concrete is governed by the magnitude of the load in the directions of principal strain. Cracks are assumed to form perpendicular to the directions of largest tensile strains. Multiple cracks are allowed to form at each material point, but they are constrained to be mutually orthogonal. If cracking occurs, the normal stress across the crack is reduced to zero and the distribution of stresses around the crack is recalculated through equilibrium iteration. This allows stress redistribution and load transfer to reinforcement or other load

paths in the structure. Once a crack forms, the direction of the crack remains fixed and can never heal. However, a crack can close, resist compression and shear, and re-open under load reversals. The cracking criterion is based on an interaction of both stress and strain as illustrated in Figure 4-7. The model predicts cracking when the generalized (principal) stress and strain state exceeds the limit state shown. Thus, biaxial and triaxial stress states are treated consistently with uniaxial conditions, but the associated cracking will now occur at a slightly higher stress and slightly lower strain. Split cracking, for example near a free edge under high compressive stress, occurs at near zero stress and a tensile strain approximately twice that of uniaxial tensile cracking.

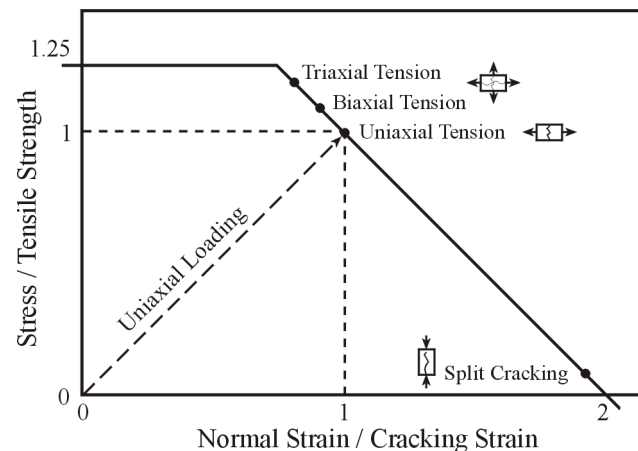


**Figure 4-7 Crack Initiation Criteria Curve**

The surfaces of cracks that develop due to tensile stress in concrete are usually rough and irregular. When a shear force is applied along a crack surface, tangential sliding occurs and this causes displacements normal to the crack surface to develop as the crack surfaces ride up on each other. When this normal displacement is restrained by reinforcement crossing the crack, tensile stresses will develop in the steel bars, which will then induce compressive stresses across the crack in the concrete. The resistance to sliding is provided by the frictional force generated by the compressive stress across the crack. The crack width is the primary variable affecting this mechanism of shear transfer. Smaller crack widths correspond to greater shear stiffness and strength. Aggregate size, reinforcement design, and concrete strength are other important factors. In order to account for the effect of cracking on shear stiffness, a reduced shear modulus is retained in the stress-strain matrix when a crack forms. The shear moduli in the plane of the crack are immediately reduced by 60% when a crack forms. The shear stiffness is further reduced using a hyperbolic variation with the opening strain normal to the crack, as illustrated in Figure 4-8.

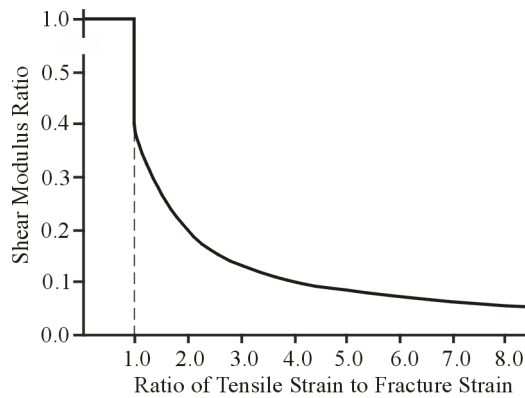


**Figure 4-8 Shear Modulus Reduction for Open Cracks**

Perhaps the most important feature of concrete modeling is the ability to capture the shear capacity in cracked concrete. The ANACAP model is equipped with a shear-shedding feature to model the shear stress capacity across an open crack. The shear retention model reduces the incremental shear modulus across an open crack as discussed above. The shear stress capacity for an open crack is a function of the crack opening strain, as illustrated in Figure 4-9. The shear-shedding feature reduces the shear stresses previously supported across an open crack if the crack continues to open. Again, equilibrium iterations are needed to redistribute the loads. Recall that cracks form in the principal strain directions so that, in general, there is no shear across a crack when it first opens. However, continued loading resulting in shear deformations will be carried in shear across the crack if possible.

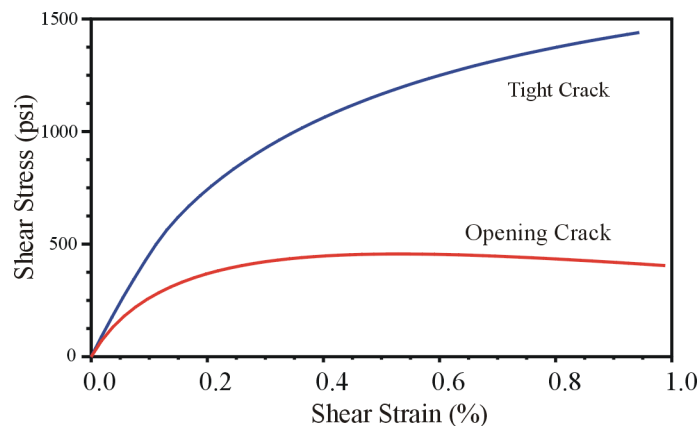


**Figure 4-9 Example of Shear Stress Capacity Across Open Cracks**

In the compression regime, the continuous stress-strain curve is defined from uniaxial test data, which is then generalized to multi-axial stress/strain states using the uniaxial equivalence of the multi-axial state, namely, the effective stress and the effective strain. The uniaxial behavior is generalized to multi-axial behavior, within the analytical framework of isotropic hardening plasticity formulation, using a Drucker-Prager surface to represent the loading surface under multi-axial compression. In this formulation, the loading surface is a function of the hydrostatic pressure, the second invariant of the deviatoric stress tensor, and the yield strength. This type of formulation incorporates the effects of low to moderate confinement stress levels, which typifies the behavior of civil structures. These relations allow for linear behavior for compressive stresses below about 50% of the compressive strength, and then strain hardening behavior until the compressive strength is reached. In addition, the

compressive strength, initial modulus, and the compressive strain level that supports the peak compressive strength are functions of temperature. In compression, concrete softens with increasing temperature, exhibiting lower compressive strength while extending the range of competent compressive strain. The stress-strain behavior under uniaxial compression is illustrated in Figure 4-10, which shows both the median and 95% confidence properties for 7 ksi concrete.

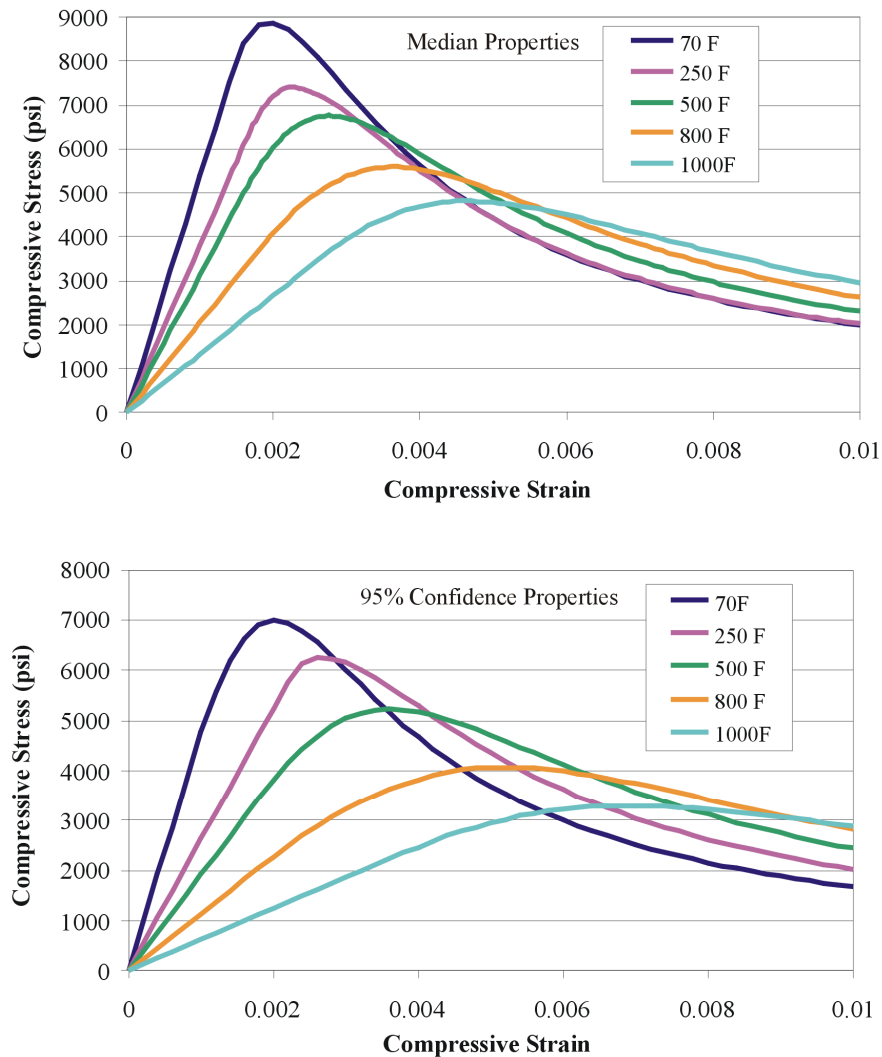


**Figure 4-10 Uniaxial Compressive Strength as Function of Temperature**

#### 4.9 Failure Criteria

In evaluating the pressure capacity for the containment system, failure criteria must be defined to establish limit states on the structural response where the internal pressure is no longer contained by the structure. There is uncertainty in defining these failure criteria, so median and 95% confidence values are defined to evaluate the effect of the uncertainty on the analysis results. For the reinforced concrete components, failure either occurs when tensile loads cause rebars to yield and then rupture, or when the shear forces across a section exceed the shear capacity. Under bending loads, concrete crushing may develop on the compressive side, but failure of the section can still be attributed to rebar rupture on the tension side of the section. Section shear failure develops when sufficient cracking extends across a section such that the shear capacity of the concrete due to aggregate interlock is reduced below that needed to support the shear demands, as discussed in Section 4.4. Section shear failure can also occur when compressive struts develop due to arch action within a member and initiate concrete failure in compression, which then also rapidly degrades the shear capacity of the section. Thus, the failure criteria used to establish structural failure of the PCCV in the global modeling are 1) the strain level in rebars causing rupture of the bar, 2) the level of shear strain across a structural section that indicates the shear capacity is exceeded, and 3) the strain level causing rupture of prestressing tendons.

As the limit state for section shear failure, a criterion for concrete shear strain across a section is defined. This failure criterion has been established for the modeling methodology employed based on previous work and benchmarking with experimental tests on structural specimens, References 2.3.12, 2.3.13, and 2.3.14. In particular, the section shear capacity criteria is based on research performed by ANATECH in support of Sandia National Labs for a NRC sponsored study on the seismic capacity of PCCVs, documented in Reference 2.3.13. This study involved a series of shake table tests on a scaled PCCV model performed in Japan, in which increasing levels of seismic loading are applied until eventual failure of the test model occurs. Analytical simulations of these series of tests were performed by ANATECH using the same concrete material model and modeling methods as employed on the pressure fragility calculations. The structural configuration considered is a prestressed concrete containment, very similar to that in the pressure fragility assessment. In the analytical effort simulating the PCCV model tests, a subset of the series of tests were performed to capture the accumulation of damage in the concrete, and the model response and thus level of damage calculated was considered to be in relatively good agreement with the test data. The test model eventually failed in shear, and examination of the analytical model at the failure conditions indicated that about 0.55% shear strain had developed across the wall of the PCCV. This section shear failure criteria has since been applied to deep beam tests that fail in shear and shown to be consistent with these failure conditions. Since shear failure is mainly a function of crack opening such that aggregate interlock and interface friction no longer provide sufficient resistance to shear deformations, this section failure criteria is also considered appropriate for these pressure fragility analyses. That is, the failure criteria is not dependent on the method of loading, just the level of strain that develops across the structural section from any loading. Once a shear band forms and the concrete shear strains reach a median level of .55% across the complete section, a brittle type shear failure of the section is assumed to occur. This criterion is needed, independent of rebar performance, because this structural failure mode can develop before rebar rupture or even rebar yield is reached in the analysis. The median and 95% confidence values for this concrete section shear strain are shown in Table 4-10. Note that this failure criterion is considered independent of temperature, but because the concrete properties degrade with temperature, the section shear capacity is

reduced with temperature.

The rupture strain for Grade 60 reinforcing bars is based on the elongation limits from test data. The test specimen elongation strain is then factored to account for strain concentration factors that are not captured by the finite element modeling, which is based on smeared cracking. In reinforced concrete structures, cracking generally develops in a series of discrete cracks, and the strain in the rebar is intensified at the intersection of these discrete cracks. From previous experience with similar modeling (References 2.3.10, 2.3.11 and 2.3.12), this strain concentration factor has a median value of 2.0, and the calculated strain at which rebar rupture can occur is generally taken to be 5% at room temperature. The median and 95% confidence values as a function of temperature for rebar fracture strain are summarized in Table 4-10.

For greased prestressing tendons, there is no strain concentration factor introduced due to cracking because the tendon acts independent of the concrete strain along the direction of the tendon. Thus, the rupture strain is based on nominal reductions in the elongation data for the tendons strands. The median and 95% confidence values as a function of temperature for tendon rupture strain are summarized in Table 4-10.

Failure criteria are also defined to consider leakage due to tearing of the liner. Tests of over-pressurization of PCCV scale models show that liner tearing will develop at discontinuities where strain concentration factors exist, in particular at the connections of liners with thicker plates at penetrations or geometric discontinuities. From previous work, for example Reference 2.3.15, this failure criterion for a tearing strain is based on the ductility of the material and the magnitude of strain concentration factors not captured by the fidelity of the modeling. First, the ductility of the liner material is defined based on elongation data performed on uniaxial test specimens. The ductility depends on the state of stress, which is generally biaxial or triaxial loading. For the liner at penetrations, the loading due to internal pressure is biaxial with the hoop tension twice that of the tension in the axial direction. This biaxial loading produces a ductility limit of 60% of the uniaxial elongation data. In addition, to account for reduced ductility in the heat affected zones of welds in the liner, a further reduction of 15% on the uniaxial test data is used. This ductility limit must then be further reduced for comparison to calculated liner strains to account for the strain concentration factors not captured in the analyses. This factor depends on the fidelity of the modeling. In the global model, the liner strains are taken at the local areas showing distress, that is, local strains rather than far field strains, and a median strain concentration factor of 6 is used on the ductility limit to establish liner tearing. For the thicker steel components of the penetration, the loading can be triaxial, and the elongation data is factored by 50% to determine the material ductility. The median and 95% confidence values for these failure criteria are summarized in Table 4-10. These values are consistent with those used in similar previous work described in Reference 2.3.10.

**Table 4-10 Summary of Material Limits and Failure Criteria**

Criteria	Normal Operating Conditions (150 °F)		Long Term Accident Conditions (500 °F)		Hydrogen Burning Conditions (1000 °F)	
	Median	95 %	Median	95 %	Median	95 %
Section Shear Strain (%)	.55	.44	.55	.44	.55	.44
Rebar Fracture Strain (%)	5.0	2.0	5.5	2.2	6.0	2.4
Tendon Failure Strain (%)	2.66	2.50	2.80	2.60	3.00	2.74
Liner Tearing Strain (%) (1/4" Thick, Grade 60)	2.13	1.72	2.16	1.45	3.54	2.42
Liner Tearing Strain (%) (>1/4" thick, Grade 70)	1.72	1.40	1.75	1.17	2.87	1.96
Bolt Rupture Strain (%)	9.2	6.8	9.9	7.2	10.6	7.6

## 5.0 PRESTRESSED CONCRETE CONTAINMENT

### 5.1 Model Description

A global 3-D model is used to assess the ultimate capacity of the PCCV due to over-pressurization under hydrogen burning conditions. This global modeling is needed to capture the overall structural performance and potential failure modes of the primary containment system and is sufficiently accurate to determine the ultimate pressure capacity of the PCCV components, governed by concrete, tendon, and rebar strength and their interaction. The ultimate capacity for the PCCV is based on strain limits for rebar and tendon rupture, concrete compressive stress, or concrete shear strain limits that indicate section shear failure. The concrete constitutive model includes tensile cracking, shear shedding, and compressive crushing as material limits. As loads are redistributed due to these material limits, the increasing loads will eventually lead to section failures. Also, an evaluation of liner tearing can be determined from the global model by considering calculated liner strains at distressed locations and factoring for strain concentration factors, based on previous similar analyses, to account for discontinuities at anchorages and connections. This evaluation for liner tearing also considers reduced ductility of the liner material due to biaxial loading conditions and for heat affected zones at weld seams.

The modeling consists of a free-standing, full height representation of the PCCV. The thermal model, illustrated in Figure 5-1, is used to determine the temperature distribution within the structure for each of the 3 thermal conditions, and the stress model, illustrated in Figure 5-2, is used to determine the pressure capacity based on the temperature distribution of interest and the combinations of the other parameter values. Steady state temperature solutions are used for the normal operating and LTA cases. A transient thermal solution is used for the hydrogen burning case with the initial conditions set to the steady state operating conditions. The appropriate temperature distribution is then transferred to the stress model, and the internal pressure is incrementally increased to find the failure pressure with that temperature distribution.

As illustrated in the figures, the concrete is modeled with solid elements and the steel liner is modeled with plate elements. The liner elements are attached to the common nodes on the surfaces of the concrete elements for compatibility with the concrete deformations. This assumes that the liner anchorage system keeps the liners in contact with the concrete for this global modeling of the PCCV performance. The prestressing tendons are modeled with truss elements using independent nodes from the concrete nodes. The tendon nodes are then constrained to the concrete nodes using constraint equations to capture the behavior of the greased tendons. For the hoop tendons, the tendons are constrained to the concrete in the radial and axial directions, but the tendon nodes are allowed to move relative to the concrete in the hoop direction. Similarly, for the axial tendons, the tendons are constrained to the concrete in the radial and hoop directions but are allowed to move relative to the concrete in the axial direction. For the areas with significant tendon curvature, for example the axial tendons in the dome and the tendons that wrap around the penetrations, the tendon nodes are fully constrained to the concrete. This tendon modeling is illustrated in Figure 5-3. The prestress loads are applied using an initial stress in the tendon elements. The tendon elements are divided into groups to allow variation in the initial stress distribution to simulate prestressing losses.

In the design basis of the PCCV, the effects of tendon relaxation, concrete creep, concrete shrinkage, and anchorage losses are considered in calculating a level of prestress after 60 years of operation based on American Society of Mechanical Engineers (ASME) code regulations. In the pressure fragility evaluation, this “end-of-life” prestressing level is considered the 95% confidence value of prestressing, that is, we are 95% confident that we will have at least this level of prestress over the life of the structure. For the nominal or best-estimate value of prestress, a level of prestress is used in the fragility analysis based on that calculated for the design basis at SIT conditions, which basically accounts for losses during anchorage seating and some initial tendon relaxation and concrete creep. The prestress levels used for nominal values are about 4% higher than those used for 95% confidence values. The effects of this variation in prestress are considered by performing an analysis with nominal values of all parameters, then another analysis using 95% confidence values of prestressing and nominal values of all other parameters and determining the change in the pressure capacity. The contribution to the variance or “standard deviation” in pressure capacity due to uncertainty in prestress can then be calculated from this difference in the pressure capacity as described in Section 4.3.

The reinforcement bars are modeled as embedded, truss-like steel elements at the appropriate locations within the concrete brick elements. The strains within the brick element at the locations of the rebar within that element are used to assess the rebar performance via the constitutive relations for the steel material. The associated stiffness and stress in the reinforcement are superimposed onto the concrete brick element. The reinforcement included in the modeling is illustrated in Figures 5-4 through 5-8, showing axial bars on the inner surface, axial bars on the outer surface, hoop bars on the inner surface, hoop bars on the outer surface, and other secondary reinforcement, respectively. As illustrated, some smearing of the reinforcement is performed to reduce modeling and computation times, for example, every other bar may be explicitly included but each with twice the area (2:1 modeling). In some areas, 4 bars are lumped together as a single truss-like sub-element with 4 times the individual rebar area (4:1).



**Figure 5-1 Full 3-D Finite Element Modeling for Thermal Analysis**



**Figure 5-2 Full 3-D Finite Element Modeling for Stress Analysis**



**Figure 5-3 Illustration of Modeling for Tendons**



**Figure 5-4 Modeling of Reinforcement, Inside Axial Bars**



**Figure 5-5 Modeling of Reinforcement, Outside Axial Bars**



**Figure 5-6 Modeling of Reinforcement, Inside Hoop Bars**



**Figure 5-7 Modeling of Reinforcement, Outside Hoop Bars**



**Figure 5-8 Modeling of Reinforcement, Other Bars**

## 5.2 Thermal Analyses

The thermal model is used to develop the temperature distributions for the stress model in performing the pressure capacity analyses. The temperature distributions determine the variation of material properties with temperature within the structure and thermal stresses based on the changes from reference temperature and restraint against thermal expansion or contraction. The 3 thermal conditions described in Section 4.6 are used as the basis for evaluating the variation of pressure capacity with temperature. The temperature distributions associated with these 3 thermal conditions are illustrated in Figure 5-9 for normal operating condition, Figure 5-10 for long term design basis accident condition, and Figure 5-11 for the hydrogen burning thermal condition. The temperature distribution for the normal operating condition is based on a steady state solution with the PCCV atmosphere at 105 °F. The temperature distribution for the LTA thermal condition is based on a steady state solution with the PCCV atmosphere at 438 °F. The temperature distribution for the hydrogen burning thermal condition is based on a transient solution when the PCCV atmosphere and liner reach 1000 °F for a postulated hydrogen burn scenario. All 3 thermal conditions are considered to occur during extreme winter ambient conditions when the air temperature is -40 °F. For the steady state based conditions, the gradient is linear through the wall. For the transient hydrogen burning case, the inside surface of the liner reaches 1000 °F while the surface of the concrete next to the liner has a peak temperature of 249 °F, as illustrated in Figure 5-11.

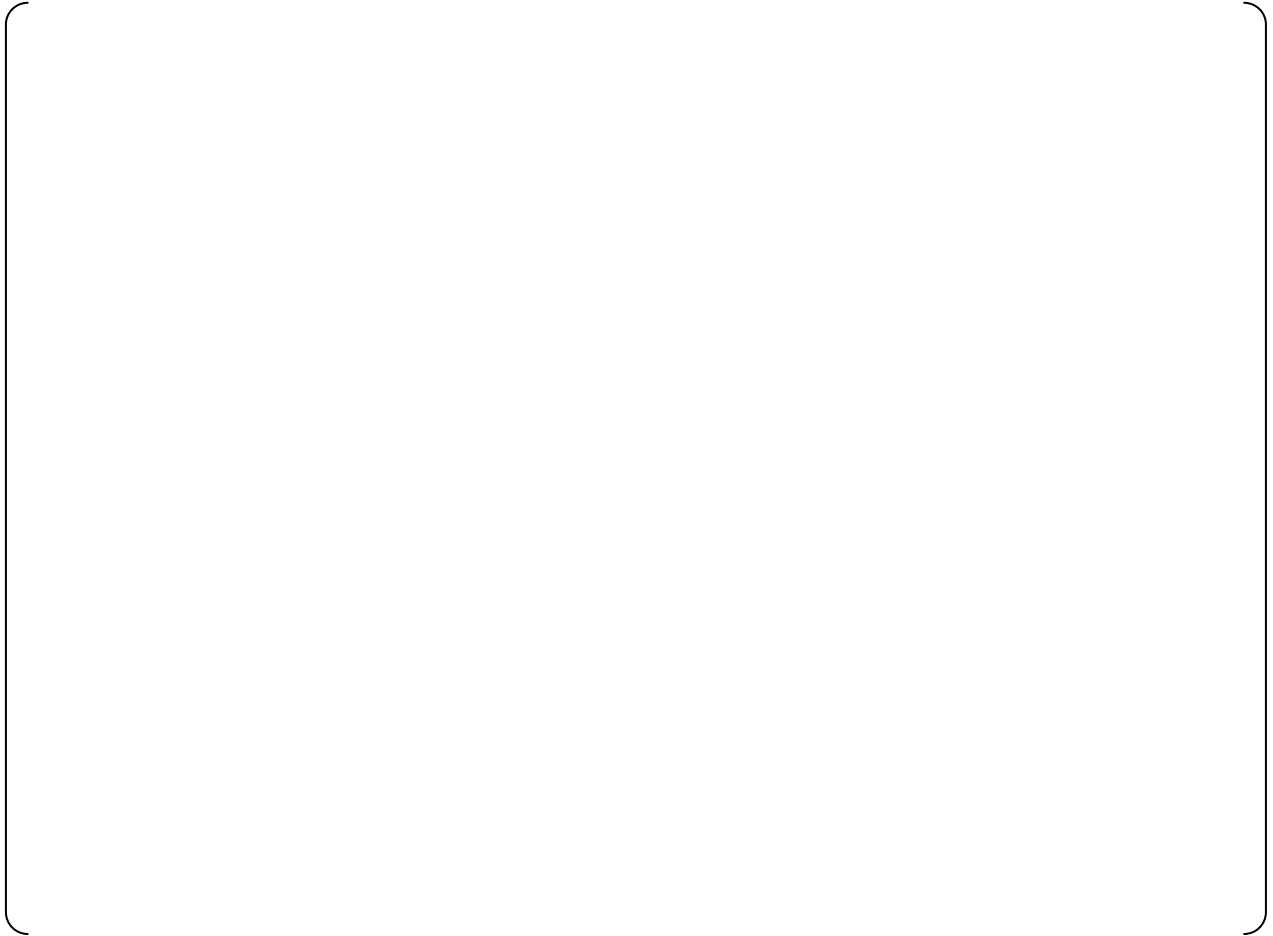


**Figure 5-9 Temperature Distribution for Normal Operating Condition**



**Figure 5-10 Temperature Distribution for Long Term Accident Condition**

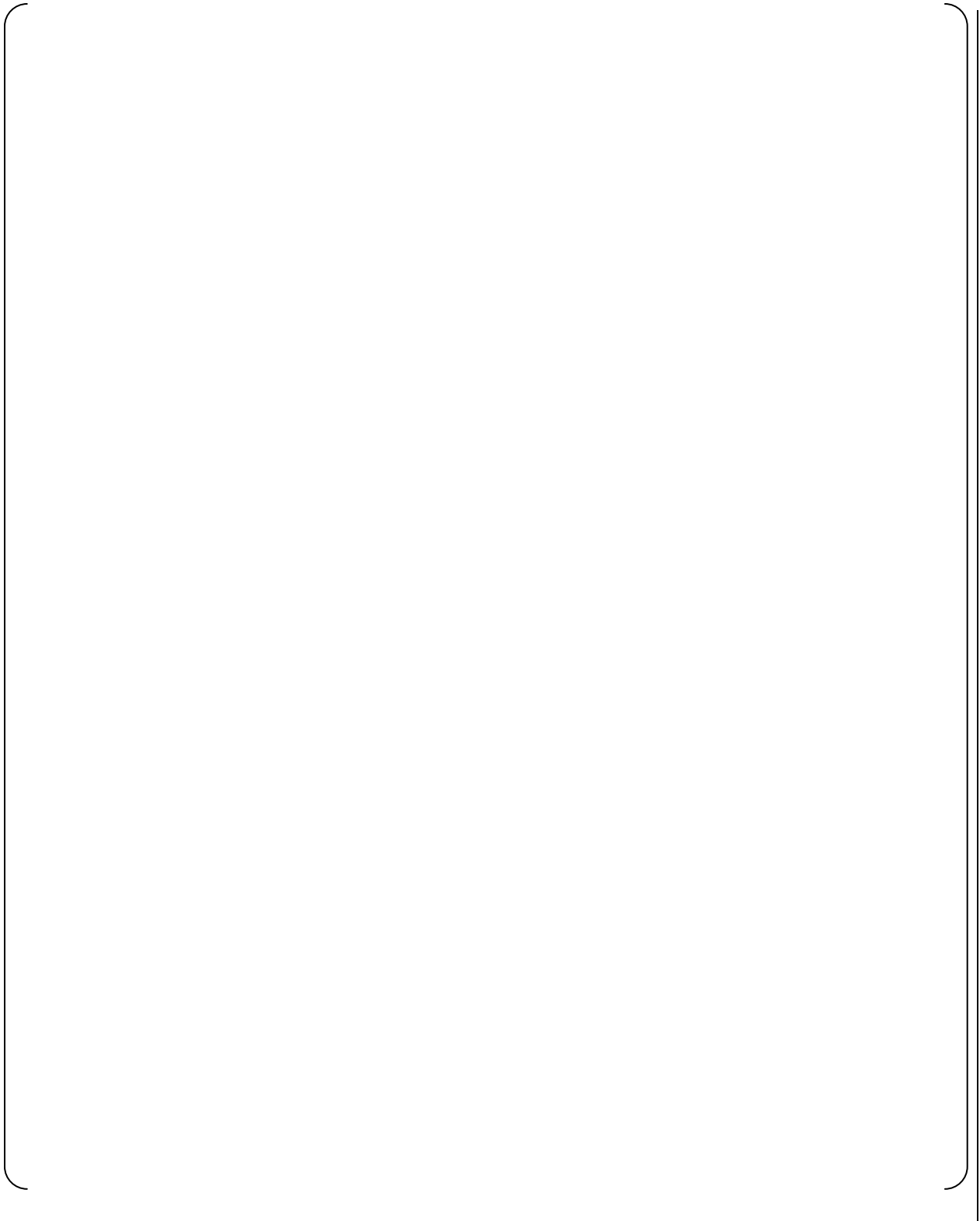


**Figure 5-11 Temperature Distribution for Hydrogen Burning Condition**

### 5.3 Median Capacity Analyses

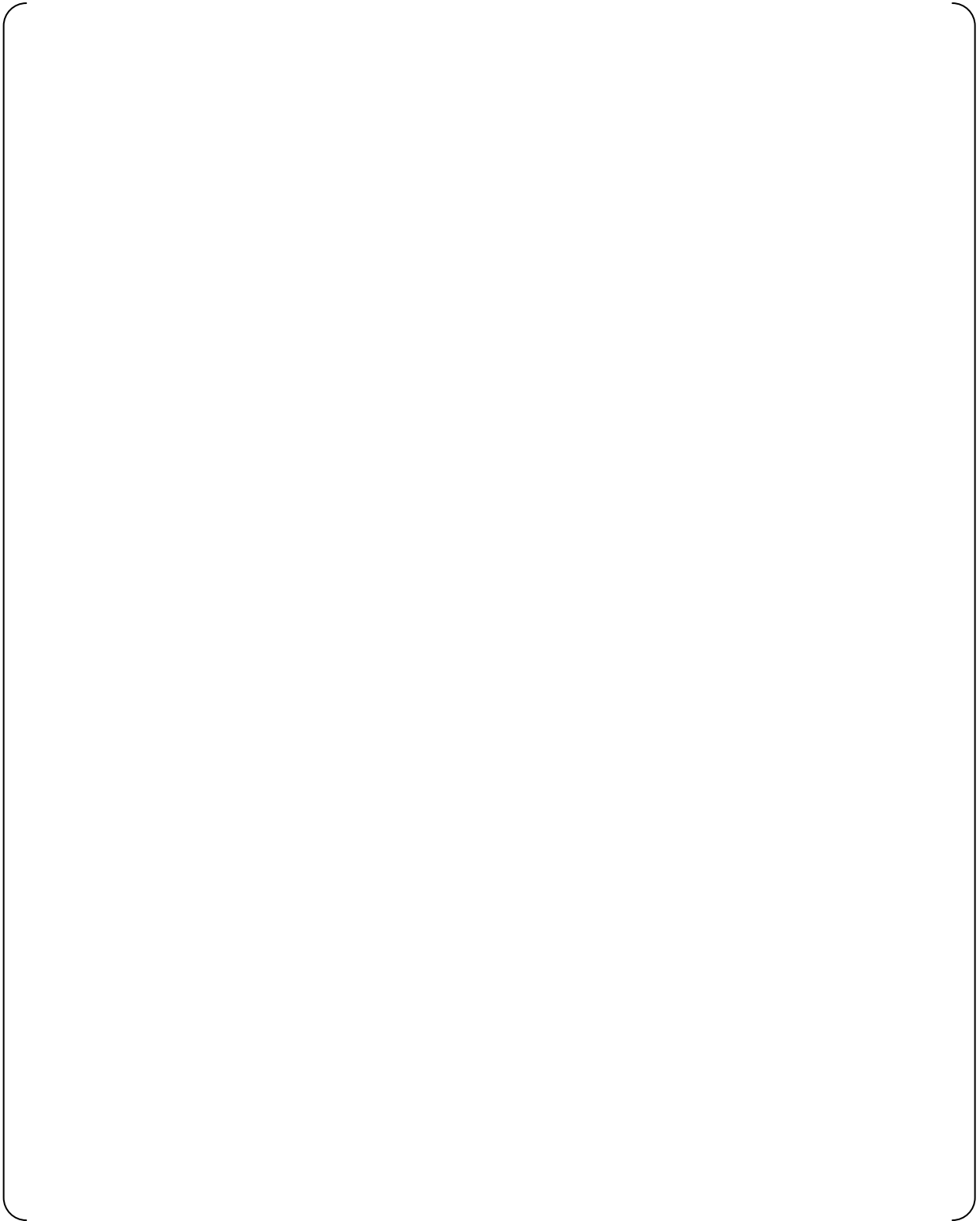
The median ultimate pressure capacity for the PCCV is determined using the global stress model along with median values of all material properties and failure criteria. The median pressure capacity is calculated for each of the 3 thermal conditions described in Section 4.6 and illustrated in the previous section. For each median pressure capacity analysis, the failure pressure for each mode of failure is determined based on the corresponding failure criteria, for example, monitoring liner plastic strains to determine the pressure where liner tearing initiates. The failure pressures for each failure mode are determined independently, that is, the structural effect or consequences due to initiation of any one failure mode does not influence the next failure mode. For example, when the rupture strain of a rebar has been reached, the pressure associated with rebar failure is determined, but the rebar continues to plastically deform until the next failure mode is reached. This complies with the basic assumptions needed for parameter independence in the probabilistic assessment.

Table 5-1 summarizes the median pressure capacities calculated for the various failure modes for the 3 thermal conditions. The following figures illustrate the performance of the PCCV during over-pressurization for the steady state LTA thermal condition. Figure 5-12 provides a contour plot for accumulated plastic strain in the liner illustrating the failure mode for liner tearing. The contour limit has been set to the failure strain at the corresponding temperature so that red color indicates areas near the failure limit. In this plot the peak plastic strain is shown to be above the failure limit so that liner tearing has initiated. Figure 5-13 provides a contour plot for maximum principal strains in the concrete. In this figure, the contour limit is set to 2% to highlight the areas of more extensive cracking to illustrate the cracking damage that develops leading to yield and rupture of rebar and tendons. Figure 5-14 provides a contour plot for plastic strain in the hoop tendons illustrating failure mode associated with tendon rupture. In this plot, the peak plastic strain is still below the failure strain limit, so that tendon failure has not yet developed. It is noted that the deformed shape and failure mode associated with rebar and tendon rupture illustrated in these figures closely matches that in the 1/4 scale PCCV tests conducted at Sandia (References 2.3.17 and 2.3.18).

Figures 5-15, 5-16, and 5-17 provide similar plots for the analyses to calculate the median pressure capacity at the normal operating condition. Figures 5-18 5-19, and 5-20 provide similar plots for the median pressure analyses for the hydrogen burning condition.

**Table 5-1 Summary of Median Pressure Capacities**

Failure Mode	Failure Pressure (psig)		
	Normal Operating Conditions	Long Term Accident Conditions	Hydrogen Burning Conditions
PCCV Liner Tearing	230.0	223.6	237.7
PCCV Rebar Rupture	250.0	243.6	247.7
PCCV Tendon Rupture	248.0	246.0	249.0
PCCV Concrete	252.0	255.6	253.7



**Figure 5-12 Accumulated Plastic Strain in Liner, Median Pressure Capacity for Long Term Accident Condition**



**Figure 5-13 Maximum Principal Concrete Strains, Median Pressure Capacity for Long Term Accident Condition**

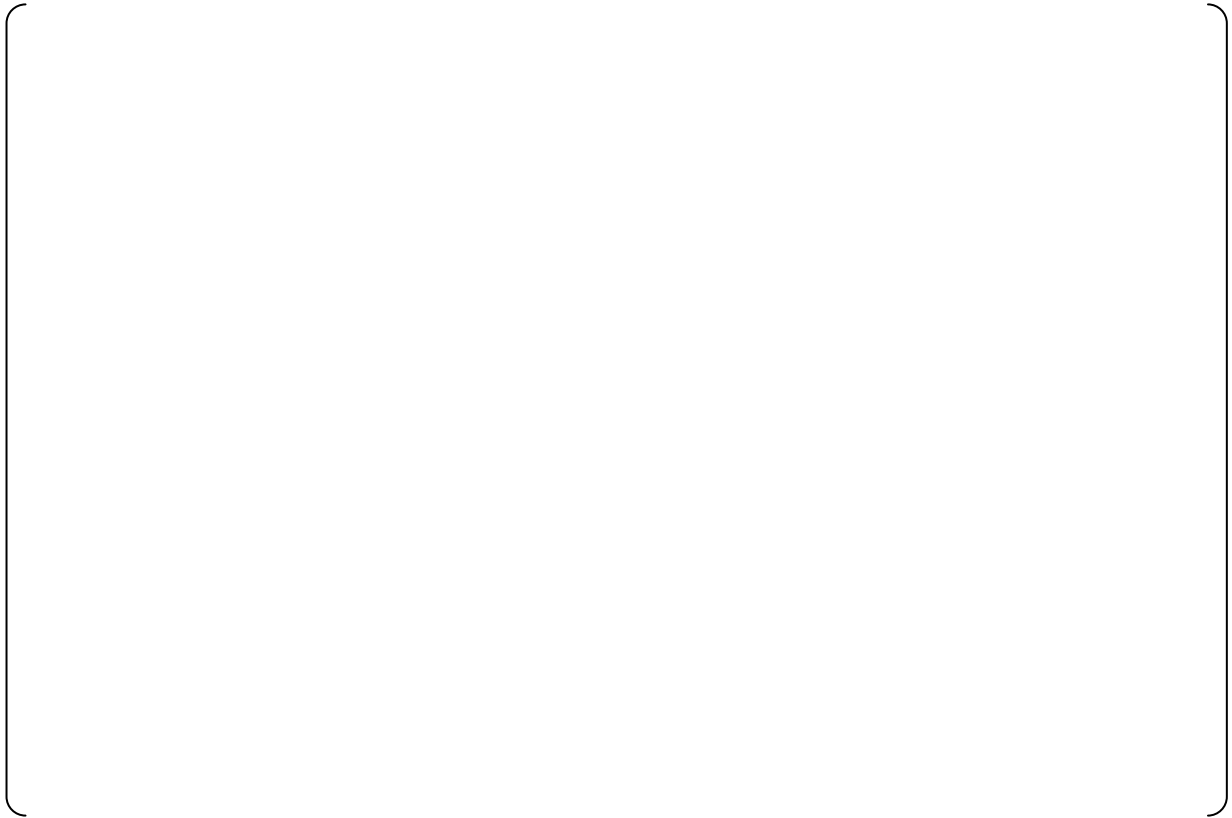


**Figure 5-14 Accumulated Plastic Strain in Hoop Tendons, Median Pressure Capacity for Long Term Accident Condition**

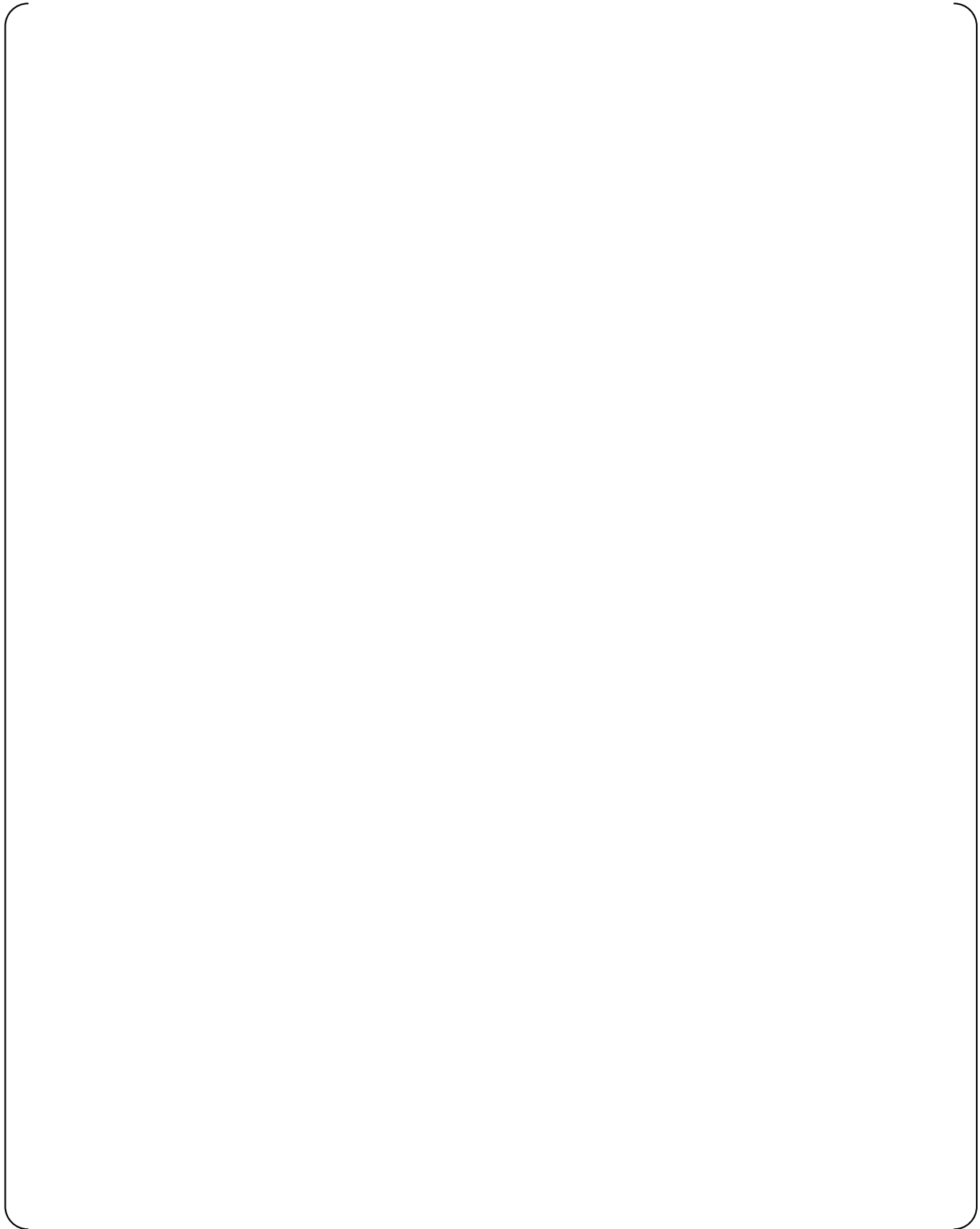


**Figure 5-15 Accumulated Plastic Strain in Liner, Median Pressure Capacity for Normal Operating Condition**

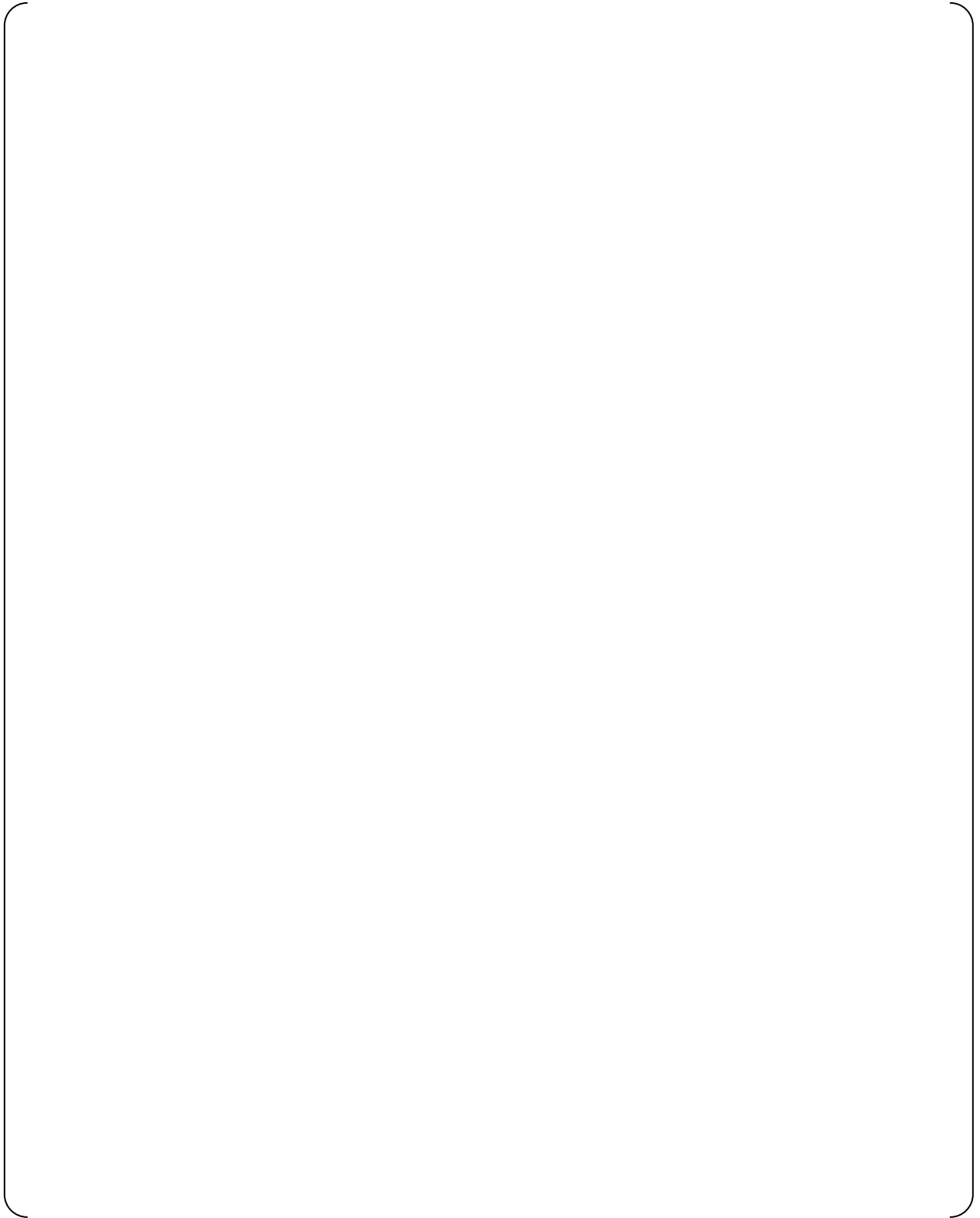


**Figure 5-16 Maximum Principal Concrete Strains, Median Pressure Capacity for Normal Operating Condition**



**Figure 5-17 Accumulated Plastic Strain in Hoop Tendons, Median Pressure Capacity for Normal Operating Condition**

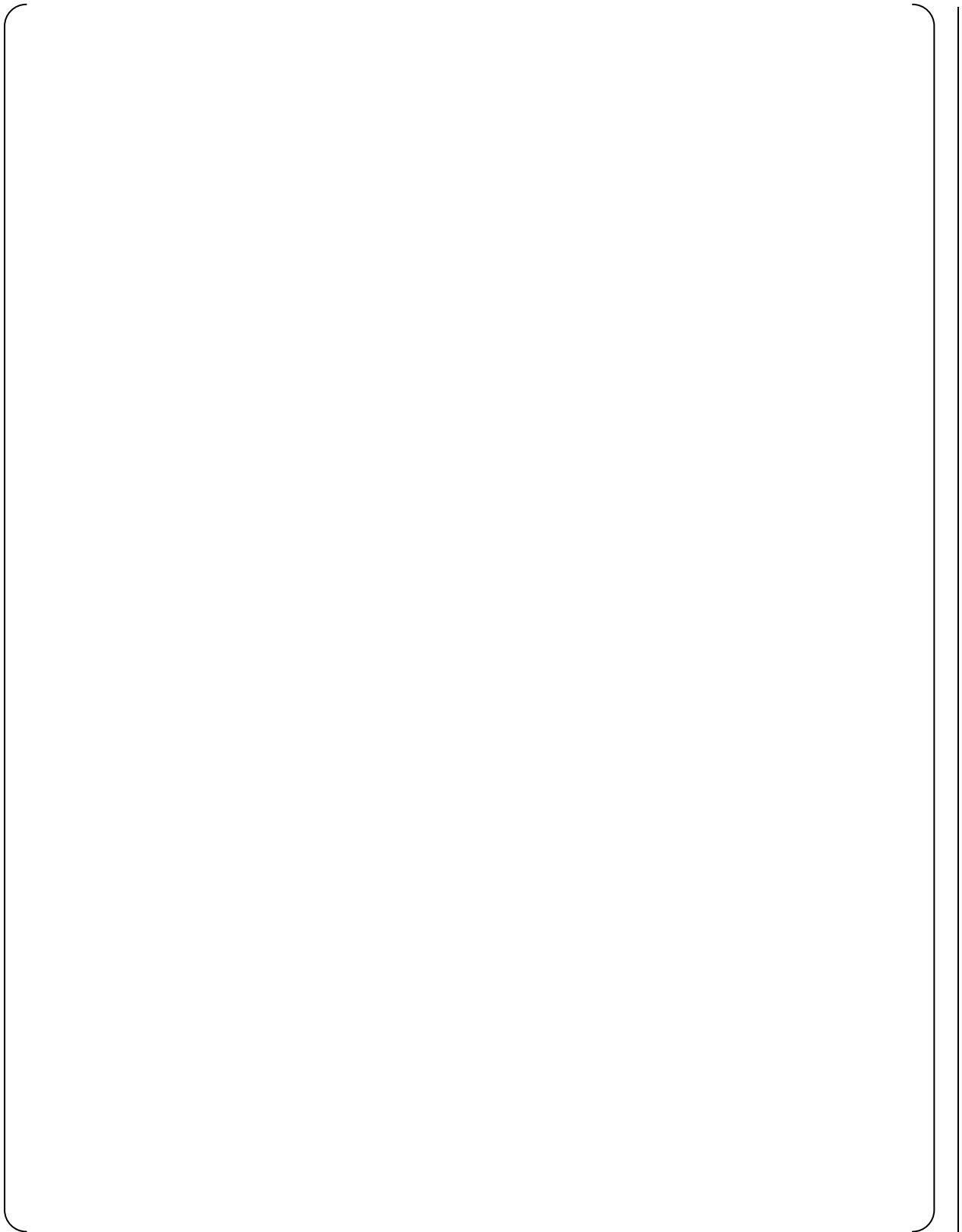


**Figure 5-18 Accumulated Plastic Strain in Liner, Median Pressure Capacity for Hydrogen Burning Condition**

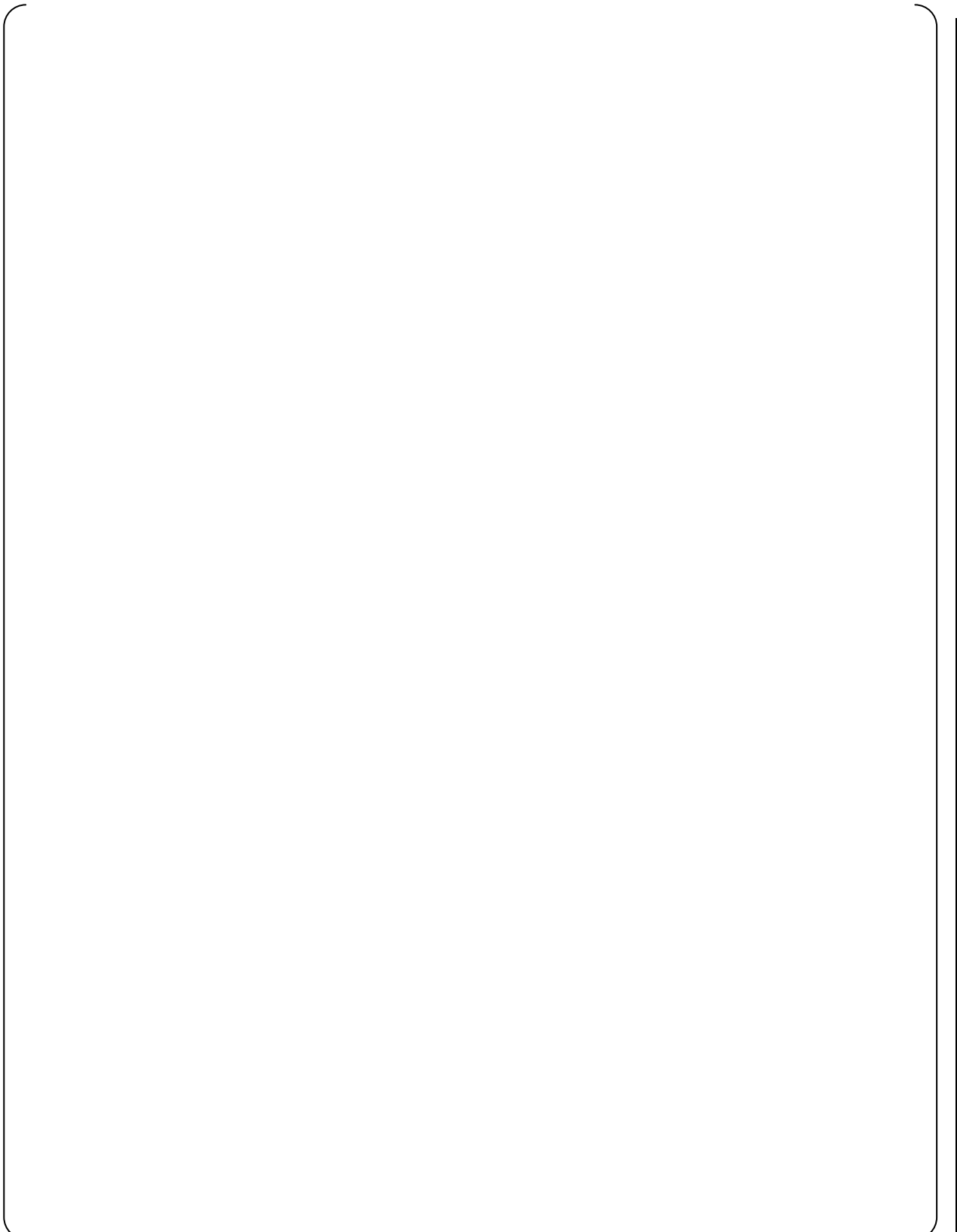


**Figure 5-19 Maximum Principal Concrete Strains, Median Pressure Capacity for Hydrogen Burning Condition**



**Figure 5-20 Accumulated Plastic Strain in Hoop Tendons, Median Pressure Capacity for Hydrogen Burning Condition**

#### 5.4 Evaluation for Uncertainty

The evaluation of uncertainty to determine the variance in the pressure capacity is performed with the global stress model using the temperature distribution for the LTA condition. It is assumed that the uncertainty due to material property and failure criteria variations does not change significantly for the other temperature conditions, just the median pressure capacity. Analyses are performed using variations for each parameter determined to have a significant effect on the pressure capacity as described in Sections 4.3 and 4.4. For the global model analyses, these significant parameters are 1) concrete strength and stiffness, 2) the effect of temperature on concrete properties, 3) the rebar material properties, 4) the tendon prestressing level (see discussion in section 5.1), 5) the tendon material properties, 6) the rebar rupture strain, 7) the tendon rupture strain, 8) the liner rupture strain, and 9) the concrete failure strain. The first 5 parameters are variations in material properties, and for each material property parameter, an additional analysis is performed using the 95% confidence value of that property along with the median values of all other properties. The resulting pressure capacity is then used to determine the variation in the pressure capacity due to uncertainty with this material property. For example the variance in the calculated pressure capacity for liner tearing due to uncertainty in rebar yield is calculated as

$$\beta_s^{rebar-yield} = \frac{\text{Ln}(217.6 / 223.6)}{-1.645} = .0165$$

where 223.6 is the median pressure capacity using median values of all parameters, and 217.6 is the calculated pressure capacity using the 95% confidence value for rebar plastic properties and median values for all other material properties.

The last 4 significant parameters consider uncertainty in the failure criteria used to establish the pressure capacity, and in a similar fashion, the variation in the pressure capacity is determined based on the 95% confidence value of each significant failure criterion parameter along with the median values of all other parameters. In this case, a new analysis does not have to be performed, rather the results of the analysis using all median values are re-evaluated for the pressure capacity using the 95% confidence value of each failure criteria. The variance due to the uncertainty in each failure criteria is then calculated in a similar fashion as above based on the variation in the pressure capacity. For example the variance in the calculated pressure capacity for PCCV rebar rupture due to uncertainty in rebar failure strain is calculated as

$$\beta_f^{rebar-rupture} = \frac{\text{Ln}(217.6 / 243.6)}{-1.645} = .0686$$

where 243.6 is the median pressure capacity using median values of all parameters, and 217.6 is the calculated pressure capacity using the 95% confidence value for the rupture strain of the rebar and median values for all other parameters.

Table 5-2 summarizes the variations performed and the corresponding pressure capacities for each failure mode. Note that variations in failure criteria generally affect only the failure mode associated with that failure parameter since the failure modes are considered independent of each other. The variance calculated for each parameter variation as described above is then combined together along with the modeling variance using the Square Root of the Sum of the Squares to define a composite variance on the pressure capacity for that failure mode. Note that the variation due to modeling uncertainty does depend on temperature as described in

## Section 4.5.

**Table 5-2 Summary of Uncertainty Evaluations in Global Modeling**

Variation Considered (Using Long Term Accident Conditions)	Failure Pressure (psig)			
	Liner Tearing	Rebar Rupture	Tendon Rupture	Concrete Failure
Median Values	223.6	243.6	246.0	255.6
Concrete Strength and Stiffness	222.8	243.0	243.0	251.0
Concrete Temperature Effect	221.6	241.6	241.6	253.0
Rebar Yield & Ultimate Strength	217.6	241.0	239.6	250.0
Tendon Prestressing Level	223.0	243.6	243.6	255.6
Tendon Yield and Ultimate Strength	215.6	237.6	241.6	
Rebar Rupture Strain		217.6		
Tendon Rupture Strain			241.6	
Liner Rupture Strain	217.0			
Concrete Failure Strain				254.0

**5.5 Fragility Summary**

The global modeling is used to establish the ultimate capacity and pressure fragility of the PCCV boundary for the primary containment system. The steady state thermal condition representative of LTA conditions is used as a basis for evaluation of aleatory uncertainties in material properties and failure criteria as described in the above section. The variation of the fragility with temperature is evaluated through consideration of a range in thermal conditions. The failure pressure is characterized using a lognormal probability density function defined as

$$p_f(p) = \frac{1}{p\beta\sqrt{2\pi}} \exp\left[-\frac{1}{2}\left(\frac{\ln(p) - \mu}{\beta}\right)^2\right]$$

where  $p$  is the failure pressure,  $\mu$  is the mean value of the natural log of the failure pressure, and  $\beta$  is the standard deviation of the natural log of the failure pressure. The standard deviation,  $\beta$ , is the composite value calculated as described in the previous section. The corresponding fragility, defined as the cumulative probability of failure for increasing internal pressure, is defined with the integral of the probability density function. The failure pressures are summarized in Table 5-3, which provides the median and 95% confidence values of the failure pressures for the various failure modes and temperature regimes. The 95% confidence value is calculated by evaluating the cumulative probability function for 5% failure probability. The 95% confidence value is the pressure value such that there is a 95% confidence that the actual failure pressure will be higher. The pressure fragilities with

temperature are plotted in Figures 5-21, 5-22, 5-23, and 5-24, for liner tearing, rebar failure, tendon failure, and concrete failure, respectively.

**Table 5-3 Summary of Pressure Fragility from Global Modeling**

Failure Mode and Thermal Condition	Failure Pressure (psig)	
	Median	95% HC
PCCV Liner Tearing		
Normal Operating	230.0	184.9
Long Term Accident	223.6	176.0
Hydrogen Burning	237.7	183.1
PCCV Rebar Rupture		
Normal Operating	250.0	195.9
Long Term Accident	243.6	187.2
Hydrogen Burning	247.7	186.6
PCCV Tendon Rupture		
Normal Operating	248.0	200.0
Long Term Accident	246.0	194.2
Hydrogen Burning	249.0	192.3
PCCV Concrete Failure		
Normal Operating	252.0	203.7
Long Term Accident	255.6	202.2
Hydrogen Burning	253.7	196.4

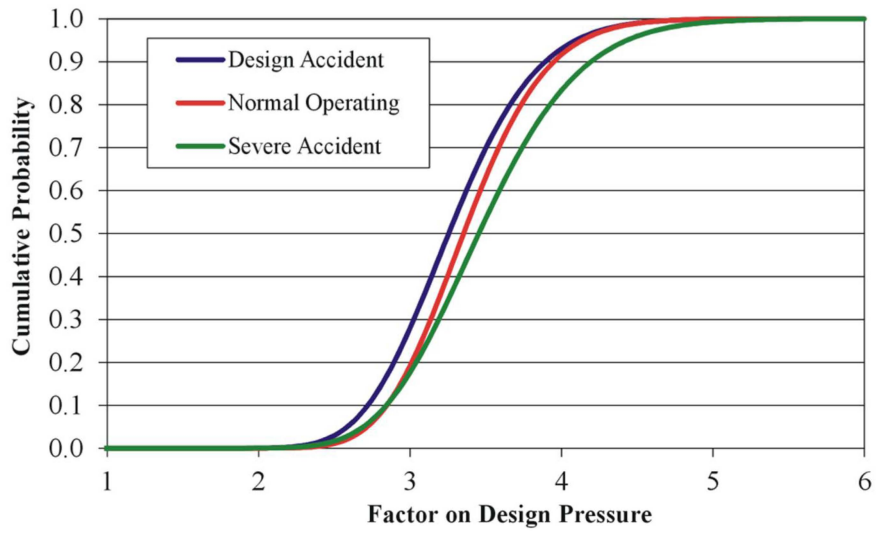


**Figure 5-21 Pressure Fragility with Temperature for PCCV Liner Tearing**

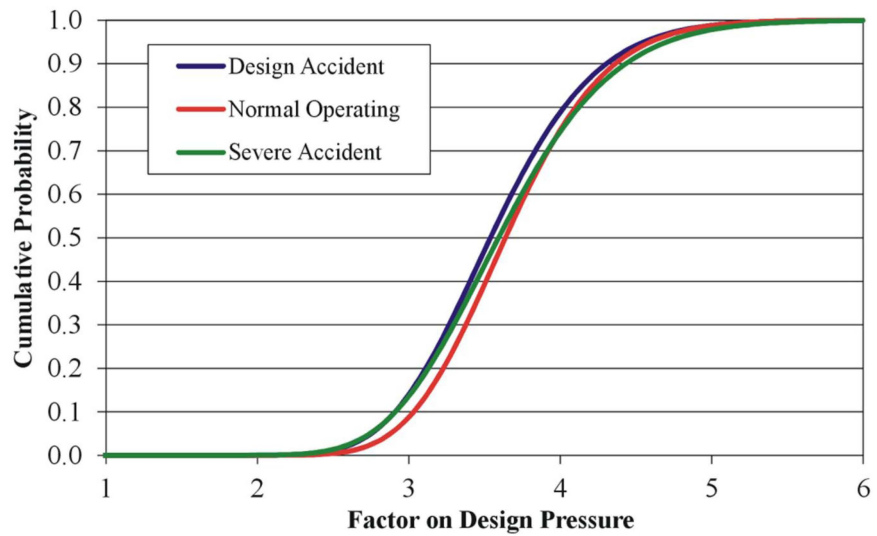


**Figure 5-22 Pressure Fragility with Temperature for PCCV Rebar Failure**

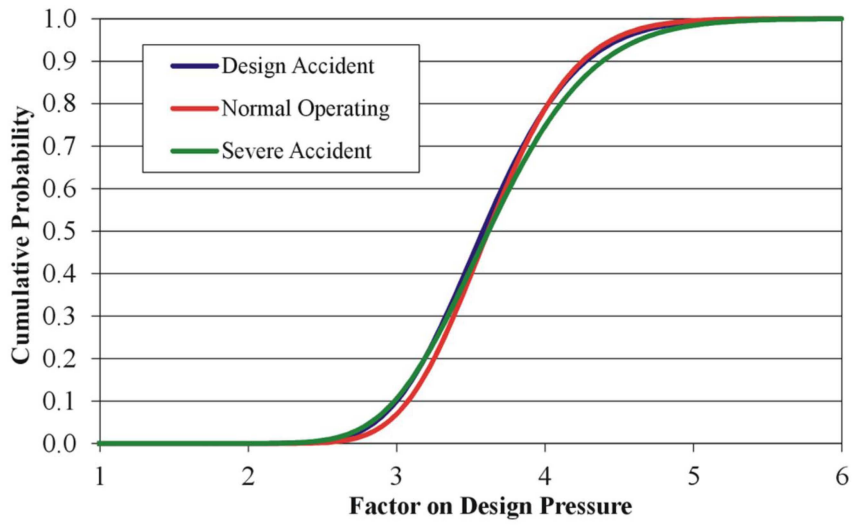


**Figure 5-23 Pressure Fragility with Temperature for PCCV Tendon Failure**

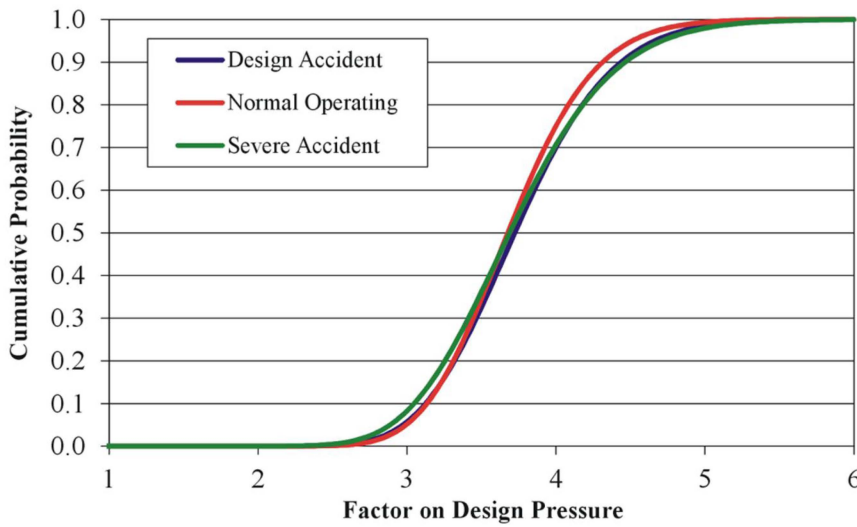


**Figure 5-24 Pressure Fragility with Temperature for PCCV Concrete Failure**

## 6.0 EQUIPMENT HATCH

### 6.1 Model Description

A detailed local model of the EH and a portion of the surrounding PCCV wall is constructed to evaluate the pressure fragilities due to local failure modes associated with the EH components. Test data for the SNL ¼ scale PCCV pressure tests (Reference 2.3.17) show that the personnel ALs and major pipe penetrations do not fail before the liner tearing. This test also indicated that the EH components would not fail before liner tearing, but the scaled configuration of the EH in the test is not considered a good simulation of the EH in the US-APWR design. Thus, local modeling of the EH is performed to establish the pressure fragility of this major penetration. The EH closure is a pressure-seating design with the closure cover on the inside of containment. The following local failure modes are considered in the detailed local model,

- Yielding and rupture of reinforcing bars around the EH
- Yielding and rupture of tendons around the EH
- Failure of concrete around the EH penetration, including shear failure along the sleeve
- Tearing of liner at thickened steel sections around EH
- Tearing of EH steel components
- Yielding and rupture of EH cover bolts due to flange rotation and ovalization
- Rupture or buckling of EH cover

The local modeling for the EH model, including a section of the PCCV wall around the penetration, is illustrated in the following figures. Figure 6-1 provides overall inside and outside views of the concrete and steel components. The liner is modeled with plate elements with common nodes to the concrete surface without explicitly including the anchorage components in the model. Figure 6-2 provides a cut section view illustrating the thickened concrete section. Figure 6-3 provides a close-up view of the modeling used for the bolted flange connection for the hatch cover. The closure bolts are modeled with beam elements with the appropriate length, cross-sectional area, connections, and initial prestress. A contact surface between the flanges is used to allow flange slippage or separation to develop as appropriate. A friction coefficient of 0.42 is used between these surfaces based on Reference 2.1.2. This modeling includes the effects of flange rotation and relative movement between the flanges due to ovalization of the EH penetration. Yielding and rupture of the cover closure bolts due to flange rotation and slippage is used as the metric in determining pressure capacity for this failure mechanism. Figure 6-4 illustrates the shear studs on the outside of the sleeve and also the tendons included in the local model. The reinforcement in the local model is the same as discussed in Section 5-1 for the global model. Displacement boundary conditions, extracted from the global model, are imposed on the cut sections of the PCCV wall in the local model. This enforces the deformation patterns from the global response of the containment system on the local model while capturing more refinement in the structural response of the EH components. A thermal analysis, using a more refined local thermal model consistent with that performed for the global model, is performed for the local model to establish the temperature distributions in the refined mesh of the local model. The thermal and pressure loads are incrementally applied in coordination with the displacement boundary conditions for the same loading states in the global model to evaluate the failure modes and failure pressure levels for the EH components.

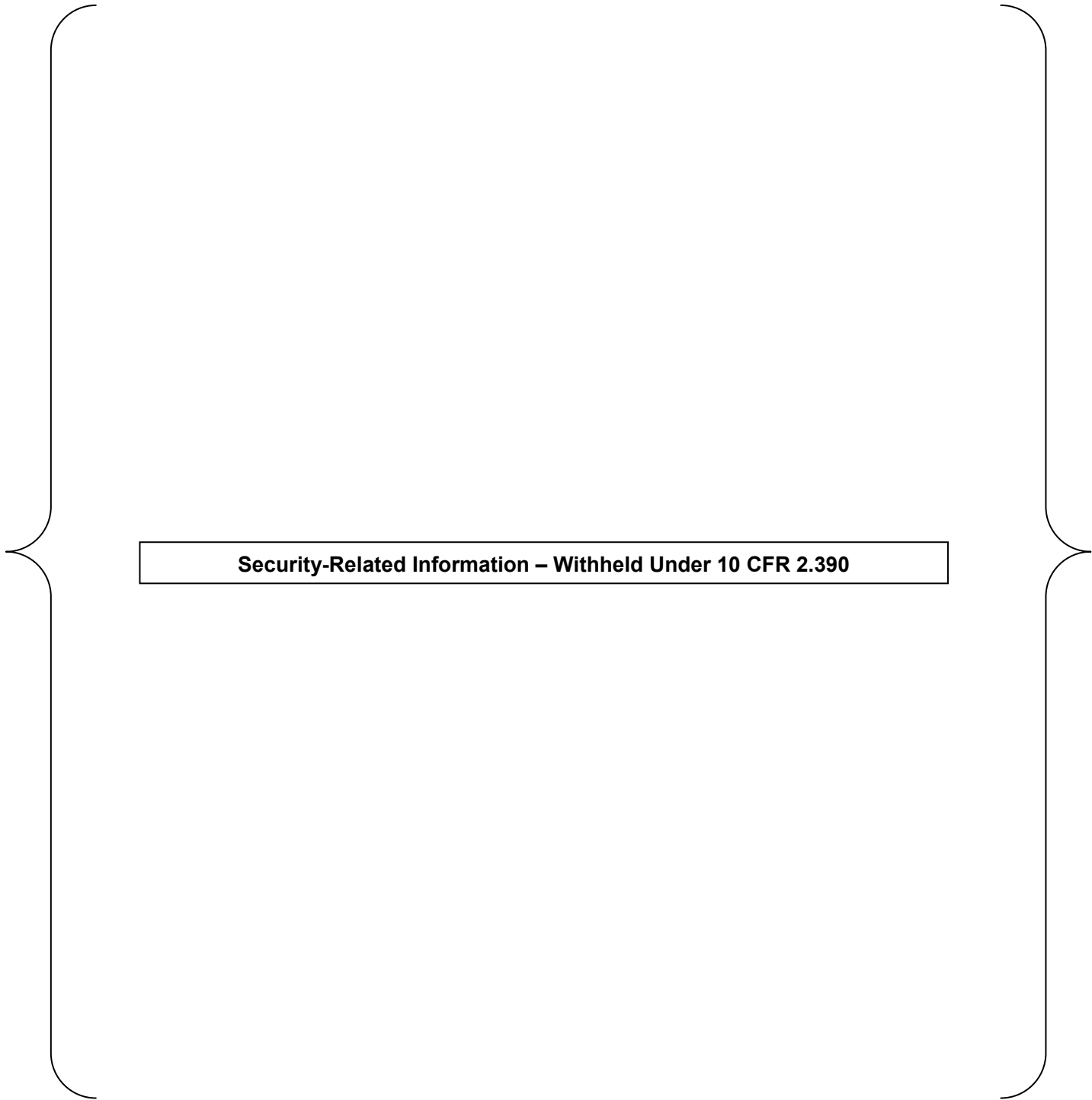


**Figure 6-1 Local Model of Equipment Hatch**

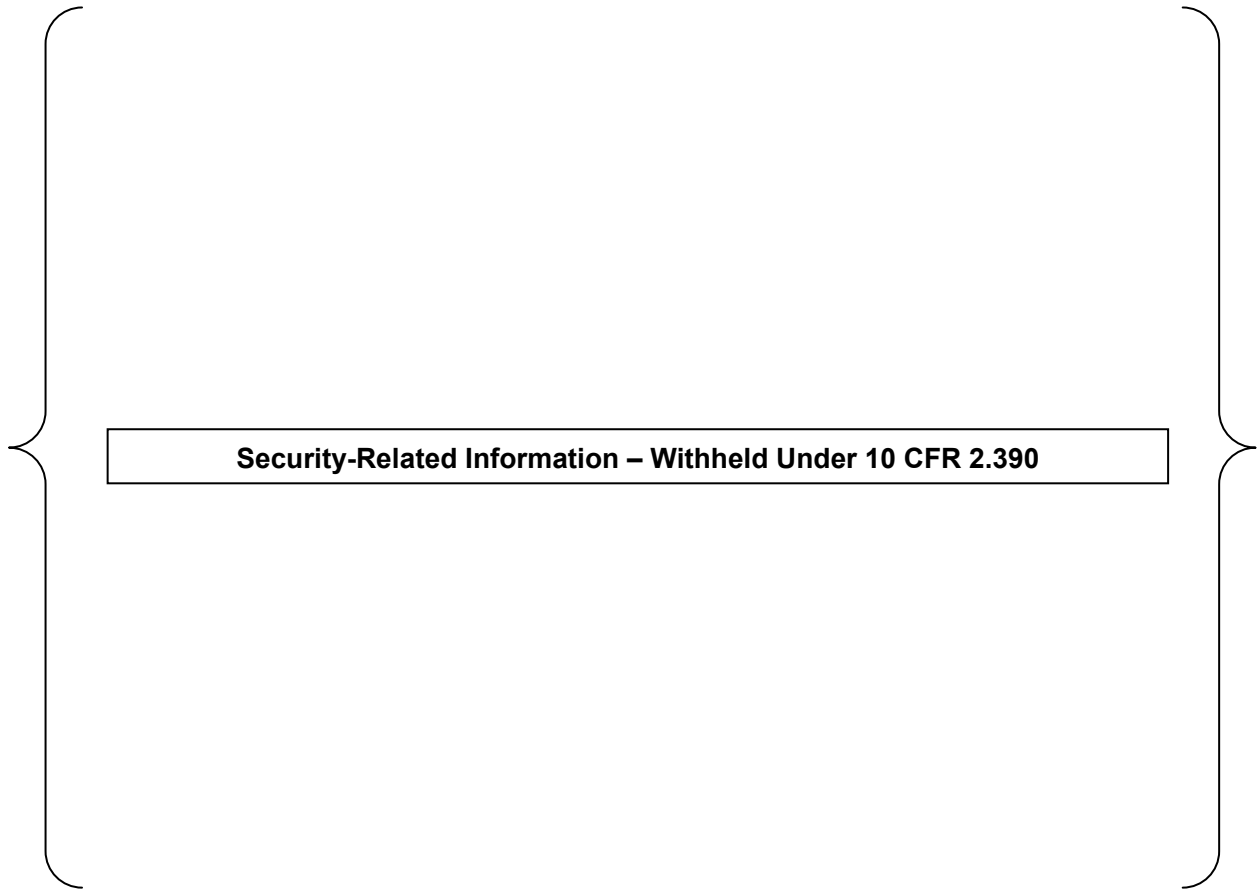


**Figure 6-2 Local Model of Equipment Hatch, Cut Section View**

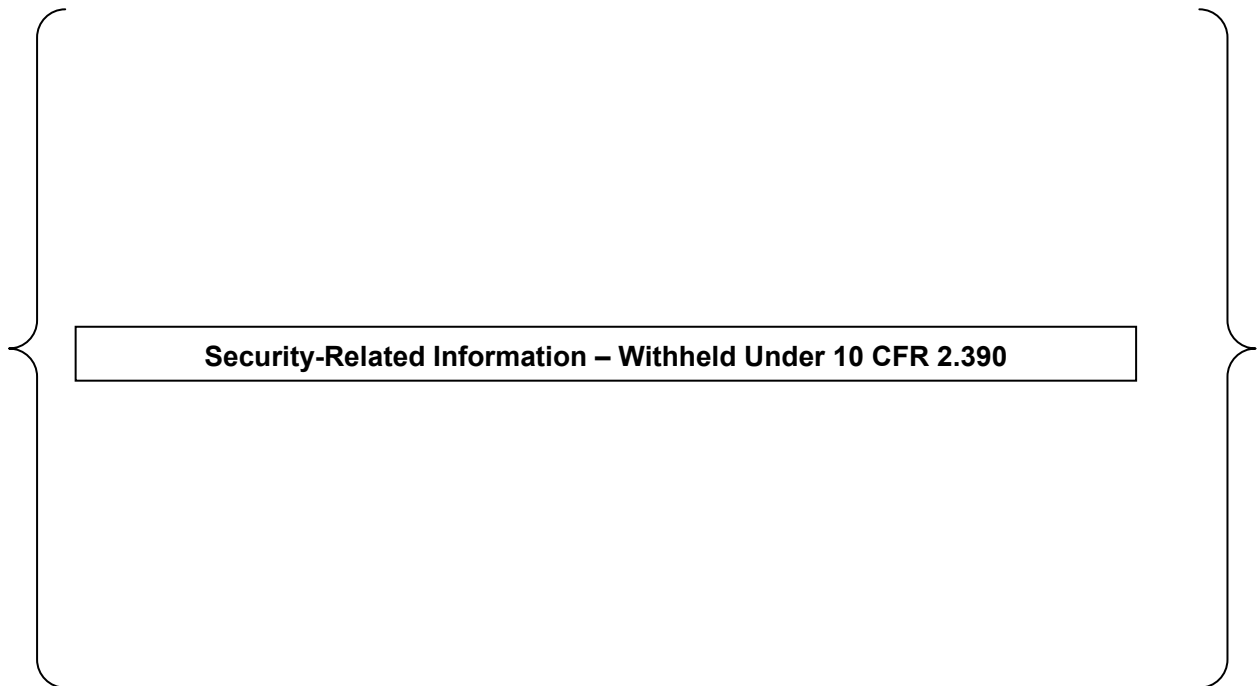


**Figure 6-3 Local Model of Equipment Hatch, Close-up of Bolted Flange**



**Figure 6-4 Local Model of Equipment Hatch, Studs and Tendons**

## 6.2 Thermal Analyses

A local thermal model is used to develop the temperature distributions for the local stress model in performing the pressure capacity analyses. The local thermal model has double mesh refinement in all directions (each 20-node brick replaced with eight 8-node bricks) consistent with that described for the global modeling. The temperature distributions determine the variation of material properties with temperature within the structure and thermal stresses based on the changes from reference temperature and restraint against thermal expansion or contraction. The 3 thermal conditions described in Section 4.6 are used as the basis for evaluating the variation of pressure capacity with temperature. The temperature distributions associated with these 3 thermal conditions for the local EH model are illustrated in Figure 6-5 for normal operating condition, Figure 6-6 for long term design basis accident condition, and Figure 6-7 for the hydrogen burning thermal condition. The temperature distribution for the normal operating condition is based on a steady state solution with the PCCV atmosphere at 105 °F. The temperature distribution for the LTA thermal condition is based on a steady state solution with the PCCV atmosphere at 438 °F. The temperature distribution for the hydrogen burning thermal condition is based on a transient solution when the PCCV atmosphere and liner reach 1000 °F for a postulated hydrogen burn scenario. Due to the orientation of the plate element outward normal, two figures are provided for the hydrogen burn thermal conditions; one showing the temperatures for inside surface of liner and one showing the exposed surfaces of equipment hatch and cover. All 3 thermal conditions are considered to occur during extreme winter ambient conditions when the air temperature is -40 °F.

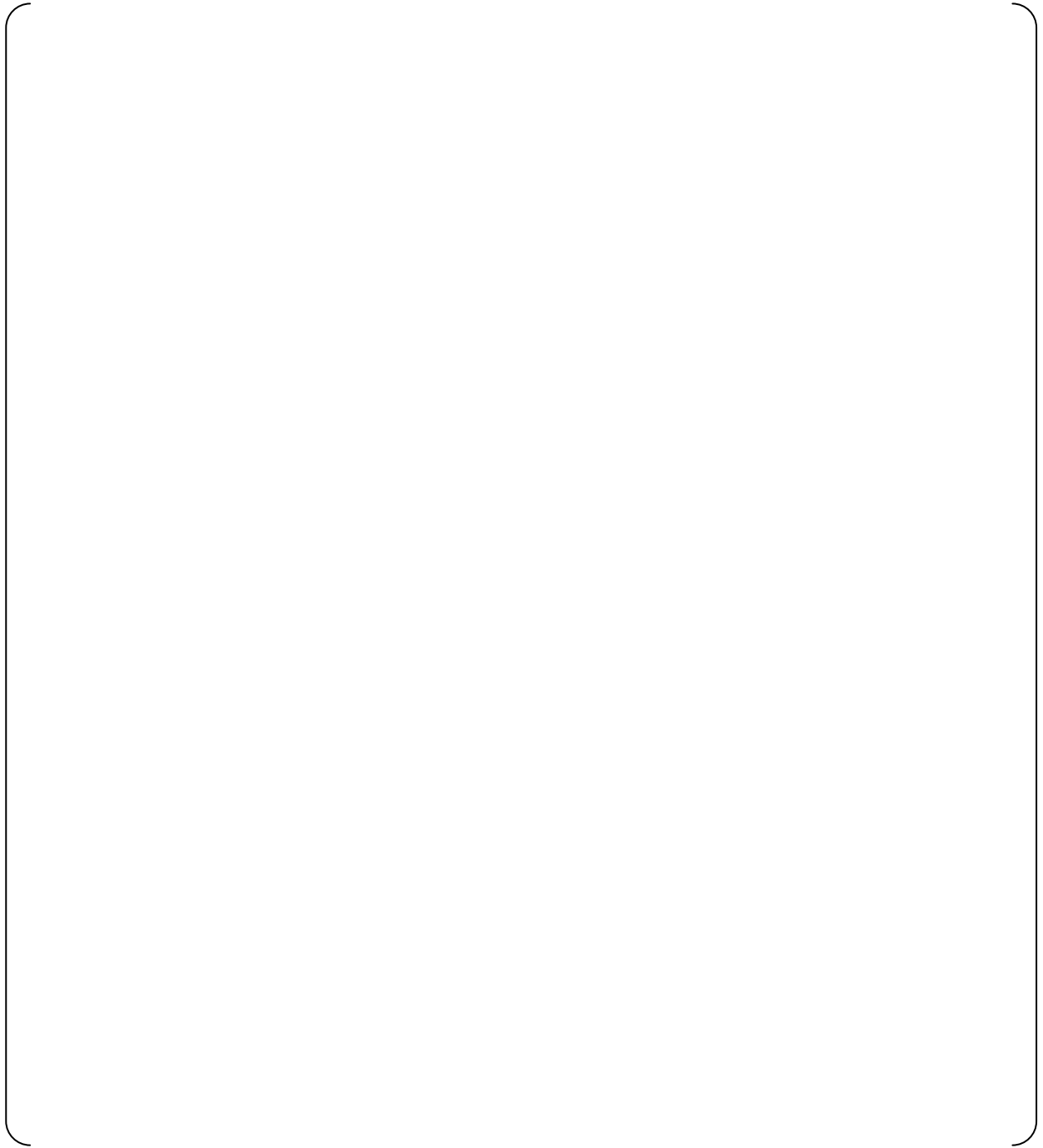


**Figure 6-5 Temperature Distribution in EH Model for Normal Operating Condition**

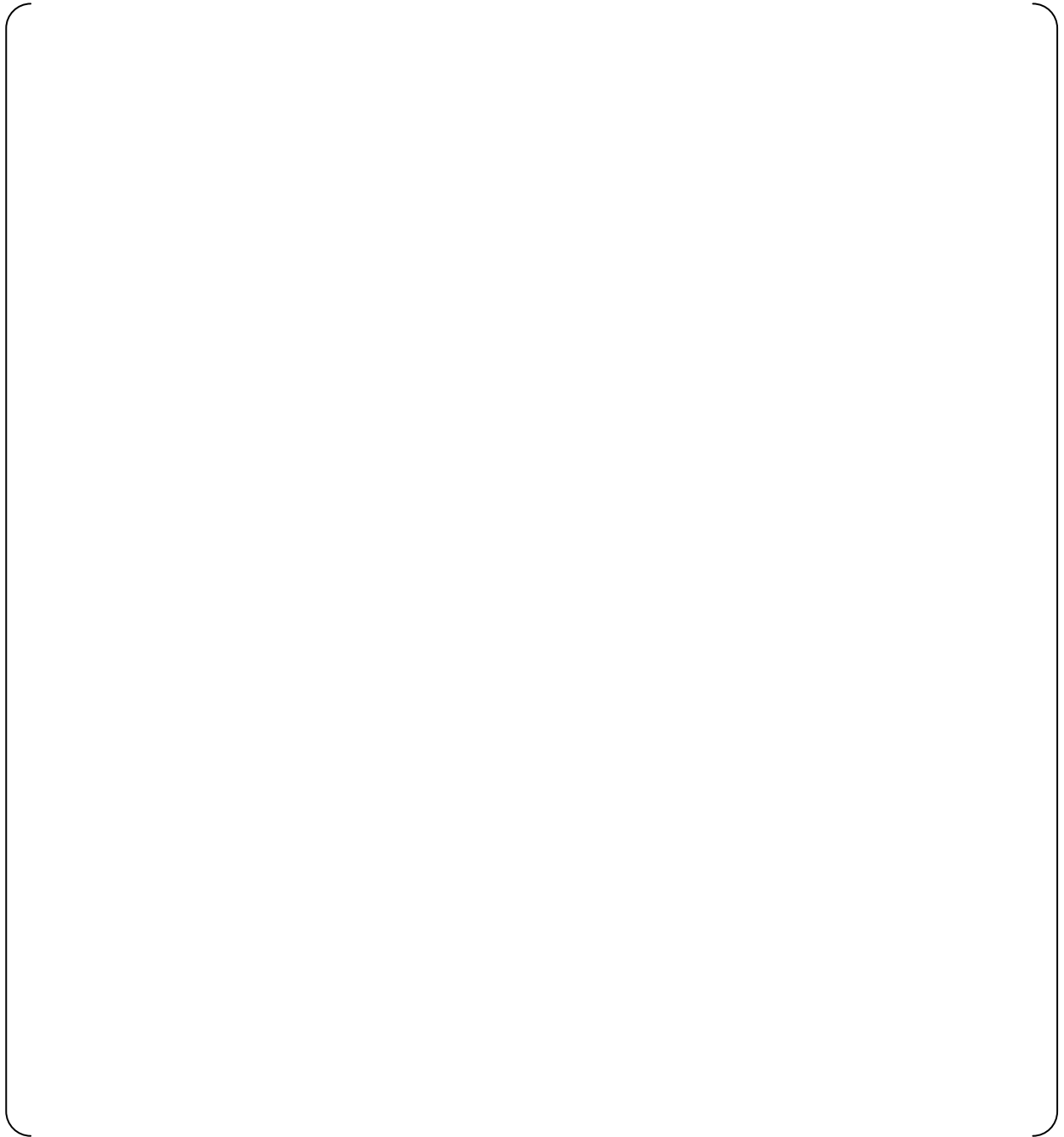


**Figure 6-6 Temperature Distribution in EH Model for Long Term Accident Condition**

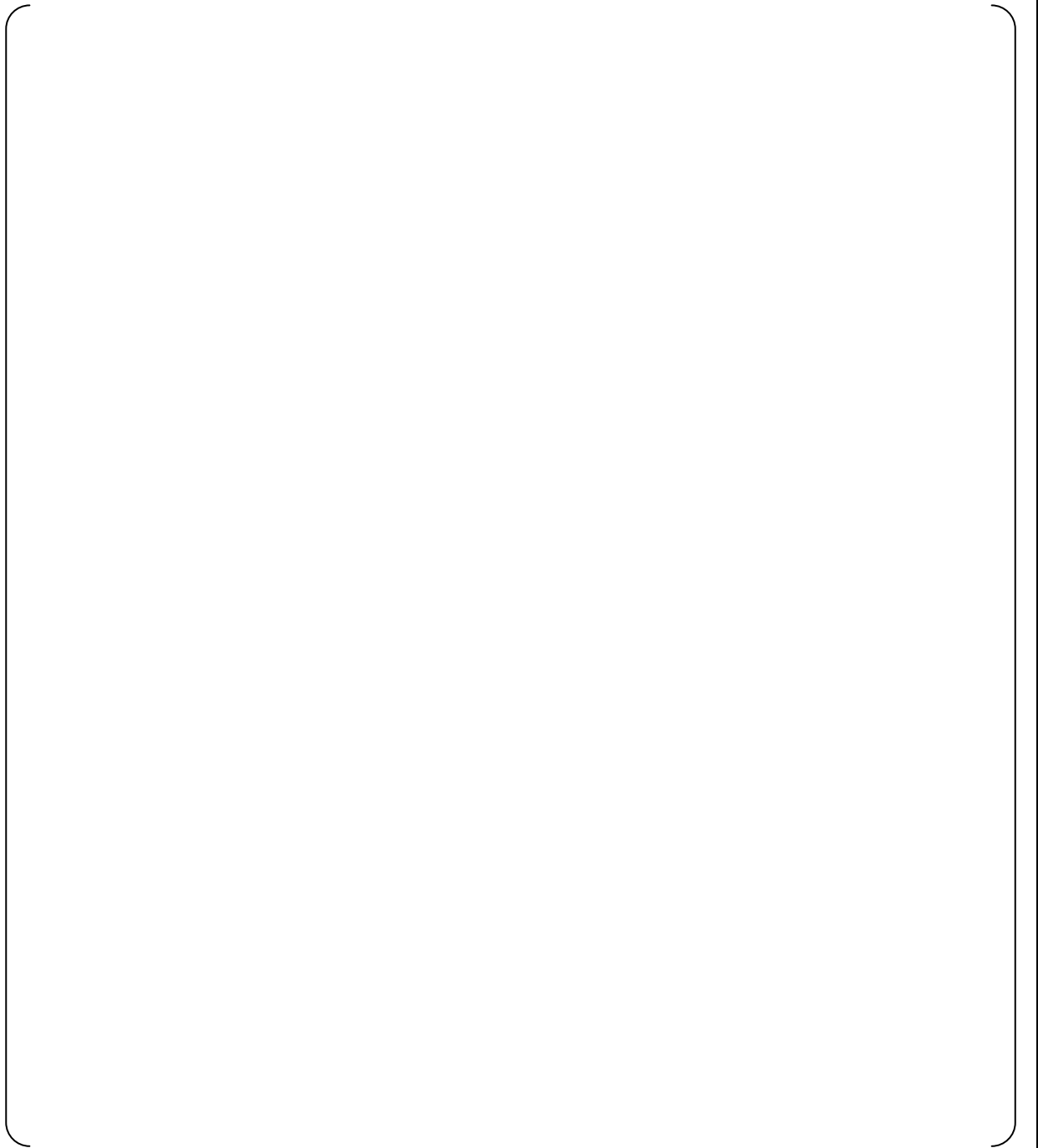


**Figure 6-7 Temperature Distribution in EH Model for Hydrogen Burning Condition**

### 6.3 Median Capacity Analyses

The median pressure capacity for the EH components is determined using the EH local model along with median values of all material properties and failure criteria. The median pressure capacity is calculated for each of the 3 thermal conditions described in Section 4.6 and illustrated in the previous section. For each median pressure capacity analysis, the failure pressure for each mode of failure is determined based on the corresponding failure criteria, for example, monitoring liner plastic strains to determine the pressure where liner tearing initiates. The failure pressures for each failure mode are determined independently, that is, the structural effect or consequences due to initiation of any one failure mode does not influence the next failure mode. For example, when the rupture strain of a rebar has been reached, the pressure associated with rebar failure is determined, but the rebar continues to plastically deform until the next failure mode is reached. This complies with the basic assumptions needed for parameter independence in the probabilistic assessment.

Table 6-1 summarizes the median pressure capacities calculated for the various failure modes related to the EH for the 3 thermal conditions. Note that some values have approximated or greater than signs indicating that judgment or extrapolation was used since the associated failure criteria have not been realized for the final pressure reached in the analysis. These failure modes were determined to be non-controlling for the EH local modeling. The following figures illustrate the performance of the EH during over-pressurization for the steady state LTA thermal condition. Figure 6-8 provides a contour plot for maximum principal strains in the concrete as representative of concrete cracking damage with deformations magnified by 10. In this figure, the contour limit is set to 2% to highlight the areas of more extensive cracking to illustrate the cracking damage that develops leading to yield and rupture of rebar and tendons. This figure indicates extensive cracking on the outside face, especially near the top and bottom of the penetration, due to outward bulging at this pressure level. The ovalizing deformation of the EH penetration is also illustrated. Figure 6-9 provides a contour plot for the minimum principal stress in the concrete as representative of the concrete compressive stress with deformations magnified by 10. This figure indicates some local crushing has developed on the inside face around the EH at this pressure level. Figure 6-10 provides a contour plot for the shear strain in the concrete for a cross section through the EH with deformations magnified by 10. The contour limits have been set to highlight the areas nearing the shear capacity of the section. The gray or black color would need to extend all the way through the section and around the EH for initiation of a shear plug type failure. Note that the outward bulging induces some compression around the EH sleeve on the inner surface to help resist the shear plug failure. These figures for concrete performance indicate significant damage is developing in the concrete at these pressures, but that a limiting pressure capacity due to failure of the concrete or with the EH anchorage to the concrete does not develop.

Figure 6-11 provides a contour plot for accumulated plastic strain in the liner. For the pressure level shown, the peak plastic strain is shown to be above the failure limit so that liner tearing has initiated along the line at the geometric discontinuity for the thickened concrete section. This figure confirms the finding in the global analysis that liner tearing will initiate at the liner discontinuity at the concrete thickness change before tearing in the liner at the connection with the EH steel components. Figure 6-12 provides a contour plot for plastic strain in the steel components of the EH. This figure shows that the higher strains develop around the edge of the sleeve on the outside of the EH due to bulging and concrete damage on the outer face. While tearing may initiate here first, this is not considered failure for

pressure capacity because it does not compromise the pressure boundary. Figure 6-13 provides a contour plot for plastic strain in the tendons at the pressure level indicated. In this plot, the peak plastic strain is still below the failure strain limit, so that tendon failure has not yet developed. The pressure capacity due to rebar failure is determined by monitoring the plastic strain in the rebar elements. Similarly, the pressure capacity due to yielding of the EH cover bolts is determined by monitoring the initiation of plastic yielding in the bolt elements.

Figures 6-14 through 6-19 provide similar plots for the analyses for calculating the median pressure capacity at the normal operating condition. Figures 6-20 through 6-24 provide similar plots for the median pressure analyses for the hydrogen burning thermal condition.

It is found that the pressure capacities due to concrete failure, tendon rupture, and bolt yielding (as a result of flange rotation and slippage) are not governing for the EH local modeling, and parameter variations for these failure modes are not considered further in developing the variance in the pressure capacity.

**Table 6-1 Summary of Median Pressure Capacities for Equipment Hatch**

Failure Mode	Failure Pressure (psig)		
	Normal Operating Conditions	Long Term Accident Conditions	Hydrogen Burning Conditions
EH Rebar Rupture	236.8	237.4	240.4
EH Tendon Rupture	~263	~251	266.2
EH Liner Tearing	241.5	228	240.7
EH Concrete Failure	~262	>250	>250
EH Bolt Rupture	~275	252	>270
EH Sleeve Tearing	263	251	262
EH Cover Failure	263	252	260



**Figure 6-8 EH Concrete Cracking for Long Term Accident Conditions**



**Figure 6-9 EH Concrete Compressive Stress for Long Term Accident Conditions**



**Figure 6-10 EH Concrete Shear Strain for Long Term Accident Conditions**



**Figure 6-11 EH Liner Plastic Strains for Long Term Accident Conditions**

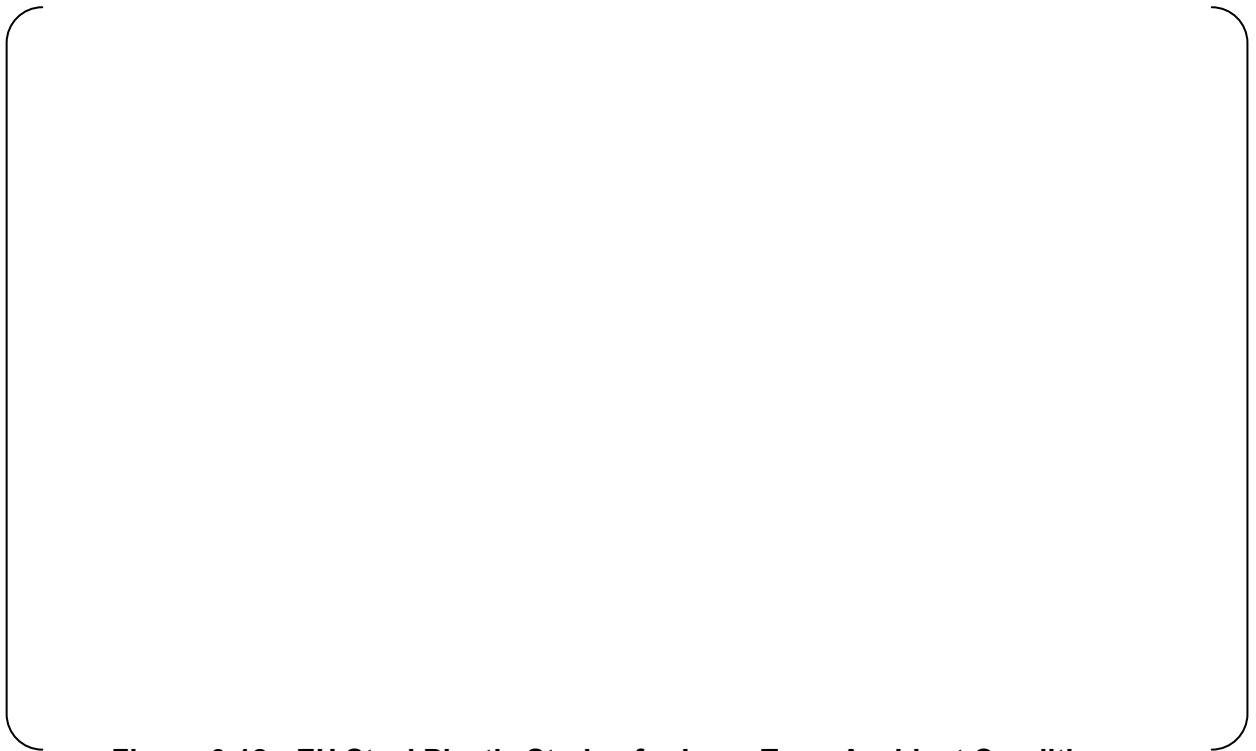


**Figure 6-12 EH Steel Plastic Strains for Long Term Accident Conditions**



**Figure 6-13 EH Tendon Plastic Strains for Long Term Accident Conditions**



**Figure 6-14 EH Concrete Cracking for Normal Operating Conditions**



**Figure 6-15 EH Concrete Compressive Stress for Normal Operating Conditions**

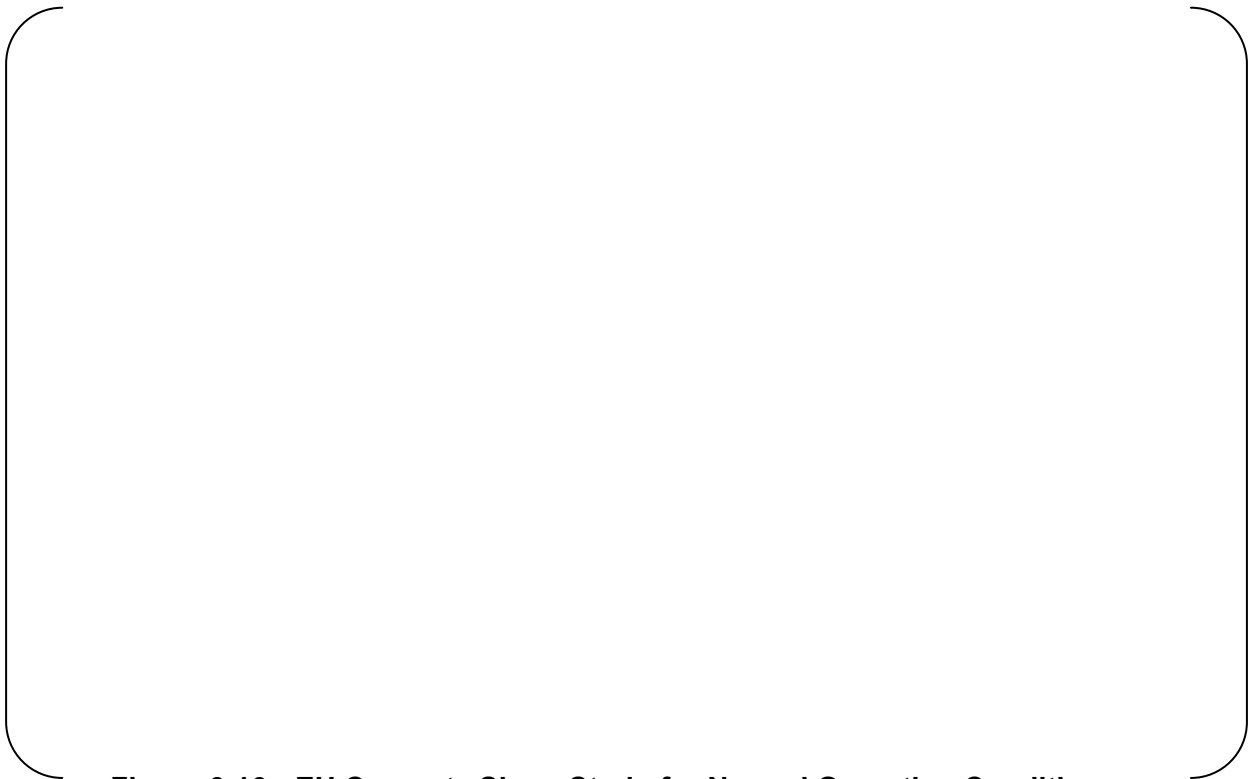


**Figure 6-16 EH Concrete Shear Strain for Normal Operating Conditions**



**Figure 6-17 EH Liner Plastic Strains for Normal Operating Conditions**



**Figure 6-18 EH Steel Plastic Strains for Normal Operating Conditions**



**Figure 6-19 EH Tendon Plastic Strains for Normal Operating Conditions**



**Figure 6-20 EH Concrete Cracking for Hydrogen Burning Conditions**



**Figure 6-21 EH Concrete Compressive Stress for Hydrogen Burning Conditions**



**Figure 6-22 EH Concrete Shear Strain for Hydrogen Burning Conditions**



**Figure 6-23 EH Liner Plastic Strains for Hydrogen Burning Conditions**



**Figure 6-24 EH Steel Plastic Strains for Hydrogen Burning Conditions**

#### 6.4 Evaluation for Uncertainty

The evaluation of uncertainty to determine the variance in the pressure capacities associated with the EH is determined with the local EH model using the temperature distribution for the LTA condition. It is assumed that the uncertainty due to material property and failure criteria variations does not change significantly for the other temperature conditions, that is, only the median pressure capacity changes significantly with temperature. Analyses are performed using variations for each parameter determined to have a significant effect on the pressure capacity as described in Sections 4.3 and 4.4. For the local EH model analyses, these significant parameters are 1) the steel properties of the EH components (including temperature effects), 2) the tendon prestressing level, 3) the closure bolt prestress level, 4) the bolt material properties, 5) the rebar rupture strain, 6) the liner rupture strain, and 7) the steel rupture strain. The first 4 parameters are variations in material properties and prestressing level, and for each parameter, an additional analysis is performed using the 95% confidence value of that property along with the median values of all other properties. The resulting pressure capacity is then used to determine the variation in the pressure capacity due to uncertainty with this material property. For example the variance in the calculated pressure capacity for tearing in the EH steel components due to uncertainty in the steel properties is calculated as

$$\beta_s^{steel-yield} = \frac{\text{Ln}(226/251)}{-1.645} = .0638$$

where 251 is the median pressure capacity using median values of all parameters, and 226 is the calculated pressure capacity using the 95% confidence value for the plastic properties of the steel and median values for all other parameters.

The last 3 significant parameters consider uncertainty in the failure criteria used to establish the pressure capacity, and in a similar fashion, the variation in the pressure capacity is determined based on the 95% confidence value of each significant failure criterion parameter along with the median values of all other parameters. In this case, a new analysis does not have to be performed, rather the results of the analysis using all median values is re-evaluated for the pressure capacity using the 95% confidence value of each failure criteria. The variance due to the uncertainty in each failure criteria is then calculated in a similar fashion as above based on the variation in the pressure capacity. For example the variance in the calculated pressure capacity for EH rebar rupture due to uncertainty in rebar failure strain is calculated as

$$\beta_f^{rebar-rupture} = \frac{\text{Ln}(197.7/237.4)}{-1.645} = .1112$$

where 237.4 is the median pressure capacity using median values of all parameters, and 197.7 is the calculated pressure capacity using the 95% confidence value for the rupture strain of the rebar and median values for all other parameters.

Table 6-2 summarizes the variations performed and the corresponding pressure capacities for each failure mode. Note that variations in failure criteria generally affect only the failure mode associated with that failure parameter since the failure modes are considered to be independent of each other. The variance calculated for each parameter variation as described above is then combined together along with the modeling variance using the Square Root of the Sum of the Squares to define a composite variance on the pressure capacity for

that failure mode. Note that the variation due to modeling uncertainty does depend on temperature as described in Section 4.5.

**Table 6-2. Summary of Uncertainty Evaluations in EH Local Modeling**

Variation Considered (Using Long Term Accident Conditions)	Failure Pressure (psig)			
	EH Liner Tearing	EH Rebar Rupture	EH Sleeve Tearing	EH Cover Failure
All Median Values	228.0	237.4	251.0	252.0
Steel Yield	223.0	224.0	226.0	224.5
Tendon Prestress	226.4	236.0	250.0	251.0
Bolt Prestress	225.0	235.0	249.0	249.0
Bolt Yield	227.5	237.0	249.0	251.0
Rebar Rupture Strain		197.7		
Liner Rupture Strain	217.0			
Steel Rupture Strain			245.1	252.0

## 6.5 Fragility Summary

The local modeling is used to establish the ultimate capacity and pressure fragility for the primary containment system as limited by the EH penetration and components. The steady state thermal condition representative of LTA conditions is used as a basis for evaluation of aleatory uncertainties in material properties and failure criteria as described in the above section. The variation of the fragility with temperature is evaluated through consideration of a range in thermal conditions. The failure pressure is characterized using a lognormal probability density function defined as

$$p_f(p) = \frac{1}{p\beta\sqrt{2\pi}} \exp\left[-\frac{1}{2}\left(\frac{\ln(p) - \mu}{\beta}\right)^2\right]$$

where  $p$  is the failure pressure,  $\mu$  is the mean value of the natural log of the failure pressure, and  $\beta$  is the standard deviation of the natural log of the failure pressure. The standard deviation,  $\beta$ , is the composite value calculated as described in the previous section. The corresponding fragility, defined as the cumulative probability of failure for increasing internal pressure, is defined with the integral of the probability density function. The failure pressures are summarized in Table 6-3, which provides the median and 95% confidence values of the failure pressures for the various failure modes and temperature regimes. The 95% confidence value is calculated by evaluating the cumulative probability function for 5% failure probability. This 95% confidence value is the pressure value such that there is a 95% confidence that the actual failure pressure will be higher. The pressure fragilities with temperature are plotted in Figures 6-25, 6-26, and 6-27, for rebar failure around the EH, tearing of the EH sleeve, and failure of the EH cover, respectively.

**Table 6-3 Summary of Pressure Fragility from EH Local Modeling**

Failure Mode and Thermal Condition	Failure Pressure (psig)	
	Median	95% HC
EH Rebar Rupture		
Normal Operating	236.8	173.2
Long Term Accident	237.4	171.0
Hydrogen Burning	240.4	170.3
EH Sleeve Tearing		
Normal Operating	263.0	202.5
Long Term Accident	251.0	189.7
Hydrogen Burning	262	194.3
EH Cover Failure		
Normal Operating	263.0	201.7
Long Term Accident	252.0	189.8
Hydrogen Burning	260	192.2

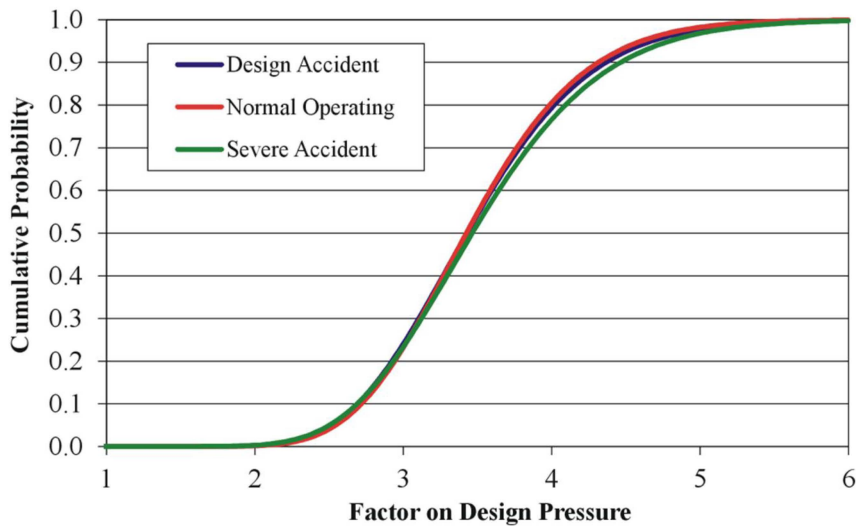


**Figure 6-25 Pressure Fragility with Temperature for EH Rebar Failure**

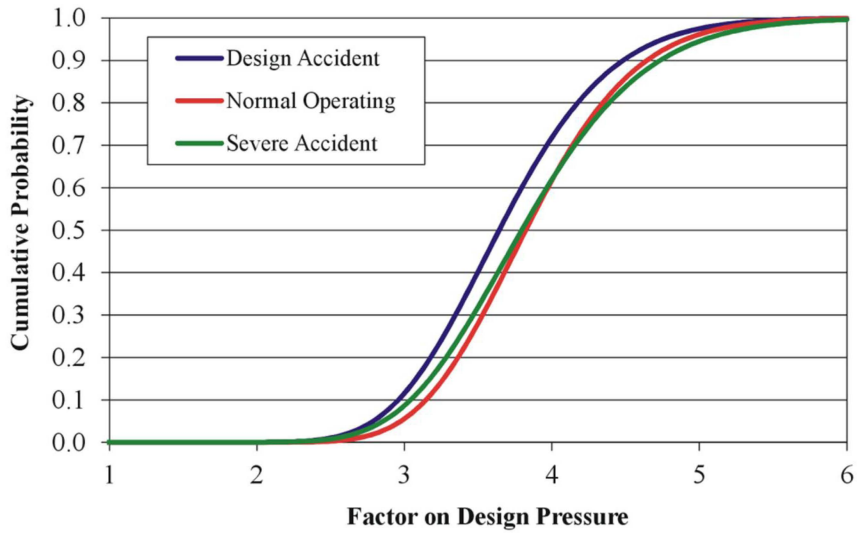


**Figure 6-26 Pressure Fragility with Temperature for EH Sleeve Tearing**

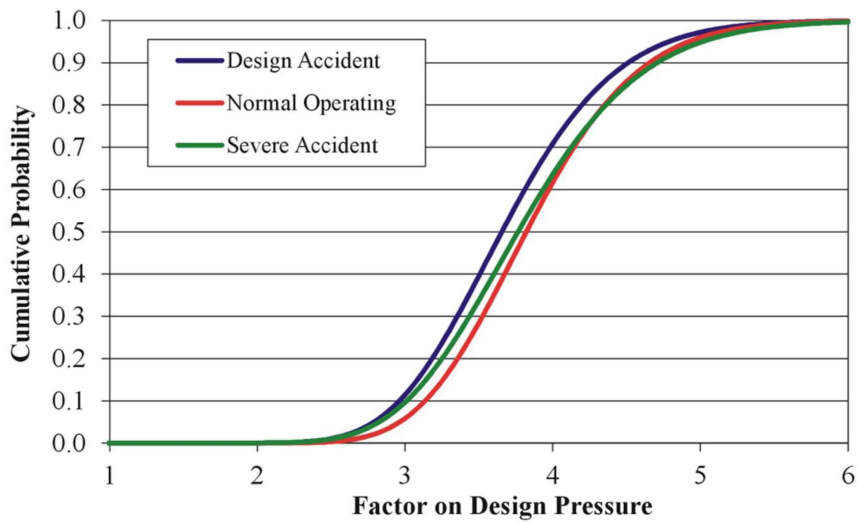


**Figure 6-27 Pressure Fragility with Temperature for EH Cover Failure**

## 7.0 CONCLUSION

As used for the probabilistic risk assessment (PRA), the ultimate capacity of the PCCV was calculated to be 201 psig in design control document (DCD) Chapter 19. The primary purpose of this technical report is to show that the 201 psig capacity is the smaller and more conservative value than the results summarized here from the non-linear analyses. Probabilistic analyses summarized in Section 3.0 show the median pressure capacities determined from the global PCCV modeling and the local EH are higher than 201 psig under all thermal conditions. Deterministic analyses summarized in Appendix B show the pressure capacities of AL, MS/FW and FTT are also higher than 201 psig under all thermal conditions. Therefore, it is concluded that the ultimate capacity of 201 psig (216 psia), used for PRA, is conservative adequate for use.

The analysis performed In Appendix A demonstrates that the liner will remain a leak tight barrier for the internal pressure and temperature associated with an accident where hydrogen is generated due to interaction between fuel cladding and water coolant. Therefore, it is concluded that the pressure capability of the steel lined PCCV is able to meet the requirement in RG 1.136 C.5.B.(2) and DG-1203.

The more likely severe accident challenges for the US-APWR are the cases that containment depressurization functions are available in accordance with the US-APWR PRA evaluation. The containment condition is maintained below the design pressure and temperature within the 24 hours after onset of core damage as well as the period following initial 24 hours after the onset of core damage for these more likely severe accident challenges. Further discussion is described in Appendix C.

# **APPENDIX A**

## **Pressure Integrity for Hydrogen Generated Pressure Loads**

### List of Tables

<u>Table No.</u>	<u>Title</u>	<u>Page</u>
Table A-1	Summary of Factored Load Limits from ASME Subsection CC-3720	87
Table A-2	Summary of Steel Elastic Properties	87
Table A-3	Summary of Steel Plastic Properties for Pressure Integrity	88
Table A-4	Summary of Concrete Properties for Level C Analysis	88
Table A-5	Summary of Pressure at First Yield in Steel Components	89

### List of Figures

<u>Figure No.</u>	<u>Title</u>	<u>Page</u>
Figure A-1	Deformed Shape x50 of PCCV at 162.4 psig Pressure	90
Figure A-2	Contour of Maximum Principal Strain in Liner at 162.4 psig Pressure	90
Figure A-3	Maximum Liner Strains as Function of Pressure	91
Figure A-4	Contour of Minimum Principal Stress in Concrete at 162.4 psig Pressure	91
Figure A-5	Locations of Peak Rebar Stress, 0 to 180 degrees of Model	92
Figure A-6	Locations of Peak Rebar Stress, 180 to 360 degrees of Model	92

## A Pressure Integrity for Hydrogen Generated Pressure Loads

A deterministic analysis is performed to demonstrate that the pressure capability of the steel lined prestressed concrete boundary of the containment system meets the regulatory requirements in 10CFR50.44(c)(5) per Draft Regulatory Guide DG-1203. To meet this requirement, it must be demonstrated that the containment maintains structural integrity for an internal pressure corresponding to an accident resulting in 100% fuel clad-coolant reaction. For the US-APWR, this is an internal pressure of 162.4 psig or 2.39 times the design pressure. Table A-1 summarizes the Factored Load strain limits for the liner that are used for verifying the structural integrity under this hydrogen burning condition per RG 1.7. To demonstrate pressure integrity, a deterministic analysis is performed using material properties that are based on specified design values, which represent lower bound values, and include degradation with temperature. The analysis considers nonlinear material response for the concrete and steel components. Table A-2 provides a summary of the elastic properties for steels, and Table A-3 provides a summary of the plastic properties of the steel materials. Table A-4 provides a summary of the concrete properties. Note that the tensile strength has been reduced to a small value to eliminate tensile stress in the concrete as representative of design assumptions. All thermal properties are assumed to be constant with temperature and are summarized in Table 4-6.

The analysis includes the internal pressure and gravity loads, but ignores the thermal strains leading to thermal induced stresses, in accordance with RG 1.7. The temperature distribution within the structure for evaluation of temperature dependent material properties is taken to be the transient thermal condition where the prestressed concrete containment vessel (PCCV) atmosphere is at 1000 °F corresponding to the hydrogen burn scenario as used for the hydrogen burning case in the pressure fragility study as discussed in Sections 4.6 and 5.2. The outside environment and interior rooms outside the containment correspond to winter conditions. The stress analysis model is first initialized to be stress free at a uniform ambient temperature of 70 °F, and the gravity and prestressing loads are applied on the model. Next, the pressure of 162.4 psig along with the accident temperature distributions are incrementally applied to the model using static equilibrium iterations for nonlinear effects. Note that the coefficient of thermal expansion for all materials is set to zero to ignore thermal stresses. The calculated liner strains are then evaluated relative to the Factored Load limits to demonstrate structural integrity.

The structural and thermal models used for the deterministic analysis are the same global models as described in Section 5.1, except that a modification for the rebar transition across the equipment hatch (EH) is included in the structural model. As depicted in Figures 5-6 and 5-7, #18 hoop bars are used across the upper and lower parts of the EH whereas #14 hoop bars used for the nominal section thickness. At the 0° azimuth (away from the buttress), this rebar transition is now modeled by using a rebar area as the average area of #18 and #14 bars in the vertical row of elements along the transition line. There are also extra layers of horizontal bars, #14 bars on outside surface and #11 bars on inside surface, that terminate at this rebar transition area as shown in Figure 5-8.

Table A-5 provides a summary of the pressure at first yield of the steel components for this deterministic analysis. First yield in the liner develops at the transition to the thickened concrete section at the EH. First yield in the rebar develops in a local hoop bar on the outside surface around the EH. The tendons have not reached yield at the final pressure of 162.4 psi.

Figure A-1 illustrates the deformed shape of the PCCV at 162.4 psig pressure with the displacements magnified by a factor of 50. The horizontal cut view shows the reverse hoop bending at the buttresses and also near the 0° azimuth (12 o'clock in figure). This area is where the heavier reinforcement (#18 horizontal bars) at the EH stops and #14 bars start for the hoop reinforcement on the nominal sections.

Figure A-2 provides contour plots for the maximum principal strains in the liner for the surface next to the concrete and for the inside surface away from the concrete. This figure illustrates the areas of elevated strains, and the contour limits have been set at 0.3% strain to help identify any areas that may exceed the limit. The areas of elevated strain are shown to be around discontinuities in the structure, along the geometric kink for the thickened concrete section, along the buttresses, or at the rebar transition area near the 0° azimuth. The red color shows strains between 0.26 and 0.3%, and the gray color identifies strains above 0.3%. The global liner strain away from discontinuities is well below 0.3%. Figure A-3 plots both the membrane and membrane + bending strain for the maximum principal strains for the peak values of strain from the regions shown. In each of the 3 areas where the maximum principal strain exceeds 0.3% at a pressure of 162.4 psi, the element with the maximum value is identified and then the history of the strain for increasing pressure is plotted for each of the 3 elements. All elements are well within the 1.0% limit for membrane + bending. The elements along the kink in the geometry at the concrete thickness change show a peak membrane strain of 0.43%, and the elements at the buttress show a peak membrane strain of 0.31%. It is noted that the nonlinear shape of these strain curves before the pressure at first yield as identified in Table A-5 is due to concrete cracking and the changing modulus of the liner as the internal temperature increases to 1000 °F as the thermal condition for the hydrogen burn scenario.

To further assess the integrity of the containment for this pressure and temperature condition, the performance of the concrete and reinforcement are evaluated. Figure A-4 provides contours for minimum principal stress in the concrete. This plot is representative of the maximum concrete compressive stress. Generally, for factored loads, the allowable concrete compressive stress in design is limited to 75% of the compressive strength for primary membrane plus bending per American Society of Mechanical Engineers (ASME) Subsection CC-3421.1. The peak compressive stress found in the model is 6349 psi or 91% of the design strength due to bending at the connection with the basemat. However, this model treats the basemat as essentially rigid, and some relief in this peak bending stress is expected for a flexible basemat. In addition, this elevated compressive stress is seen to be a localized stress in an area with a steep gradient, and thus averaging over the 2 integration points in the vertical direction near the outside surface of the element is performed. This provides a maximum expected compressive stress of 4521 psi, which is below the design limit of 5250 psi as 75% of the design compressive strength.

ASME Subsection 3422.1 also provides an allowable limit of 90% of yield for tensile rebar stress in design for factored load categories. However, this section also provides that this limit can be exceeded if it can be shown that attainment of a general yield state is precluded. Figures A-5 and A-6 provide figures illustrating the areas where rebar stresses exceed 90% of the design yield strength of 60 ksi. These figures indicate that all rebar stresses in areas of global deformation response are within the design allowable limit. Elevated rebar stresses develop in areas affected by local discontinuities, such as near the buttresses, around the penetrations, and at the rebar transition area from the thickened EH section. Only the area at the rebar transition location has peak rebar stresses above the design based yield, and because a nonlinear analysis is performed, it is demonstrated that a general yield state does

not develop.

In summary, the analysis performed demonstrates that the liner will remain a leak tight barrier for the internal pressure and temperature associated with an accident where hydrogen is generated due to interaction between fuel cladding and water coolant. All global liner strains remain below the allowable limits specified in ASME subsection CC-3720 as required in Draft Regulatory Guide DG-1203, with some elevated values at local discontinuities. These local strains at discontinuities are well below ductility limits for the liner, especially at the liner elevated temperature, and in reality, the temperature difference between the liner and concrete will induce compressive stress in the liner. The structural integrity of the PCCV boundary is maintained for this pressure, and a general yield state is precluded for the primary forces due to this load.

**Table A-1 Summary of Factored Load Limits from ASME Subsection CC-3720**

Load State	Allowable Liner Strain	
	Membrane	Membrane + Bending
Tension	0.3%	1.0%
Compression	0.5%	1.4%

**Table A-2 Summary of Steel Elastic Properties**

	150 °F	500 °F	1000 °F
SA 516 Carbon			
Modulus (xE6 psi)	29.0	26.4	17.4
Poisson's Ratio	0.289	0.295	0.304
Prestressing			
Modulus (xE6 psi)	28.4	26.4	24.4
Poisson's Ratio	--	--	--

**Table A-3 Summary of Steel Plastic Properties for Pressure Integrity**

	150 °F	500 °F	1000 °F
SA516 Grade 70			
Yield Stress (ksi)	42.8	38.5	30.6
Tensile Strength (ksi)	71.3	66.7	50.8
Elongation (%)	17.0	16.4	24.0
SA516 Grade 60			
Yield Stress (ksi)	36.06	32.39	25.79
Tensile Strength (ksi)	61.14	57.20	43.52
Elongation (%)	21.0	20.3	29.7
A615 Grade 60 Rebar			
Yield Stress (ksi)	63.5	45.7	29.0
Tensile Strength (ksi)	97.0	86.4	47.3
Elongation (%)	8.6	9.0	10.0
A416 Grade 1860 Tendons			
Yield Stress (ksi)	243	231.0	212.1
Tensile Strength (ksi)	270	260.8	244.5
Elongation (%)	3.50	3.60	3.74

**Table A-4 Summary of Concrete Properties for Level C Analysis**

	150 °F	500 °F	1000 °F
PCCV Concrete (7 ksi)			
Comp Strength (psi)	7000	5233	3298
Strain at Peak Comp (%)	0.20	0.36	0.68
Modulus (xE6 psi)	4.769	1.912	0.617
Tensile Strength (psi)	6.3	4.2	2.6
Fracture Strain (xE-6)	--	--	--
Poisson's Ratio	0.18	0.18	0.18
Basemat Concrete (4 ksi)			
Comp Strength (psi)	4000	2948	1858
Strain at Peak Comp (%)	0.20	0.36	0.68
Modulus (xE6 psi)	3.605	1.407	0.454
Tensile Strength (psi)	4.7	3.1	1.96
Fracture Strain (xE-6)	--	--	--
Poisson's Ratio	0.18	0.18	0.18

**Table A-5 Summary of Pressure at First Yield in Steel Components**

<b>Component</b>	<b>Pressure (psi)</b>	<b>Note</b>
Liner	117.2	First yield occurs at transition to EH thickened concrete section
Rebar	134.7	First yield occurs in local hoop bar on outside surface around equipment hatch
Tendons	--	No yielding at final pressure of 162.4 psi



**Figure A-1 Deformed Shape x50 of PCCV at 162.4 psig Pressure**



**Figure A-2 Contour of Maximum Principal Strain in Liner at 162.4 psig Pressure**



**Figure A-3 Maximum Liner Strains as Function of Pressure**



**Figure A-4 Contour of Minimum Principal Stress in Concrete at 162.4 psig Pressure**



**Figure A-5 Locations of Peak Rebar Stress, 0 to 180 degrees of Model**



**Figure A-6 Locations of Peak Rebar Stress, 180 to 360 degrees of Model**

## **APPENDIX B**

# **Containment Performance for Pressure Loads for Containment Penetration**

## TABLE OF CONTENTS

LIST OF FIGURES .....	96
LIST OF TABLES.....	99
B-1 SCOPE.....	100
B-2 APPLICABLE DOCUMENTS .....	101
B-2.1 Project Documents .....	101
B-2.2 Codes and Standards.....	101
B-2.3 Reference Documents.....	101
B-3 SUMMARY DESCRIPTION .....	103
B-4 ANALYSIS METHODS.....	105
B-4.1 Finite Element Modeling.....	105
B-4.2 Loading Conditions.....	106
B-4.3 Thermal Conditions .....	106
B-4.4 Material Properties .....	112
B-4.5 Failure Criteria.....	115
B-5 PCCV GLOBAL MODEL .....	117
B-5.1 Model Description.....	117
B-5.2 Thermal Analyses.....	128
B-5.3 Stress Analyses.....	133
B-6 EQUIPMENT HATCH.....	138
B-6.1 Model Description.....	138
B-6.2 Analyses for Normal Operating Conditions .....	144
B-6.3 Analyses for Long Term Accident Conditions.....	147
B-6.4 Analyses for Hydrogen Burning Conditions.....	151
B-6.5 Equipment Hatch Summary.....	154
B-7 PERSONNEL AIRLOCK .....	155
B-7.1 Model Description.....	155
B-7.2 Analyses for Normal Operating Conditions .....	160
B-7.3 Analyses for Long Term Accident Conditions.....	164
B-7.4 Analyses for Hydrogen Burn Conditions.....	169
B-7.5 Personnel Airlock Summary .....	174
B-8 MAIN STEAM AND FEEDWATER PIPING.....	175
B-8.1 Model Description.....	175
B-8.2 Analyses for Normal Operating Conditions .....	179
B-8.3 Analyses for Long Term Accident Conditions.....	182
B-8.4 Analyses for Hydrogen Burn Conditions.....	185
B-8.5 MS/FW Piping Penetrations Summary .....	188
B-9 FUEL TRANSFER TUBE .....	189
B-9.1 Model Description.....	189
B-9.2 Analyses for Normal Operating Conditions .....	192
B-9.3 Analyses for Long Term Accident Conditions.....	195

B-9.4 Analyses for Hydrogen Burn Conditions..... 199  
B-9.5 Fuel Transfer Tube Summary..... 202

**LIST OF FIGURES**

Figure B-4-1	Thermal Conditions on Exterior Surfaces of PCCV .....	110
Figure B-4-2	Temperature and Pressure for Long Term Accident Condition .....	111
Figure B-4-3	Temperature and Pressure for Hydrogen Burning Condition .....	111
Figure B-5-1	Full 3-D Finite Element Modeling for Thermal Analysis.....	119
Figure B-5-2	Full 3-D Finite Element Modeling for Stress Analysis.....	120
Figure B-5-3	Illustration of Plate Element Modeling for Liner and Sleeves .....	121
Figure B-5-4	Illustration of Modeling for Tendons .....	122
Figure B-5-5	Modeling of Reinforcement, Inside Axial Bars.....	123
Figure B-5-6	Modeling of Reinforcement, Outside Axial Bars .....	124
Figure B-5-7	Modeling of Reinforcement, Inside Hoop Bars .....	125
Figure B-5-8	Modeling of Reinforcement, Outside Hoop Bars .....	126
Figure B-5-9	Modeling of Reinforcement, Other Bars .....	127
Figure B-5-10	Temperature Distribution for Normal Operating Condition .....	129
Figure B-5-11	Temperature Distribution for Long Term Accident Condition .....	130
Figure B-5-12	Concrete Temperature Distribution for Hydrogen Burning Condition .....	131
Figure B-5-13	Liner Temperature for Hydrogen Burning Condition.....	132
Figure B-5-14	Illustration of PCCV Global Deformation for Long Term Accident Conditions, Slice through Equipment Hatch, Pressure at 201.6 psig .....	134
Figure B-5-15	Illustration of PCCV Global Deformation for Long Term Accident Conditions, Slice through Main Steam Piping, Pressure at 201.6 psig .....	135
Figure B-5-16	Illustration of PCCV Global Deformation for Long Term Accident Conditions, Slice through Personnel Airlock, Pressure at 201.6 psig.....	136
Figure B-5-17	Illustration of PCCV Global Deformation for Long Term Accident Conditions, Slice through Fuel Transfer Tube, Pressure at 201.6 psig.....	137
Figure B-6-1	Local Model of Equipment Hatch, View from Inside .....	139
Figure B-6-2	Illustration of Steel Components for EH Model, View from Outside .....	140
Figure B-6-3	Local Model of Equipment Hatch, Cut Section View .....	141
Figure B-6-4	Local Model of Equipment Hatch, Close-up of Bolted Flange .....	142
Figure B-6-5	Local Model of Equipment Hatch, Studs and Tendons .....	143
Figure B-6-6	Temperature Distribution in EH, Normal Operating Condition.....	145
Figure B-6-7	Plastic Strain in Steel Components of EH, Normal Operating Condition, 235.0 psig Pressure, Section View.....	146
Figure B-6-8	Temperature Distribution in EH, LTA Conditions.....	148
Figure B-6-9	Plastic Strain in Steel Components of EH, LTA Conditions, 201.6 psig Pressure.....	149

Figure B-6-10	Illustration of Flange Contact Pressure for EH, LTA Conditions, 221.6 psig Pressure.....	150
Figure B-6-11	Temperature Distribution in EH, Hydrogen Burn Conditions .....	152
Figure B-6-12	Plastic Strain in Steel Components of EH, Hydrogen Burn Conditions, 231.7 psig Pressure.....	153
Figure B-7-1	Local Model of Personnel Airlock, Inside View.....	156
Figure B-7-2	Local Model of Personnel Airlock, Horizontal Section Cut View.....	157
Figure B-7-3	Local Model of Personnel Airlock, Close-up Views of Steel Components.....	158
Figure B-7-4	Local Model of Personnel Airlock, Studs and Tendons .....	159
Figure B-7-5	Temperature Distribution in AL, Normal Operating Condition .....	161
Figure B-7-6	Plastic Strain in Steel Components of AL, Normal Operating Condition, Exterior View, 240 psig Pressure .....	162
Figure B-7-7	Plastic Strain in Steel Components of AL, Normal Operating Condition, Interior View, 240 psig Pressure.....	163
Figure B-7-8	Temperature Distribution in AL, LTA Condition .....	165
Figure B-7-9	Plastic Strain in Steel Components of AL, LTA Condition, External View, 225.6 psig Pressure.....	166
Figure B-7-10	Plastic Strain in Steel Components of AL, LTA Condition, Internal View, 225.6 psig Pressure.....	167
Figure B-7-11	Contact Pressure in Flanges for AL, LTA Condition, 249.6 psig Pressure.....	168
Figure B-7-12	Temperature Distribution in AL, Hydrogen Burn Condition .....	170
Figure B-7-13	Plastic Strain in Steel Components of AL, Hydrogen Burn Condition, External View, 251.7 psig Pressure.....	171
Figure B-7-14	Plastic Strain in Steel Components of AL, Hydrogen Burn Condition, Internal View, 251.7 psig Pressure.....	172
Figure B-7-15	Contact Pressure in Flanges for AL, Hydrogen Burn Condition, 251.7 psig Pressure.....	173
Figure B-8-1	Illustration of MS/FW Local Model, View from Inside .....	176
Figure B-8-2	Illustration of MS/FW Local Model, Cut Section View .....	176
Figure B-8-3	Illustration of Modeling for Steel Components in MS/FW Local Model.....	177
Figure B-8-4	Illustration of modeling for liner and anchorages in MS/FW Local Model.....	177
Figure B-8-5	Illustration of modeling for Tendons in MS/FW Local Model .....	178
Figure B-8-6	Temperature Distribution in MS/FW, Normal Operating Condition.....	180
Figure B-8-7	Plastic Strain in Steel Components of MS/FW, Normal Operating Condition, 240 psig Pressure .....	180
Figure B-8-8	Concrete Shear Strain at MS/FW, Normal Operating Condition, 236 psig Pressure .....	181
Figure B-8-9	Temperature Distribution in MS/FW, LTA Condition .....	183

Figure B-8-10	Plastic Strain in Steel Components of MS/FW, LTA Condition, 249.6 psig Pressure .....	183
Figure B-8-11	Concrete Shear Strain at MS/FW, LTA Condition, 217.6 psig Pressure .....	184
Figure B-8-12	Temperature Distribution in MS/FW, Hydrogen Burn Condition .....	186
Figure B-8-13	Plastic Strain in Steel Components of MS/FW, Hydrogen Burn Condition, 251.7 psig Pressure.....	186
Figure B-8-14	Concrete Shear Strains at MS/FW, Hydrogen Burn Condition, 229.7 psig Pressure.....	187
Figure B-9-1	Illustration of FTT Local Model, View from Inside.....	190
Figure B-9-2	Illustration of FTT Local Model, View from Outside .....	190
Figure B-9-3	Illustration of FTT Local Model, Cut Section View .....	191
Figure B-9-4	Illustration of FTT Local Model, View of Steel Components.....	191
Figure B-9-5	Temperature Distribution in FTT, Normal Operating Condition .....	193
Figure B-9-6	Plastic Strain in Steel Components of FTT, Normal Operating Condition, 241 psig Pressure.....	194
Figure B-9-7	Concrete Shear Strain at FFT Penetration, Normal Operating Condition, 241 psig Pressure.....	194
Figure B-9-8	Temperature Distribution in FTT, LTA Condition.....	196
Figure B-9-9	Plastic Strain in Steel Components of FTT, LTA Condition, 249.6 psig Pressure.....	197
Figure B-9-10	Concrete Shear Strain at FFT Penetration, LTA Condition, 239.6 psig Pressure.....	197
Figure B-9-11	FFT Flange Cover Contact Pressure, LTA Condition, 249.6 psig Pressure ....	198
Figure B-9-12	Temperature Distribution in FTT, Hydrogen Burn Condition .....	200
Figure B-9-13	Plastic Strain in Steel Components of FTT, Hydrogen Burn Condition, 244.9 psig Pressure.....	200
Figure B-9-14	Concrete Shear Strain around FTT, Hydrogen Burn Condition, 244.9 psig Pressure.....	201

**LIST OF TABLES**

Table B-3-1	Summary of Pressure Capacities for US-APWR Containment Penetrations .....	104
Table B-4-1	Summary of Temperature Conditions.....	108
Table B-4-2	Temperature and Pressure in PCCV for Long Term Accident Thermal Condition .....	108
Table B-4-3	Temperature and Pressure in PCCV for Hydrogen Burning Thermal Condition .....	108
Table B-4-4	Film Coefficients for Thermal Conditions.....	109
Table B-4-5	Summary of Thermal Material Properties.....	112
Table B-4-6	Summary of Steel Elastic Properties .....	113
Table B-4-7	Summary of Steel Plastic Properties .....	114
Table B-4-7	Summary of Steel Plastic Properties (continued).....	115
Table B-4-8	Summary of Concrete Properties .....	115
Table B-4-9	Summary of Material Limits and Failure Criteria .....	116
Table B-6-1	Summary of Pressure Capacities for Equipment Hatch .....	154
Table B-7-1	Summary of Pressure Capacities for Personnel Airlock.....	174
Table B-8-1	Summary of Pressure Capacities for Main Steam and Feedwater Piping.....	188
Table B-9-1	Summary of Pressure Capacities for Fuel Transfer Tube .....	202

## B-1 SCOPE

The analyses described herein are provided to establish the relative pressure capacities of the containment penetrations for the US-APWR primary containment system. Previous work documented in Reference B-2.1.1 determined the pressure capacity of the Prestressed Concrete Containment Vessel (PCCV) and the large operable penetration for the equipment hatch (EH) using probabilistic based methods. Here, the relative ranking for pressure capacity is determined for all significant penetrations into containment, namely EH, personnel airlock (AL), main steam (MS) and feedwater (FW) piping, and the fuel transfer tube (FTT). Since the previous analyses were performed, some changes in the configurations of the PCCV and EH have occurred and the designs of the other components have progressed, and this current work considers the latest configurations of all components. The intent of this current work is to rank the pressure capacities for these penetration components using a common analytical basis. Thus, for this work, the pressure capacities are calculated using deterministic analyses and design minimum properties. The modeling methods employed are consistent with the previous work, using detailed local three dimensional (3-D) modeling for each of the penetration types and extracting boundary conditions for the local models from a 3-D global model of the PCCV. The failure criteria used in determining the pressure where leakage in the containment boundary will develop is based on plastic strain limits consistent with the previous work.

The global model from the previous work is updated to include the configuration changes and to incorporate the other penetrations to capture the response of the PCCV wall around the area of each penetration from the global response of the PCCV. The local model of the EH from the previous work is also updated for the current configurations, and new detailed 3-D finite element models are constructed for the personnel AL, the FTT, and the grouping of the 4 MS lines and 4 FW lines.

The pressure capacities are calculated for 3 specified thermal conditions, namely, steady state normal operating temperatures, steady state conditions representing long term accident (LTA) conditions, and transient thermal conditions for a hydrogen burning condition as representative of a severe accident involving much higher temperatures but for much shorter durations. Each model thus has 3 different analyses performed to determine the pressure capacities of each component to the 3 different thermal conditions.

## **B-2 APPLICABLE DOCUMENTS**

### **B-2.1 Project Documents**

- B-2.1.1 US-APWR Containment Performance for Pressure Loads, Technical Report MUAP-10018, Revision 0, June 2010.
- B-2.1.2 Design Control Document for US-APWR, Chapter 3, Design of Structures, Systems, Components and Equipment, MUAP DC003, Revision 3, March 2011.
- B-2.1.3 Design Report for the Basic Design of the US-APWR PCCV, PCV-13-05-113-001 Rev. 1, URS Corporation, July 2013.
- B-2.1.4 US-APWR Standard Design, Detail Configuration of Equipment Hatch (Drawing Package), KDS-UAP-20130003, Rev 0.
- B-2.1.5 US-APWR Standard Design Equipment Hatch Design Report N0-FH00208 Rev.4, November 2010.
- B-2.1.6 US-APWR Basic Design, URS Drawings PCV-13-11-004, Rev 2, July 2012.
- B-2.1.7 US-APWR Standard Design, Detail Configuration of Personnel Airlocks (Drawing Package), KDS-UAP-20130002, Rev 0.
- B-2.1.8 US-APWR Standard Design, Detailed Drawings for Containment Penetrations, N0-EF20007, Rev 3.
- B-2.1.9 Pressure and Thermal Conditions for Draft Technical Report of PCCV Ultimate Pressure Capacity, MHI Drawing 4DS-UAP-20100038, Revision 1, 2013.

### **B-2.2 Codes and Standards**

- B-2.2.1 ASME 2001 through 2003 addenda: Boiler and Pressure Vessel Code, Section III – Rules for Construction of Nuclear Power Plant Components, Division 2 – Code for Concrete Reactor Vessels and Containments, Subsection CC-Concrete Containments, Article CC 3000 – Design.
- B-2.2.2 ASME 2001 through 2003 addenda: Boiler and Pressure Vessel Code, Section II, Part A – Ferrous Material Specifications.
- B-2.2.3 ACI-349-06, Code Requirements for Nuclear Safety Related Concrete Structures.
- B-2.2.4 ASME 2001 through 2003 addenda: Boiler and Pressure Vessel Code, Section III – Rules for Construction of Nuclear Power Plant Components, Division 1 – Subsection NE – Class MC Components.

### **B-2.3 Reference Documents**

- B-2.3.1 ABAQUS/Standard, Version 6.12, Dassault Systemes Simulia Corp., Providence, RI.
- B-2.3.2 ANACAP-U, Version 2.5, Theory Manual, ANA-QA-145, ANATECH Corp., San Diego, CA, 1998.

- B-2.3.3 Regulatory Guide 1.216 Containment Structural Integrity Evaluation For Internal Pressure Loadings Above Design Basis Pressure, U. S. Nuclear Regulatory Commission, August 2010.
- B-2.3.4 Nonlinear, Incremental Structural Analysis of Massive Concrete Structures, ETL 1110-2-365, U. S. Army Corps of Engineers, Department of the Army, Washington, DC, August 1994.

### B-3 SUMMARY DESCRIPTION

Table B-3-1 provides a summary of the calculated pressure capacities for each type of penetration for the various thermal conditions based on a breach in the pressure boundary of that penetration.

For the EH, yielding and tearing in the cover at the connection to the flange is the limiting mechanism for both normal operating and LTA. For the hydrogen burn case, the limiting condition is found to be tearing in the sleeve at the connection with the PCCV.

At the personnel AL, plastic deformation and tearing in the sleeve is the limiting mechanism for pressure capacity for both normal operating and LTA. For the hydrogen burn condition, the limiting component is the front plate of the AL at the connection with the horizontal stiffeners.

The pressure limiting mechanism for MS/FW penetrations is excessive concrete shear strains leading to loss of the anchorage culminated by tendon failure. The MS/FW penetrations have relatively stiff steel components for the penetration diameter, and in addition, there is some interaction between the individual penetrations in the grouping.

For the FTT, the pressure capacity is limited by excessive concrete shear strains leading to loss of anchorage also culminated by tendon failure. This is attributed to the relatively stiff and thick steel sections coupled to a relatively small diameter penetration.

As used for the PRA, the ultimate capacity of the PCCV was calculated to be 201 psig in design control document (DCD) Chapter 19. The primary purpose of this technical report is to show that the 201 psig capacity is the smaller and more conservative value than the results summarized here from the non-linear analyses. For the Hydrogen burning Condition the limiting penetration is at the MS/FW with a capacity of 229.7 psig but this should not be a problem as it exceeds the ultimate PCCV capacity of 201 psig. On the other hand, the pressure capacity of the EH of 186.8 psig under LTA condition is lower than 201 psig. However, the results of probabilistic analysis which are described in main body of MUAP-10018 Rev.1 show the median pressure capacities of EH are higher than 201 psig under all thermal conditions.

**Table B-3-1 Summary of Pressure Capacities for US-APWR Containment Penetrations**

Component	Penetration Outer Sleeve Diameter	Failure Pressure (psig) Followed by Factor on P <sub>d</sub>		
		Normal Operating Conditions	Long Term Accident Conditions	Hydrogen Burning Conditions
Equipment Hatch	28'-7"	233.0 (3.43)	186.8 (2.75)	230.7 (3.39)
		cover	cover	sleeve
Personnel Airlock	8'-8 <sup>3</sup> / <sub>8</sub> "	242.0 (3.56)	223.6 (3.29)	>251.7 (3.70)
		sleeve	sleeve	front plate
MS/FW Piping	MS 5'-0"	236.0 (3.47)	217.6 (3.20)	229.7 (3.38)
	FW 2'-6"	anchorage	anchorage	anchorage
Fuel Transfer Tube	2'-6 <sup>1</sup> / <sub>2</sub> "	241 (3.54)	239.6 (3.52)	244.9 (3.60)
		anchorage	anchorage	anchorage

Note: > sign means that the analysis was carried to this pressure load and failure had not yet developed

## **B-4 ANALYSIS METHODS**

These analyses follow the modeling and analysis methods used in the previous work as described in Reference B-2.1.1. The geometry and configurations used in the analyses are based on References B-2.1.2 through B-2.1.8. These analyses are based on detailed 3-D finite element modeling and advanced material constitutive relations. To determine relative pressure capacities between different containment penetrations, deterministic analyses are performed using material properties that are based on specified design values, which represent lower bound values, and include degradation with temperature. The analysis considers nonlinear material response for the concrete and steel components and the effects of thermal induced stress. The failure criteria used to determine the limiting capacity is plastic strain in the component consistent with the previous work. The plastic strain represents a ductility limit for the material and is factored to account for weld seams, mesh fidelity, and biaxial loading. Here the 95% confidence value of the plastic strain limit as function of temperature is used to establish the pressure capacity. The pressure capacity is determined whenever the accumulated plastic strain anywhere in the component reaches the specified value. If the component is in pure membrane, this would be representative of net section failure. However, if the component has bending response, then the capacity is set whenever the outer fiber reaches the strain failure limit without considering that part of the section is still below the limit. It is also noted that the accumulated plastic strain also includes plastic deformation under compressive load, such as a component under elevated temperature that is restricted from free expansion.

These analyses are conducted for three different thermal conditions, 1) normal operating steady state conditions, 2) a LTA condition, and 3) a hydrogen burn representative of a severe accident condition. For the LTA condition, the temperature distribution is based on a steady state condition where the PCCV atmosphere has reached 438 °F over 120 hours representative of a bounding loss of coolant accident (LOCA) event. For the severe accident condition, the temperature distribution for the pressure capacity is based on a transient thermal condition using a snapshot of the temperatures when the PCCV liner reaches 1000 °F in a few seconds due to a hydrogen burn scenario. These thermal conditions are described in more detail in Section 4.3 below.

### **B-4.1 Finite Element Modeling**

The pressure capacities of the penetration components are calculated using local detailed 3-D finite element modeling. The following failure modes are considered in the detailed local models,

- Yielding and rupture of reinforcing bars around the penetration
- Yielding and rupture of tendons around the penetration
- Failure of concrete around the penetration, including shear failure along the sleeve
- Tearing of penetration steel components
- Flange separation for leakage through the gasket seal

Each local model has an extent of the PCCV included around the penetration of interest. The boundary conditions for these local models are taken from a global 3-D model of the complete PCCV. Thus, the effect of the global response of the PCCV under each thermal condition is accounted for in the pressure capacity of the individual penetration. Because of the EH and other penetrations with thickened concrete sections, the containment structure does not have a true plane of symmetry. The thermal conditions leading to over-pressurization are also not

symmetric around the containment due to partial coverage of the PCCV by the reactor building. The PCCV model is free standing and includes a portion of the basemat for anchoring the axial tendons. Continuum (solid) elements with embedded truss-like sub-elements for the reinforcement are used for the reinforced concrete sections. Truss elements with appropriate constraints to the concrete are used for the axial and hoop tendons. Plate elements are used for the steel liners and the penetration sleeves. In this global model, these liner elements are “glued” to the concrete surfaces without explicitly modeling the anchorage system.

Each analysis requires a thermal and a stress version of the model. The thermal model is used to determine the temperature distribution within the structure for each of the 3 thermal conditions, and the stress model is used to determine the pressure capacity based on the temperature distribution of interest and the combinations of the other parameter values. The temperature distributions are assumed to be independent of the stress solution, that is, the temperatures do not depend on displacements. The thermal analyses use bi-linear 8-node brick elements to avoid convergence issues associated with bi-quadratic elements and the implicit formulation used in the thermal solution. Steady state temperature solutions are used for the normal operating and LTA cases. A transient thermal solution is used for the hydrogen burning case with the initial conditions set to the steady state normal operating conditions. The appropriate temperature distribution is then transferred to the stress model, and the internal pressure is incrementally increased to find the failure pressure with that temperature distribution. The stress analyses use bi-quadratic (20-node) brick elements with reduced Gaussian quadrature integration. From past experience, these elements perform the best for concrete cracking analyses for a given level of mesh refinement or nodal degrees of freedom. Thus, the thermal analyses use models with 8 times as many elements, where each 20-node, quadratic element is divided into eight 8-node linear elements. The temperature distributions at the nodes for the specified time points are read into the stress analysis from the thermal models. The stress analysis is based on static equilibrium, ignoring inertia effects. At each of the load increments for increasing internal pressure, equilibrium iterations are used to redistribute the loads and section stresses as cracking develops. The stress analyses are then evaluated per the failure criteria described in Section 4.5 below to establish the failure pressure.

#### **B-4.2 Loading Conditions**

The analyses are performed by initializing the stress solution to be stress free at a uniform ambient temperature of 70 °F and then applying gravity loads and tendon prestressing. A thermal analysis (either steady state or transient, as appropriate) is performed to establish the temperature distributions within the structure for each particular thermal condition. The temperature distribution and pressures corresponding to that temperature condition are then incrementally applied to the stress model. Finally, the internal pressure is then slowly increased with static equilibrium iterations, holding the temperature distribution constant, to determine the pressure at which failure or leakage occurs for that thermal condition.

#### **B-4.3 Thermal Conditions**

As mentioned above, the pressure capacity is a function of temperature because internal pressure is associated with an accident condition involving elevated temperatures, and the capacity also depends on thermal stresses and material property degradation at elevated temperatures. The thermal conditions are intended as bounding cases for the type of accident under consideration.

The pressure capacity is thus calculated at 3 different thermal conditions, 1) normal operating steady state conditions, 2) steady state LTA conditions, and 3) severe accident transient conditions (hydrogen burning) where high temperatures develop for a relatively short duration. These thermal conditions are assumed to develop in extreme winter ambient conditions where larger thermal gradients through the structure would develop, as a conservative measure. The interior of the PCCV has uniform atmospheric temperature that acts over all interior surfaces. The exterior of the PCCV has some surface area exposed to ambient (open air) temperatures and some surface area exposed to room temperatures where the reactor building covers parts of the PCCV. These areas for the exterior surface of the PCCV are defined in Figure B-4-1. The actual boundaries in the model are approximate based on element sizing and spacing. The interior surfaces of the penetration collars through the PCCV wall will also be exposed to room temperatures because these are covered by the reactor building, and the closure lids for the penetrations are on the inside of the containment. The inside surface of the closure lid and flanges are exposed to the PCCV atmosphere temperature. Table B-4-1 provides a summary of the temperature conditions for the various surfaces for the 3 thermal conditions based on Reference B-2.1.2. The film coefficients to be used for heat convection on the various surfaces, as summarized in Table B-4-4, are based on data from Reference B-2.3.4.

The PCCV interior atmosphere temperature representing the long term design basis accident is based on the data provided in Reference B-2.1.9 described as loss of coolant in LOOP or Loss of component cooling water system (CCWS)/essential service water system (ESWS) and reactor coolant pump (RCP) seal LOCA. A simplified fit to this data is provided in Table B-4-2 and plotted in Figure B-4-2. For this thermal condition, the temperature distribution is based on a steady state solution with the PCCV atmosphere at 438 °F, which develops around 100 hours. The conditions for the severe accident are based on the conditions described in Reference B-2.1.9 for the case of hydrogen burn. Table B-4-3 provides the tabular data for this hydrogen burning condition with the corresponding plot in Figure B-4-3. The temperature distribution for this case is based on a transient thermal analysis and when the temperature reaches 1000 °F on the liner, the corresponding temperature distribution is used as the basis for the pressure capacity for this thermal condition, that is, the resulting temperature distribution is held constant while the pressure is incrementally increased to find the pressure capacity.

**Table B-4-1 Summary of Temperature Conditions**

<b>Condition</b>	<b>PCCV Interior Temperature (°F)</b>	<b>PCCV Open Air Temperature (°F)</b>	<b>PCCV Room Temperature (°F)</b>	<b>Ground<sup>a</sup> Temperature (°F)</b>
Normal Operating Steady State	105	-40	50	35
Long Term Accident Steady State	438	-40	50	35
Hydrogen Burning Transient	1000	-40	50	35

<sup>a</sup>The ground temperature is the temperature assumed at the bottom of the basemat.

**Table B-4-2 Temperature and Pressure in PCCV for Long Term Accident Thermal Condition**

<b>Time (Hours)</b>	<b>Temperature (°F)</b>	<b>Pressure (psig)</b>
0.0	105	0.0
1.3	168	6.0
6.0	223	18.0
11.0	270	44.0
21.5	323	90.0
27.0	337	86.0
36.0	367	95.2
54.0	393	116.4
99.0	438	178.4
111.0	438	190.8
126.0	438	201.6

**Table B-4-3 Temperature and Pressure in PCCV for Hydrogen Burning Thermal Condition**

<b>Time (Seconds)</b>	<b>Temperature (°F)</b>	<b>Pressure (psig)</b>
0.0	105	0.0
5.0	242	32.0
40.0	242	32.0
42.0	1530	159.0
162.0	242	32.0
300.0	242	32.0

**Table B-4-4 Film Coefficients for Thermal Conditions**

<b>Surface</b>	<b>Film Coefficient (BTU/hr-ft<sup>2</sup>-°F)</b>	<b>Comments</b>
Interior Steel Surfaces	infinite	Use large coefficient so that temperature of steel surface tracks PCCV atmosphere temperature
Exterior Concrete Surfaces	1.6	Concrete exposed to ambient elements and wind
Interior Concrete Surfaces	2.1	Concrete exposed to controlled room circulation inside Reactor Building

**Security-Related Information – Withheld Under 10 CFR 2.390**

**Figure B-4-1 Thermal Conditions on Exterior Surfaces of PCCV**



**Figure B-4-2 Temperature and Pressure for Long Term Accident Condition**



**Figure B-4-3 Temperature and Pressure for Hydrogen Burning Condition**

#### B-4.4 Material Properties

The thermal properties are based on commonly accepted values and summarized in Table B-4-5. The heat transfer or film coefficients used for heat convection from surfaces exposed to temperatures are summarized in Table B-4-4 in Section 4.3. These were provided in Reference B-2.3.4.

These analyses are based on design minimum values for mechanical material properties. The important point is that the analyses for each component are based on the same material properties to provide a common basis for establishing the relative pressure capacities. The mechanical properties as a function of temperature are based on that used in the previous work. A summary of the snapshot values for 3 discrete temperatures are provided in Table B-4-6 for the elastic properties and Table B-4-7 for the plastic properties for the steel materials. For the steel materials, continuous curves for the effective stress versus effective strain plasticity relations are developed for the design minimum values and for temperatures of 150, 250, 500, 800, and 1000 °F. In the analysis, linear interpolation between these values is used for intermediate temperatures, so these temperatures are chosen to provide a relatively good piecewise linear fit to the degradation shapes of the properties with temperature.

The concrete constitutive relations and modeling are the same as described in Reference B-2.1.1. A summary of the basic concrete properties are provided in Table B-4-8. Note that the tensile strength has been reduced to a small value to eliminate tensile stress in the concrete as representative of design assumptions.

**Table B-4-5 Summary of Thermal Material Properties**

Material	Weight Density (lb/ft <sup>3</sup> )	Specific Heat (BTU/lb-°F)	Conductivity (BTU/hr-ft-°F)	Coefficient of Expansion (/°F)
Concrete	150	0.21	0.8	5.5E-6
Carbon Steel Liner	490	0.12	26	6.5E-6
Structural Steel	490	0.12	26	6.5E-6
Reinforcement <sup>1</sup>	--	--	--	6.5E-6
Tendons <sup>1</sup>	--	--	--	6.5E-6

<sup>1</sup>Reinforcement and Tendons take on the temperatures of the surrounding concrete

**Table B-4-6 Summary of Steel Elastic Properties**

	150 °F	500 °F	1000 °F
SA 516 Carbon Steel			
Modulus (xE3 ksi)	29.0	26.4	17.4
Poisson's Ratio	0.289	0.295	0.304
Prestressing			
Modulus (xE3 ksi)	28.4	26.4	24.4
Poisson's Ratio	--	--	--
SA 106 Grade B			
Modulus (xE3 ksi)	29.2	27.3	20.4
Poisson's Ratio	0.289	0.295	0.304
SA 266 Grade 3			
Modulus (xE3 ksi)	29.0	27.1	20.2
Poisson's Ratio	0.289	0.295	0.304
SA 335 / SA 336 22			
Modulus (xE3 ksi)	30.3	28.3	24.7
Poisson's Ratio	0.289	0.295	0.304
A182 F304			
Modulus (xE3 ksi)	28.0	25.9	22.8
Poisson's Ratio	0.289	0.295	0.304
A312 T304			
Modulus (xE3 ksi)	28.0	25.9	22.8
Poisson's Ratio	0.289	0.295	0.304
A193 C1 B8			
Modulus (xE3 ksi)	28.0	25.9	22.8
Poisson's Ratio	0.289	0.295	0.304
A36			
Modulus (xE3 ksi)	29.0	27.0	22.9
Poisson's Ratio	0.289	0.295	0.304

**Table B-4-7 Summary of Steel Plastic Properties**

	150 °F	500 °F	1000 °F
<b>SA 516 Grade 70</b>			
Yield Stress (ksi)	38.0	34.1	26.9
Tensile Strength (ksi)	70.0	65.5	49.7
Elongation (%)	17.0	16.4	24.0
<b>SA 516 Grade 60</b>			
Yield Stress (ksi)	32.0	28.7	22.6
Tensile Strength (ksi)	60.0	56.2	42.6
Elongation (%)	21.0	20.3	29.7
<b>A615 Grade 60 Rebar</b>			
Yield Stress (ksi)	60.0	43.2	27.4
Tensile Strength (ksi)	90.0	80.0	43.9
Elongation (%)	7.0	9.0	10.0
<b>A416 Grade 1860</b>			
Yield Stress (ksi)	243.0	231.0	212.1
Tensile Strength (ksi)	270.0	260.8	244.5
Elongation (%)	3.50	3.60	3.74
<b>SA106 Grade B</b>			
Yield Stress (ksi)	32.9	28.5	20.8
Tensile Strength (ksi)	60.0	60.0	34.6
Elongation (%)	20.0	22.2	26.7
<b>266 Grade 3</b>			
Yield Stress (ksi)	35.2	30.6	22.3
Tensile Strength (ksi)	75.0	75.0	43.2
Elongation (%)	19.0	21.1	25.3
<b>SA 335 / SA 336 22</b>			
Yield Stress (ksi)	28.6	26.9	23.7
Tensile Strength (ksi)	60.0	58.2	53.9
Elongation (%)	22.0	24.4	29.3
<b>A182 F304</b>			
Yield Stress (ksi)	26.7	19.4	15.5
Tensile Strength (ksi)	75.0	63.4	57.4
Elongation (%)	30.0	33.3	40.0
<b>A312 T304</b>			
Yield Stress (ksi)	26.7	19.4	15.5
Tensile Strength (ksi)	75.0	63.4	57.4
Elongation (%)	35.0	38.9	46.7

**Table B-4-7 Summary of Steel Plastic Properties (continued)**

A193 C1 B8			
Yield Stress (ksi)	26.7	19.4	15.5
Tensile Strength (ksi)	75.0	63.4	57.4
Elongation (%)	30.0	33.3	40.0
A36			
Yield Stress (ksi)	41.6	31.0	18.9
Tensile Strength (ksi)	60.4	58.9	32.1
Elongation (%)	26.0	30.0	34.0

**Table B-4-8 Summary of Concrete Properties**

	150 °F	500 °F	1000 °F
PCCV Concrete (7 ksi)			
Comp Strength (psi)	7000	5233	3298
Strain at Peak Comp (%)	0.20	0.36	0.68
Modulus (xE6 psi)	4.769	1.912	0.617
Tensile Strength (psi)	6.3	4.2	2.6
Fracture Strain (xE-6)	--	--	--
Poisson's Ratio	0.17	0.17	0.17

**B-4.5 Failure Criteria**

The failure criteria used in these assessments follows that described in the previous work, Reference B-2.1.1. Here the 95% confidence value for plastic strain as a function of temperature is used for each material as summarized in Table B-4-9. The failure strain accounts for strain concentration factors relative to mesh fidelity, biaxial loading, and heat affected zones from welding, and temperature.

Failure criteria are also defined to consider leakage due to separation of the flanges for a bolted joint with gasket seals. The criteria used for this is to monitor the contact along the inner edge of the flanges, that is, the edge along the pressure boundary, and assume leakage occurs whenever contact is lost at any node along this edge. Thus, no credit is taken for the elasticity of the gasket in maintaining a seal if there is a separation at any point along the edges of the 2 mating flanges nearest the contained pressure.

**Table B-4-9 Summary of Material Limits and Failure Criteria**

Criteria	Normal Operating Conditions (150 °F)		Long Term Accident Conditions (500 °F)		Hydrogen Burning Conditions (1000 °F)	
	Median	95 %	Median	95 %	Median	95 %
Section Shear Strain (%)	0.55	0.44	0.55	0.44	0.55	0.44
Rebar Fracture Strain (%)	5.00	2.00	5.50	2.20	6.00	2.40
Tendon Failure Strain (%)	2.66	2.50	2.80	2.60	3.00	2.74
Steel Tearing Strain (%) (>1/4" thick, Grade 70)	1.72	1.40	1.75	1.17	2.87	1.96
Bolt Rupture Strain (%)	9.20	6.80	9.90	7.20	10.60	7.60

## B-5 PCCV GLOBAL MODEL

### B-5.1 Model Description

A global 3-D model is used to establish the global response of the PCCV under increasing pressure for each of the three thermal conditions of interest, namely normal operating, LTA and hydrogen burn as representative of severe accident. The results of the global modeling analyses are then used to couple the overall structural performance to the local models for each type of penetration by extracting the displacement response from the global model around the penetrations and applying these as displacement boundary conditions on the cut boundaries of the respective local model. The global modeling consists of a free-standing, full height representation of the PCCV. The thermal model, illustrated in Figure B-5-1, is used to determine the temperature distribution within the structure for each of the 3 thermal conditions, and the stress model, illustrated in Figure B-5-2, is used to determine the pressure capacity based on the temperature distribution of interest and the combinations of the other parameter values. The thermal model breaks each 3-D 20-node brick element used in the stress model into eight 8-node brick elements to avoid convergence issues in the thermal solution. Steady state temperature solutions are used for the normal operating and LTA cases. A transient thermal solution is used for the hydrogen burning case with the initial conditions set to the steady state normal operating conditions. The appropriate temperature distribution is then transferred to the stress model, and the internal pressure is incrementally increased to capture the global PCCV response under that temperature distribution.

Figure B-5-3 illustrates the 8-node plate element modeling used for the steel liner and penetration sleeves in the global stress model (a 4:1 refinement using 4-node shells is used for the thermal model). As illustrated in the figures, the concrete is modeled with solid elements and the steel liner is modeled with plate elements. The liner elements are attached to the common nodes on the surfaces of the concrete elements for compatibility with the concrete deformations. This assumes that the liner anchorage system keeps the liners in contact with the concrete for this global modeling of the PCCV performance. The prestressing tendons are modeled with truss elements using independent nodes from the concrete nodes. The tendon nodes are then constrained to the concrete nodes using constraint equations to capture the behavior of the greased tendons. For the hoop tendons, the tendons are constrained to the concrete in the radial and axial directions, but the tendon nodes are allowed to move relative to the concrete in the hoop direction. Similarly, for the axial tendons, the tendons are constrained to the concrete in the radial and hoop directions but are allowed to move relative to the concrete in the axial direction. For the areas with significant tendon curvature, for example the axial tendons in the dome and the tendons that wrap around the penetrations, the tendon nodes are fully constrained to the concrete. This tendon modeling is illustrated in Figure B-5-4. The prestress loads are applied using an initial stress in the tendon elements. The tendon elements are divided into groups to allow some variation in the initial stress distribution to simulate prestressing losses.

In the design basis of the PCCV, the effects of tendon relaxation, concrete creep, concrete shrinkage, and anchorage losses are considered in calculating a level of prestress after 60 years of operation based on American Society of Mechanical Engineers (ASME) code regulations, as described in Appendix A of Reference B-2.1.3. In the pressure capacity evaluation, this “end-of-life” prestressing level is considered the 95% confidence value of prestressing, that is, we are 95% confident that we will have at least this level of prestress over the life of the structure.

The reinforcement bars are modeled as embedded, truss-like steel elements at the appropriate locations within the concrete brick elements. The strains within the brick element at the locations of the rebar within that element are used to assess the rebar performance via the constitutive relations for the steel material. The associated stiffness and stress in the reinforcement are superimposed onto the concrete brick element. The reinforcement included in the modeling is schematically illustrated in Figures B-5-5 through B-5-9, showing axial bars on the inner surface, axial bars on the outer surface, hoop bars on the inner surface, hoop bars on the outer surface, and other secondary reinforcement, respectively. As illustrated, some smearing of the reinforcement is performed to reduce modeling and computation times, for example, every other bar may be explicitly included but each with twice the area (2:1 modeling). In some areas, 4 bars are lumped together as a single truss-like sub-element with 4 times the individual rebar area (4:1).

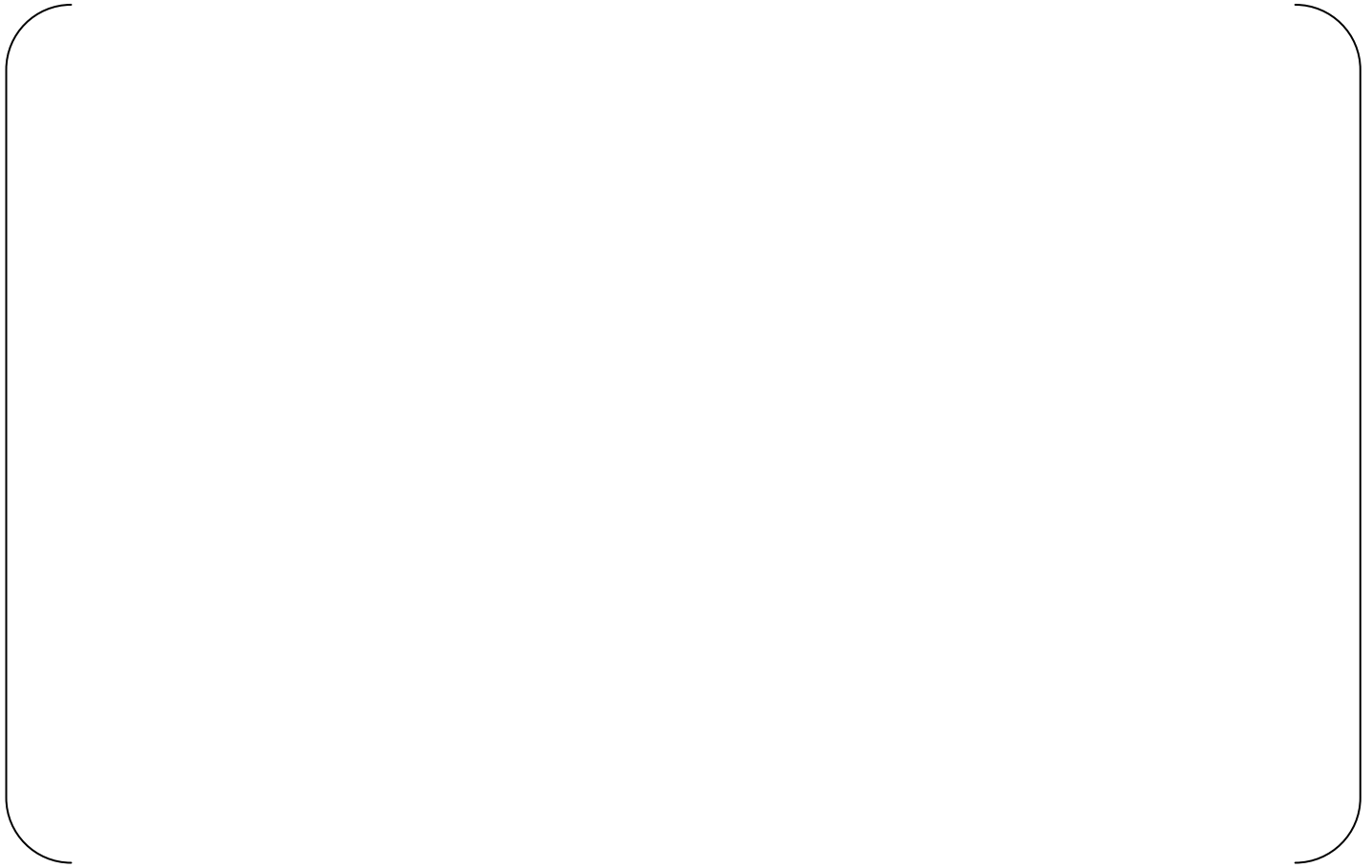


**Figure B-5-1 Full 3-D Finite Element Modeling for Thermal Analysis**



**Figure B-5-2 Full 3-D Finite Element Modeling for Stress Analysis**

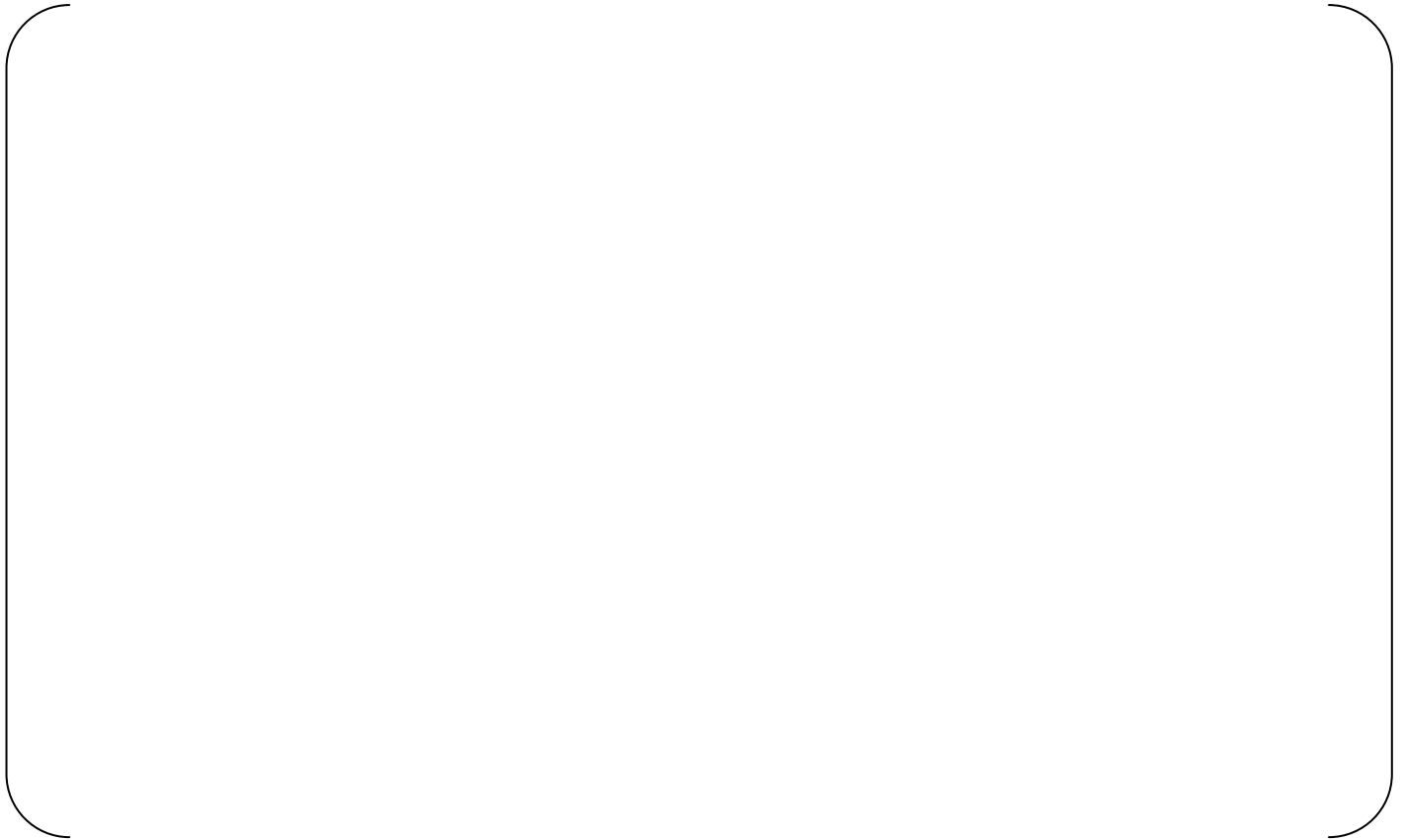


**Figure B-5-3 Illustration of Plate Element Modeling for Liner and Sleeves**



**Figure B-5-4 Illustration of Modeling for Tendons**



**Figure B-5-5 Modeling of Reinforcement, Inside Axial Bars**



**Figure B-5-6 Modeling of Reinforcement, Outside Axial Bars**



**Figure B-5-7 Modeling of Reinforcement, Inside Hoop Bars**

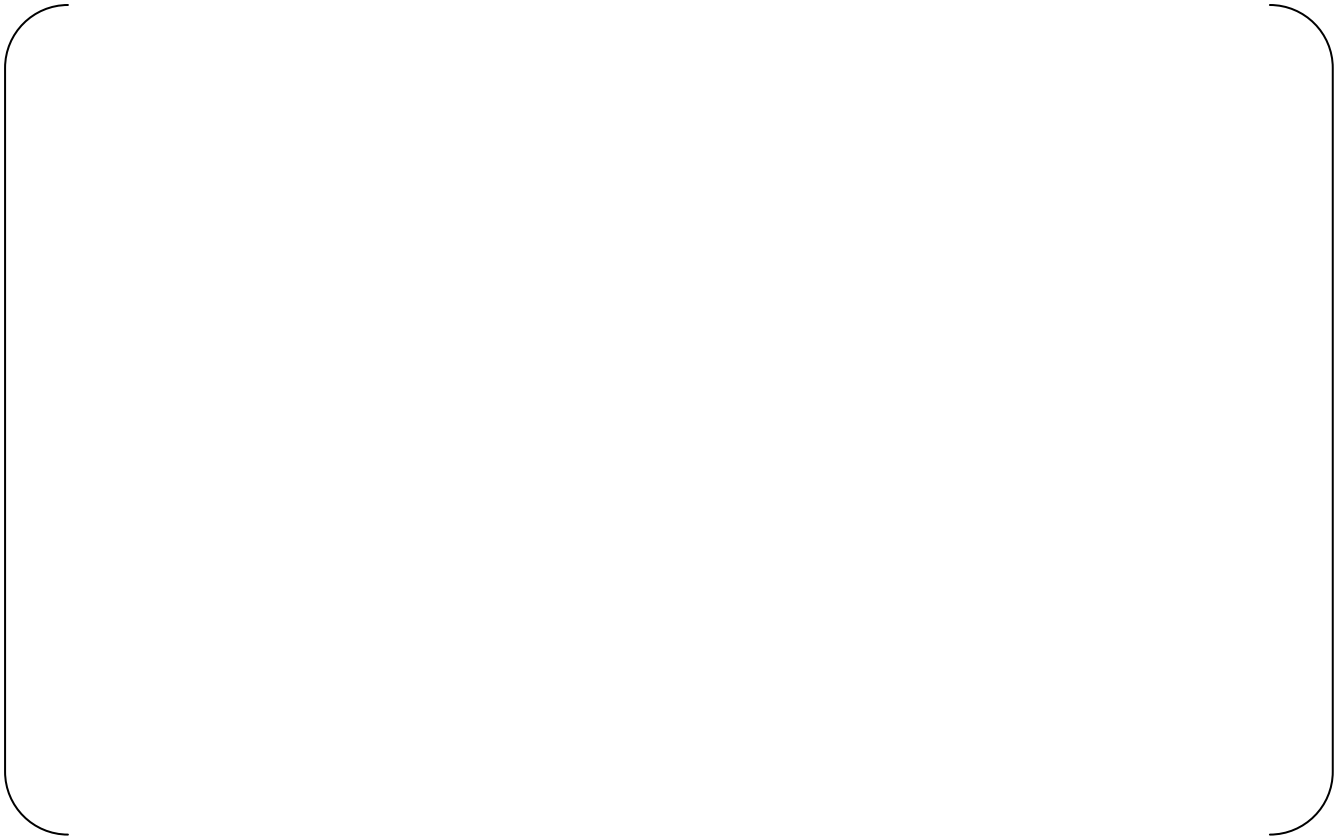


**Figure B-5-8 Modeling of Reinforcement, Outside Hoop Bars**

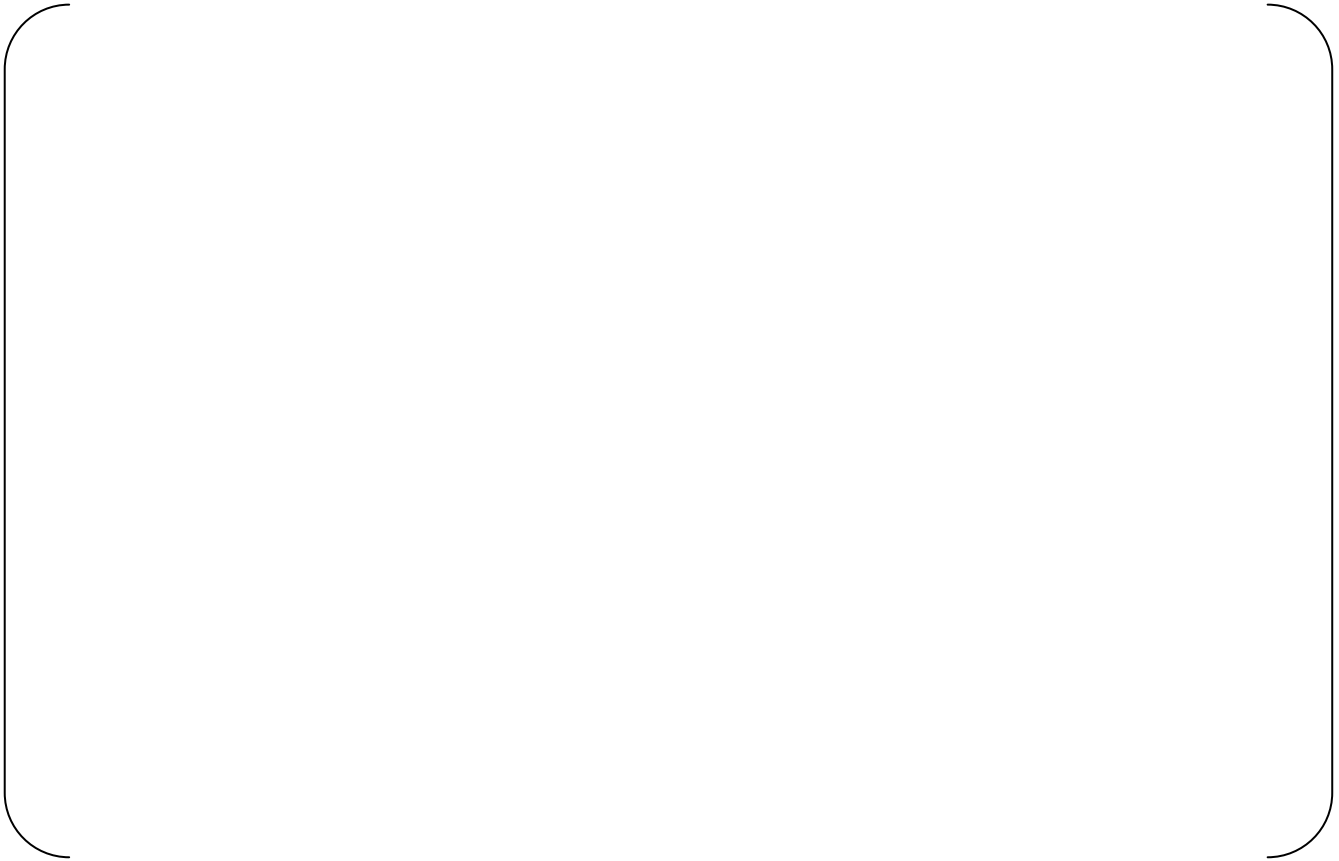


**Figure B-5-9 Modeling of Reinforcement, Other Bars**

## **B-5.2 Thermal Analyses**

The thermal model is used to develop the temperature distributions for the stress model in performing the pressure capacity analyses. The temperature distributions determine the variation of material properties with temperature within the structure and thermal stresses based on the changes from reference temperature and restraint against thermal expansion or contraction. The 3 thermal conditions described in Section 4.3 are used as the basis for evaluating the variation of pressure capacity with temperature. The temperature distributions associated with these 3 thermal conditions are illustrated in Figure B-5-10 for normal operating condition, Figure B-5-11 for long term design basis accident condition, and Figures B-5-12 and B-5-13 for the hydrogen burning thermal condition. The temperature distribution for the normal operating condition is based on a steady state solution with the PCCV atmosphere at 105 °F. The temperature distribution for the LTA thermal condition is based on a steady state solution with the PCCV atmosphere at 438 °F. The temperature distribution for the hydrogen burning thermal condition is based on a transient solution when the PCCV atmosphere and liner reach 1000 °F for a postulated hydrogen burn scenario. All 3 thermal conditions are considered to occur during extreme winter ambient conditions when the outside air temperature is -40 °F.



**Figure B-5-10 Temperature Distribution for Normal Operating Condition**



**Figure B-5-11 Temperature Distribution for Long Term Accident Condition**



**Figure B-5-12 Concrete Temperature Distribution for Hydrogen Burning Condition**



**Figure B-5-13 Liner Temperature for Hydrogen Burning Condition**

### B-5.3 Stress Analyses

The global PCCV structural response is calculated for each of the 3 thermal conditions described in Section 4.3 and illustrated in the previous section. The displacement histories for the set of nodes around each penetration are captured for transfer to the respective local model. The following figures illustrate the deformation of the PCCV under LTA conditions for a pressure of 201.6 psig ( $2.96 \cdot P_d$ ) with deformations magnified by 20. Figure B-5-14 illustrates the deformed shape for a slice through the EH, Figure B-5-15 illustrates the deformed shape for a slice through the MS piping, Figure B-5-16 illustrates the deformed shape for a slice through the personnel AL, and Figure B-5-17 illustrates the deformed shape for a slice through the FTT. These horizontal cut views show the reverse hoop bending at the buttresses and also near the  $0^\circ$  azimuth (12 o'clock in figure).

The deformation patterns and history under increasing pressures are also captured for the normal operating thermal condition and for the hydrogen burn accident thermal conditions for input into the local models for these conditions. The global response includes cracking (zero tensile strength), compressive yielding, and post cracking shear performance in the concrete and yielding and plastic deformation of steel components with material properties as a function of temperature.



**Figure B-5-14 Illustration of PCCV Global Deformation for Long Term Accident Conditions, Slice through Equipment Hatch, Pressure at 201.6 psig**



**Figure B-5-15 Illustration of PCCV Global Deformation for Long Term Accident Conditions, Slice through Main Steam Piping, Pressure at 201.6 psig**



**Figure B-5-16 Illustration of PCCV Global Deformation for Long Term Accident Conditions, Slice through Personnel Airlock, Pressure at 201.6 psig**



**Figure B-5-17 Illustration of PCCV Global Deformation for Long Term Accident Conditions, Slice through Fuel Transfer Tube, Pressure at 201.6 psig**

## **B-6 EQUIPMENT HATCH**

### **B-6.1 Model Description**

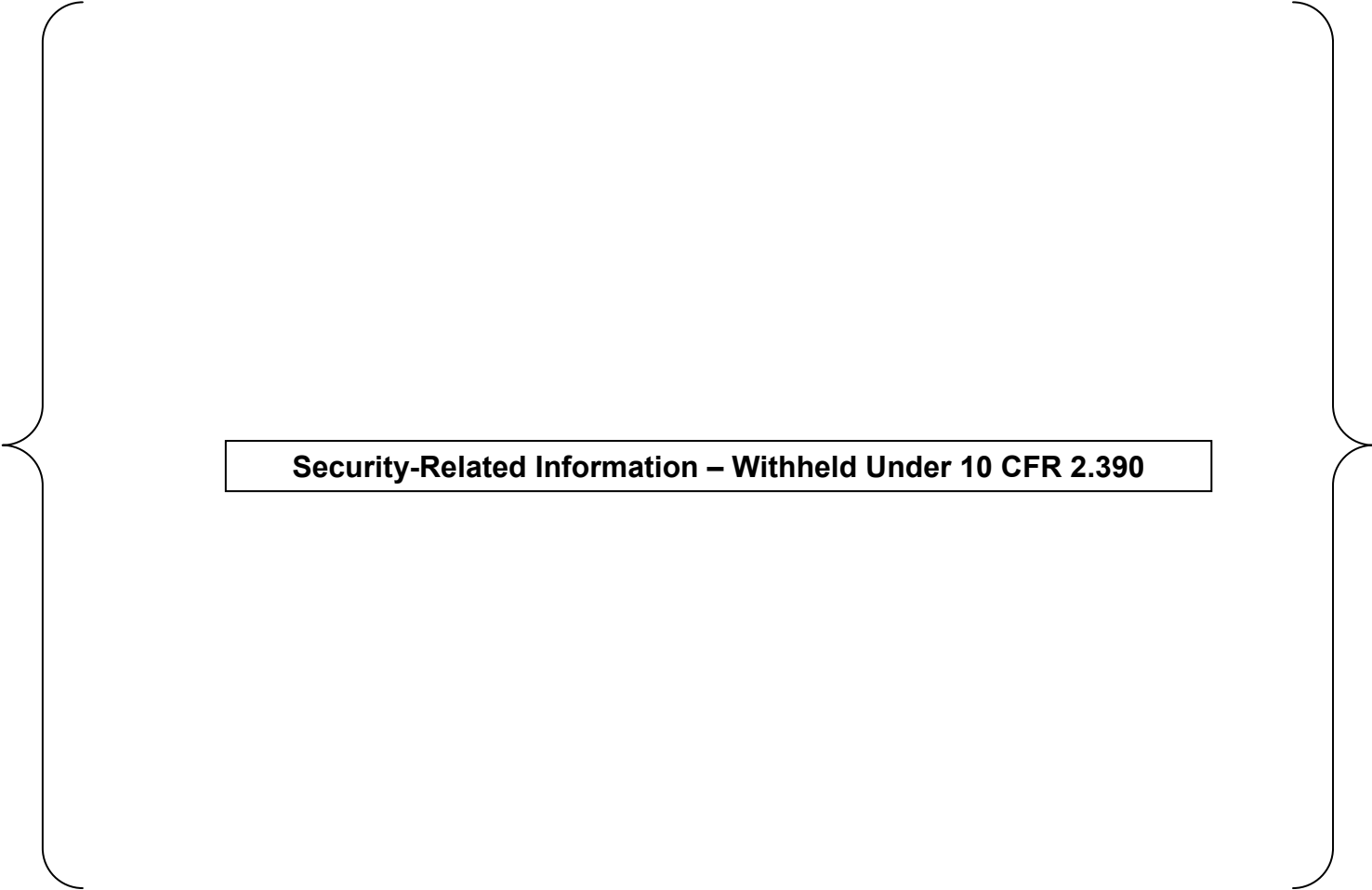
A local 3-D model of the EH and a portion of the PCCV wall around the EH is used to identify pressure capacities that are limited by the local performance of EH components using more detailed modeling of these components. For example, the global model includes the EH penetration but does not include the EH cover while the EH local model includes the cover, the closure bolts, and mating flanges as well as more refined meshing for the EH components. The local EH model uses boundary conditions extracted from the global model to impose the global deformation response on the local model.

The local modeling for the EH model, including a section of the PCCV wall around the penetration, is illustrated in the following figures. Figure B-6-1 shows an overall view looking from the inside of containment. Figure B-6-2 illustrates the liner and steel components viewed from outside containment. The liner is modeled with plate elements with common nodes to the concrete surface without explicitly including the anchorage components in the model. Figure B-6-3 provides a cut section view illustrating the thickened concrete section. Figure B-6-4 provides a close-up view of the modeling used for the bolted flange connection for the hatch cover. The EH closure is a pressure-seating design with the closure cover on the inside of containment. The closure bolts are modeled with beam elements with the appropriate length, cross-sectional area, connections, and initial prestress. A contact surface between the flanges is used to allow flange slippage or separation to develop as appropriate. A friction coefficient of 0.42 is used between these surfaces based on Reference B-2.1.5. This modeling includes the effects of flange rotation and relative movement between the flanges due to ovalization of the EH penetration. Flange separation along the inside edge of the sealing flanges is used as the metric in determining pressure capacity for seal leakage. Figure B-6-5 illustrates the shear studs on the outside of the sleeve and also the tendons included in the local model. The reinforcement in the local model is the same as discussed in Section 5-1 for the global model.

Displacement boundary conditions, extracted from the global model, are imposed on the cut sections of the PCCV wall in the local model. This enforces the deformation patterns from the global response of the containment system on the local model while capturing more refinement in the structural response of the EH components. A thermal analysis, using a more refined local thermal model consistent with that performed for the global model, is performed for the local model to establish the temperature distributions in the refined mesh of the local model. The thermal and pressure loads are incrementally applied in coordination with the displacement boundary conditions for the same loading states in the global model to evaluate the failure modes and failure pressure levels for the EH components.

**Security-Related Information – Withheld Under 10 CFR 2.390**

**Figure B-6-1 Local Model of Equipment Hatch, View from Inside**



**Security-Related Information – Withheld Under 10 CFR 2.390**

**Figure B-6-2 Illustration of Steel Components for EH Model, View from Outside**

**Security-Related Information – Withheld Under 10 CFR 2.390**

**Figure B-6-3 Local Model of Equipment Hatch, Cut Section View**

**Security-Related Information – Withheld Under 10 CFR 2.390**

**Figure B-6-4 Local Model of Equipment Hatch, Close-up of Bolted Flange**



**Figure B-6-5 Local Model of Equipment Hatch, Studs and Tendons**

## **B-6.2 Analyses for Normal Operating Conditions**

A local thermal model is used to develop the temperature distributions for the local stress model in performing the pressure capacity analyses. The local thermal model has double mesh refinement in all directions (each 20-node brick replaced with eight 8-node bricks) consistent with that described for the global modeling. The temperature distributions determine the variation of material properties with temperature within the structure and thermal stresses based on the changes from reference temperature and restraint against thermal expansion or contraction. The temperature distributions associated with normal operating condition for the local EH model are illustrated in Figure B-6-6. The temperature distribution for the normal operating condition is based on a steady state solution with the PCCV atmosphere at 105 °F and the exterior surfaces corresponding to extreme winter ambient conditions when the air temperature is -40 °F. Figure B-6-7 illustrates the distribution of plastic strain in the steel components of the EH for normal operating conditions at a pressure of 235 psig. This plot is a longitudinal section view and indicates that the limiting pressure condition for these steel components is in the cover at the connection with the flange.

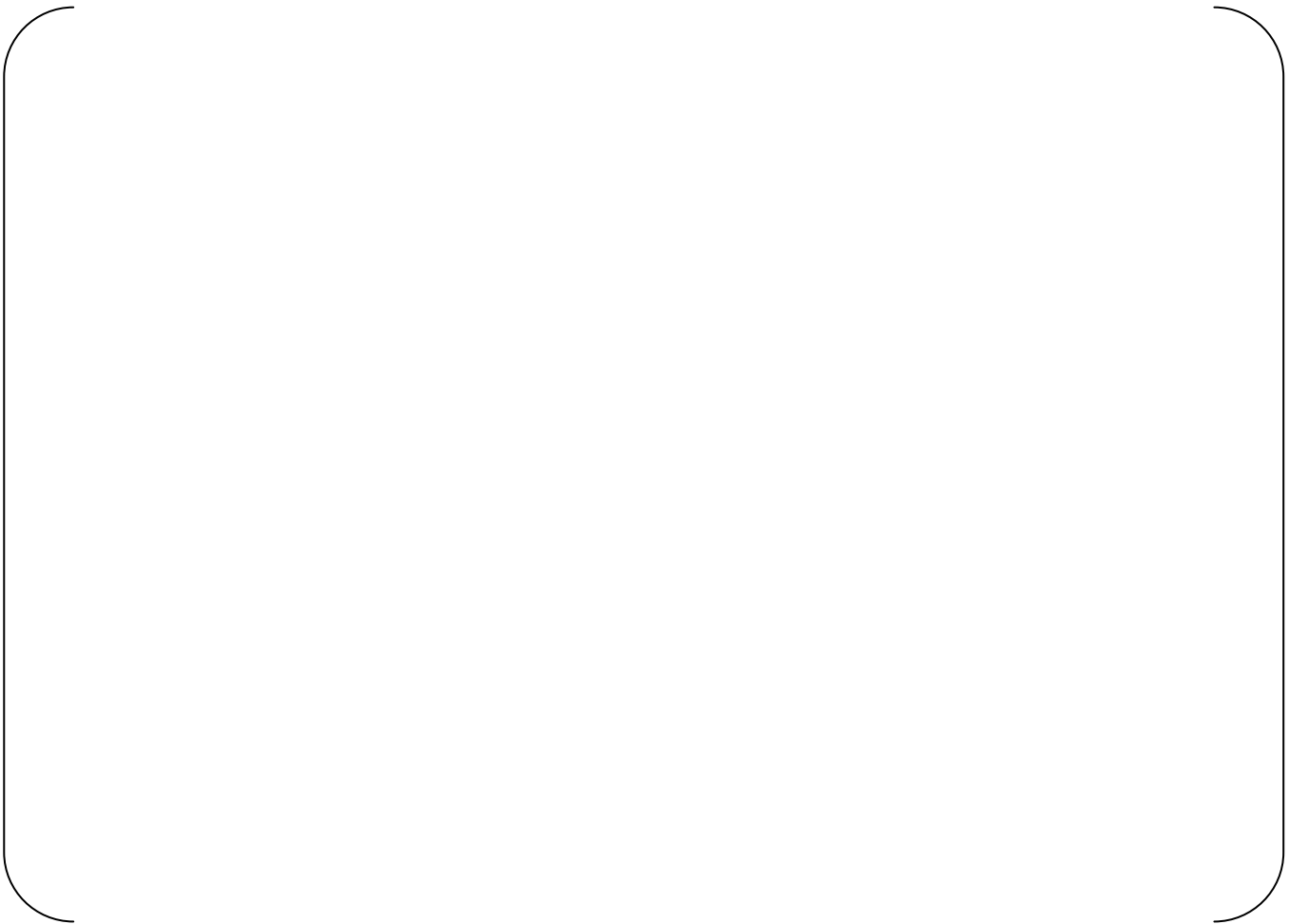


**Figure B-6-6 Temperature Distribution in EH, Normal Operating Condition**



**Figure B-6-7 Plastic Strain in Steel Components of EH, Normal Operating Condition, 235.0 psig Pressure, Section View**

### **B-6.3 Analyses for Long Term Accident Conditions**

The temperature distributions associated with LTA conditions for the local EH model are illustrated Figure B-6-8. The temperature distribution for the LTA thermal condition is based on a steady state solution with the PCCV atmosphere at 438 °F and the exterior surfaces corresponding to extreme winter ambient conditions when the air temperature is -40 °F. Figure B-6-9 illustrates the distribution of plastic strain in the steel components of the EH for the LTA conditions at a pressure of 201.6 psig. This plot is a longitudinal section view and indicates that the limiting pressure condition for these steel components is in the cover at the connection with the flange. Figure B-6-10 plots a contour of the contact pressure between the flanges in the EH for LTA thermal conditions at a pressure of 221.6 psig. Here the positive pressure values indicate that the flanges are still in contact. This figure shows that the inner surface still has good contact and thus no leakage through the bolted seal occurs.



**Figure B-6-8 Temperature Distribution in EH, LTA Conditions**



**Figure B-6-9 Plastic Strain in Steel Components of EH, LTA Conditions, 201.6 psig Pressure**



**Figure B-6-10 Illustration of Flange Contact Pressure for EH, LTA Conditions, 221.6 psig Pressure**

#### **B-6.4 Analyses for Hydrogen Burning Conditions**

The temperature distributions associated with hydrogen burning accident condition for the local EH model are illustrated in Figure B-6-11. Due to the orientation of the plate element surfaces, 2 figures are provided, one showing the temperatures for inside surface of liner and one showing the exposed surfaces of the EH and cover. The temperature distribution for the hydrogen burning thermal condition is based on a transient solution when the PCCV atmosphere and liner reach 1000 °F for a postulated hydrogen burn scenario with the exterior surfaces corresponding to extreme winter ambient conditions when the air temperature is -40 °F. Figure B-6-12 illustrates the distribution of plastic strain in the steel components of the EH for hydrogen burning thermal conditions at a pressure of 231.7 psig. This plot is a longitudinal section view and indicates that the limiting pressure condition for these steel components is in the sleeve at the connection with the PCCV wall. Again, the inner edge of the mating flanges remains in contact for the limiting pressure due to plastic deformation in the other steel components.



**Figure B-6-11 Temperature Distribution in EH, Hydrogen Burn Conditions**



**Figure B-6-12 Plastic Strain in Steel Components of EH, Hydrogen Burn Conditions, 231.7 psig Pressure**

### B-6.5 Equipment Hatch Summary

Table B-6-1 provides a summary of the calculated pressure capacities for the various failure modes considered for the three thermal conditions. The limiting condition for the normal operating and LTA conditions is yielding and excessive plastic strain at the connection of the cover with the flange. It is also noted that for normal operating conditions, plastic strain limits in the rebar at the transition from the strengthened section develops prior to failure in the cover. This plastic deformation in the rebar would not itself result in pressure leakage, but leads to the failure on the pressure boundary. For the hydrogen burn case, the limiting condition is found to be tearing in the sleeve at the connection with the PCCV. It is noted that for this case, the results are very sensitive to the duration of the high temperatures that determines how far the temperatures penetrate through the thickness of the steel elements. Here, the temperature snapshot is taken at 42 seconds, and the 1000 °F is only skin deep in the components. Even for a few minutes of “soak” time, the pressure capacity of the cover will decrease significantly as the high temperature conducts through the thickness of the shell. In all cases, the inner surface edge of the bolted flange connection remains in contact, and thus prevents leakage through the seals for these limiting pressures. The pressure capacity of the EH penetration is found to be greater than  $2.7 \cdot P_d$  for all cases.

**Table B-6-1 Summary of Pressure Capacities for Equipment Hatch**

Failure Mode	Failure Pressure (psig), Followed by Factor on $P_d$		
	Normal Operating Conditions	Long Term Accident Conditions	Hydrogen Burning Conditions
EH Sleeve Tearing	>235.0	>221.6	230.7
	>3.46	3.26	3.39
EH Cover	233.0	186.8	>231.7
	3.43	2.75	>3.41
EH Flange Leakage	>235.0	>221.6	>231.7
	>3.46	>3.26	>3.41
EH Rebar Rupture	228.0	212.6	230.7
	3.35	3.13	3.39

## **B-7 PERSONNEL AIRLOCK**

### **B-7.1 Model Description**

A local, detailed 3-D model of a personnel AL including a portion of the PCCV wall is used to calculate the pressure capacities that are limited by the local performance of the AL components. There are 2 AL locations into containment. The AL closer to the mid-height of the PCCV barrel section is judged to be more critical due to larger deformations in the wall of the PCCV at this location. This AL is also closer to a buttress, which induces some non-uniform bending in the hoop direction. The local AL model uses boundary conditions extracted from the global model to impose the global deformation response on the local model. The AL closure is a pressure-seating design with the door opening inward to containment.

The local modeling for the AL model, including a section of the PCCV wall around the penetration, is illustrated in the following figures. Figure B-7-1 provides an overall view of the local model for the AL. Figure B-7-2 provides a cut section view illustrating some of the details of the interior of the penetration and the slightly thickened concrete section. The door on the outside of containment is not included in the modeling. Figure B-7-3 provides close-up views of the modeling used for the steel components for the liner, the penetration sleeve, the inner door, the bulkhead walls, and the bulkhead stiffeners. The liner is modeled with plate elements with common nodes to the concrete surface without explicitly including the anchorage components in the model. The seal is provided by a force applied to the door to provide contact along the mating flanges between the door and the bulkhead plate with 2 O-ring seals. A contact surface between the flanges is used to allow flange slippage or separation to develop as appropriate. A friction coefficient of 0.42 is used between these surfaces based on Reference B-2.1.5. This modeling includes the effects of flange rotation and relative movement between the flanges due to the stiffness of the door and bulkhead wall. Separation of the inner surface of the flanges is used as the metric in determining pressure capacity for this failure mechanism. Figure B-7-4 illustrates the shear studs on the outside of the sleeve and also the tendons included in the local model. The reinforcement in the local model is the same as discussed in Section 5-1 for the global model. Displacement boundary conditions, extracted from the global model, are imposed on the cut sections of the PCCV wall in the local model. This enforces the deformation patterns from the global response of the containment system on the local model while capturing more refinement in the structural response of the AL components. A thermal analysis, using a more refined local thermal model consistent with that performed for the global model, is performed for the local model to establish the temperature distributions in the refined mesh of the local model. The thermal and pressure loads are incrementally applied in coordination with the displacement boundary conditions for the same loading states in the global model to evaluate the failure modes and failure pressure levels for the personnel AL components.

**Security-Related Information – Withheld Under 10 CFR 2.390**

**Figure B-7-1 Local Model of Personnel Airlock, Inside View**

**Security-Related Information – Withheld Under 10 CFR 2.390**

**Figure B-7-2 Local Model of Personnel Airlock, Horizontal Section Cut View**

**Security-Related Information – Withheld Under 10 CFR 2.390**

**Figure B-7-3 Local Model of Personnel Airlock, Close-up Views of Steel Components**



**Figure B-7-4 Local Model of Personnel Airlock, Studs and Tendons**

## **B-7.2 Analyses for Normal Operating Conditions**

Figure B-7-5 illustrates the temperature distribution for the normal operating condition showing a horizontal slice through the AL for the steel components. Figure B-7-6 and B-7-7 plot accumulated plastic strain for the AL steel components with an external and internal view, respectively, at a pressure of 240 psig. The external view plot indicates yielding in the sleeve both at the connections with the stiffeners and near the outer bulkhead, and the internal view indicates yielding in the stiffeners and in the sleeve at the connection with the stiffeners. Tearing of the sleeve near the outer bulkhead, caused by ovalization of the AL penetration, would not itself result in pressure leakage. The limiting condition will be tearing of the AL sleeve at the connection with the 6" deep vertical stiffeners.



**Figure B-7-5 Temperature Distribution in AL, Normal Operating Condition**



**Figure B-7-6 Plastic Strain in Steel Components of AL, Normal Operating Condition, Exterior View, 240 psig Pressure**



**Figure B-7-7 Plastic Strain in Steel Components of AL, Normal Operating Condition, Interior View, 240 psig Pressure**

### **B-7.3 Analyses for Long Term Accident Conditions**

Figure B-7-8 illustrates the temperature distribution for the LTA condition showing a horizontal slice through the AL. Figures B-7-9 and B-7-10 plot accumulated plastic strain for the AL steel components with an external and internal view, respectively, at a pressure of 225.6 psig. The external view plot indicates yielding in the bulkhead plate at the connections with the sleeve and the stiffeners, and the internal view indicates yielding in the stiffeners and in the sleeve at the connection with the stiffeners. The limiting condition will be tearing of the AL sleeve at the connection with the 6" deep vertical stiffeners. Figure B-7-11 provides a contour plot for the contact pressure around the mating flanges of the AL door showing that the inner surfaces remain in contact preventing leakage through the seal.



**Figure B-7-8 Temperature Distribution in AL, LTA Condition**



**Figure B-7-9 Plastic Strain in Steel Components of AL, LTA Condition, External View, 225.6 psig Pressure**



**Figure B-7-10 Plastic Strain in Steel Components of AL, LTA Condition, Internal View, 225.6 psig Pressure**



**Figure B-7-11 Contact Pressure in Flanges for AL, LTA Condition, 249.6 psig Pressure**

#### **B-7.4 Analyses for Hydrogen Burn Conditions**

Figure B-7-12 illustrates the temperature distribution for the hydrogen burn accident condition showing a horizontal slice through the AL. Figure B-7-13 and B-7-14 plot accumulated plastic strain for the AL steel components with an external and internal view, respectively, at a pressure of 251.7 psig. The external view plot indicates yielding in the bulkhead plate at the connections with the stiffeners and in the sleeve near the outer bulkhead, and the internal view indicates yielding in the stiffeners and in the sleeve at the connection with the stiffeners. Tearing of the sleeve near the outer bulkhead, caused by ovalization of the AL penetration, would not itself result in pressure leakage. The limiting condition will be tearing of the AL front plate at the connection with the horizontal stiffener. This condition is due to the high temperatures acting directly on the front face of the bulkhead plate. Figure B-7-15 provides a contour plot for the contact pressure around the mating flanges of the AL door showing that the inner surfaces remain in contact preventing leakage through the seal.



**Figure B-7-12 Temperature Distribution in AL, Hydrogen Burn Condition**



**Figure B-7-13 Plastic Strain in Steel Components of AL, Hydrogen Burn Condition, External View, 251.7 psig Pressure**

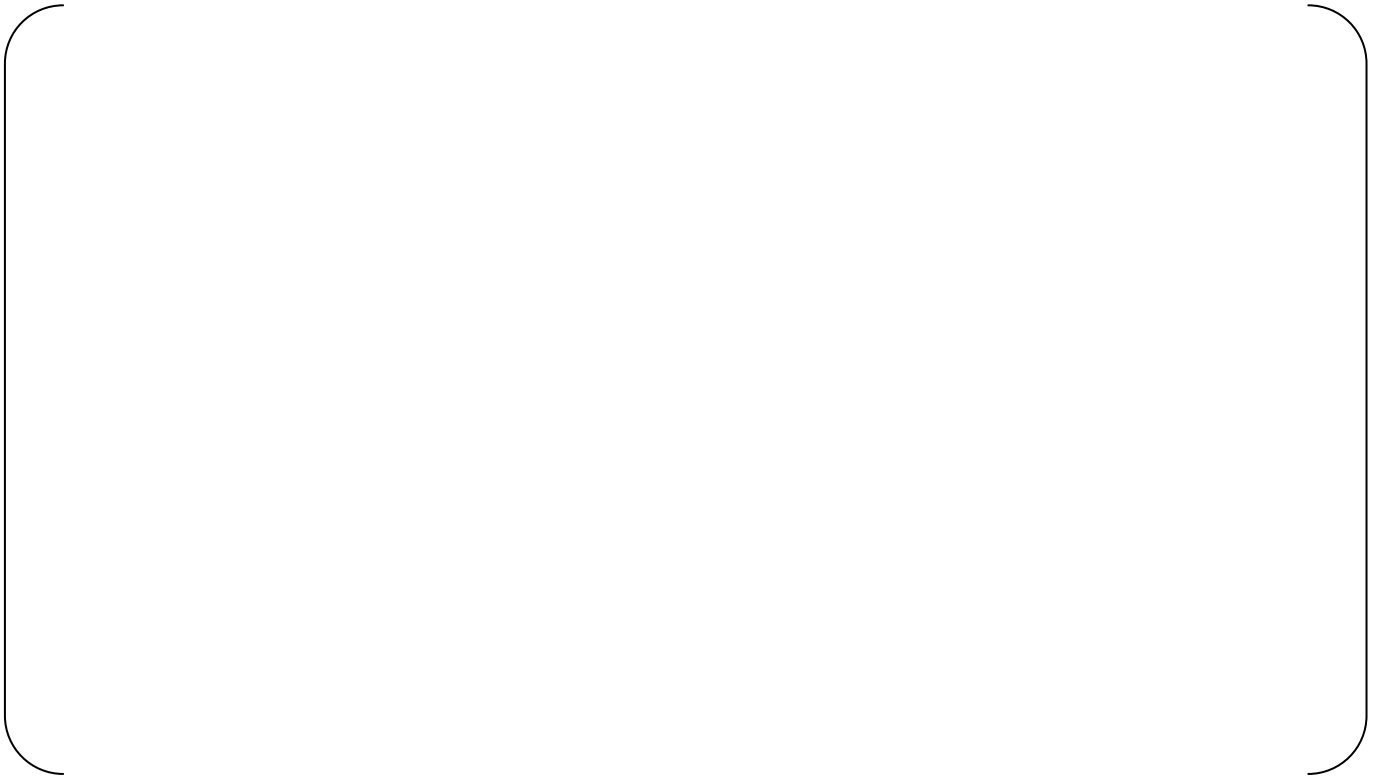


**Figure B-7-14 Plastic Strain in Steel Components of AL, Hydrogen Burn Condition, Internal View, 251.7 psig Pressure**



**Figure B-7-15 Contact Pressure in Flanges for AL, Hydrogen Burn Condition, 251.7 psig Pressure**

### B-7.5 Personnel Airlock Summary

Table B-7-1 provides a summary of the calculated pressure capacities for the various failure modes considered for the three thermal conditions. For normal operations and LTA conditions, the limiting component for the AL penetration is in the sleeve at the connection with the 6" deep vertical stiffener. For the hydrogen burn condition, the limiting component for the AL is the bulkhead front plate at the connections with the horizontal stiffeners. It is also noted that plastic strain limits in the rebar at the transition from the strengthened section develops prior to the above failures. This plastic deformation in the rebar would not itself result in pressure leakage, but leads to the tearing of the pressure boundary. The inner surface edge of the flange connection between the door and the bulkhead remains in contact, and thus prevents leakage through the seals for these limiting pressures.

**Table B-7-1 Summary of Pressure Capacities for Personnel Airlock**

Failure Mode	Failure Pressure (psig), Followed by Factor on $P_d$		
	Normal Operating Conditions	Long Term Accident Conditions	Hydrogen Burning Conditions
AL Steel Tearing	242.0	223.6	251.7
	3.56	3.29	3.70
AL Cover	>252.0	>249.6	>251.7
	>3.71	>3.67	>3.70
AL Flange Leakage	>252.0	>249.6	>251.7
	>3.71	>3.67	>3.70
AL Rebar Rupture	214.0	197.7	211.7
	3.15	2.91	3.11

## **B-8 MAIN STEAM AND FEED WATER PIPING**

### **B-8.1 Model Description**

A local, detailed 3-D model of the grouping of MS/FW piping penetration, including a portion of the PCCV wall, is used to calculate the pressure capacities that are limited by the local performance of the MS/FW piping components. The local MS/FW model uses boundary conditions extracted from the global model to impose the global deformation response on the local model.

The local modeling for the MS/FW model, including a section of the PCCV wall around the penetration, is illustrated in the following figures. Figure B-8-1 provides an overall view of the local model for the MS/FW viewed from inside containment. Figure B-8-2 provides a cut section view of one of the MS line penetrations illustrating the details of the pressure boundary. Figure B-8-3 illustrates the modeling used for the steel components of this penetration. The triangular gusset plates are approximated based on the mesh used in the concrete with an adjusted “step” pattern to provide an equivalent steel surface area. The liner and anchorage system is modeled with plate membrane elements as illustrated in Figure B-8-4. This assemblage is embedded into the concrete continuum model since the mesh for these components is different. This required that these steel components be modeled as membrane elements having only in-plane stiffness and strength. The thickened pads on the liner around the penetrations are modeled with 3-D brick elements and include a tapered edge. The local model includes the main reinforcement with tie bars and tendons as discussed in Section 5-1 for the global model. Figure B-8-5 illustrates the tendons included as embedded truss elements in the local model.

Displacement boundary conditions, extracted from the global model, are imposed on the cut sections of the PCCV wall in the local model. This enforces the deformation patterns from the global response of the containment system on the local model while capturing more refinement in the structural response of the MS/FW penetration components. A thermal analysis, using a more refined local thermal model consistent with that performed for the global model, is performed for the local model to establish the temperature distributions in the refined mesh of the local model. In this case the thermal model includes the insulation around the piping and radiation effects in the space between the pipes and sleeve. The thermal and pressure loads are incrementally applied in coordination with the displacement boundary conditions for the same loading states in the global model to evaluate the failure modes and failure pressure levels of the MS/FW penetration components.



**Figure B-8-1 Illustration of MS/FW Local Model, View from Inside**



**Figure B-8-2 Illustration of MS/FW Local Model, Cut Section View**



**Figure B-8-3 Illustration of Modeling for Steel Components in MS/FW Local Model**



**Figure B-8-4 Illustration of modeling for liner and anchorages in MS/FW Local Model**



**Figure B-8-5 Illustration of modeling for Tendons in MS/FW Local Model**

## B-8.2 Analyses for Normal Operating Conditions

The temperature distributions associated with normal operating conditions for the local MS/FW model are illustrated Figure B-8-6. The temperature distribution for the normal operating thermal condition is based on a steady state solution with the PCCV atmosphere at 105 °F and the exterior surfaces corresponding to extreme winter ambient conditions with the air temperature inside the reactor building at 50 °F. The temperature inside the pipes is 575.9 °F, and the temperature inside the sleeve is calculated based on insulation around the pipe and radiation effects.

Figure B-8-7 illustrates the distribution of plastic strain in the steel components of the MS/FW piping penetrations for normal operating conditions at a pressure of 240 psig. This plot indicates that tearing of these steel components is not the limiting condition for this penetration. Figure B-8-8 is a plot showing contours of the concrete shear strain around this anchorage at 236 psig. Coupled with yielding in the tendons, the pressure capacity for the MS/FW penetration is limited by the concrete and anchorage and will fail as a punching shear type failure before reaching plastic strain limits in the steel components. This failure pressure is determined to be 236 psig.



**Figure B-8-6 Temperature Distribution in MS/FW, Normal Operating Condition**

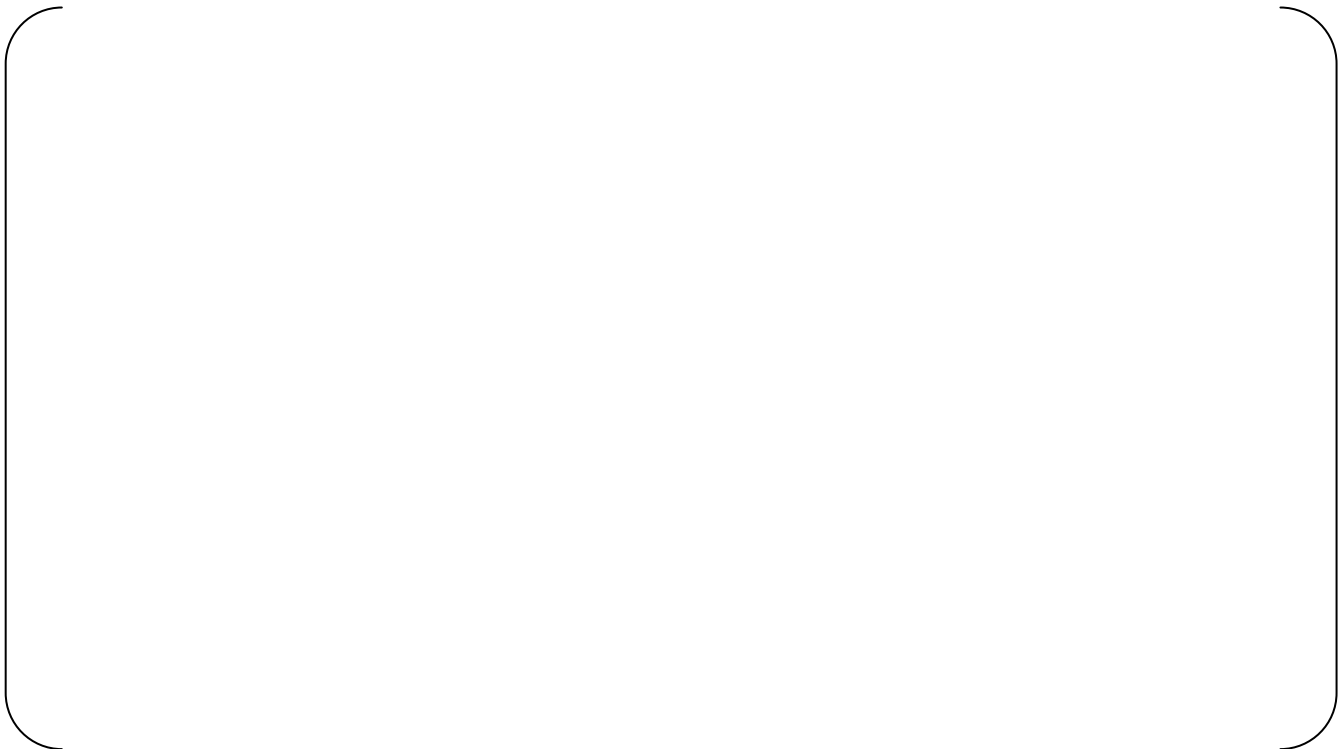


**Figure B-8-7 Plastic Strain in Steel Components of MS/FW, Normal Operating Condition, 240 psig Pressure**



**Figure B-8-8 Concrete Shear Strain at MS/FW, Normal Operating Condition, 236 psig Pressure**

### **B-8.3 Analyses for Long Term Accident Conditions**

The temperature distributions associated with LTA conditions for the local MS/FW model are illustrated Figure B-8-9. Figure B-8-10 illustrates the distribution of plastic strain in the steel components of the MS/FW piping penetrations for the LTA condition at a pressure of 249.6 psig. This plot indicates that tearing of these steel components is not the limiting condition for this penetration. Figure B-8-11 is a plot showing contours of the concrete shear strain around this anchorage at 217.6 psig. Coupled with yielding in the tendons, the pressure capacity for the MS/FW penetration is limited by the concrete and anchorage and will fail as a punching shear type failure before reaching plastic strain limits in the steel components. This failure pressure is determined to be 217.6 psig.



**Figure B-8-9 Temperature Distribution in MS/FW, LTA Condition**



**Figure B-8-10 Plastic Strain in Steel Components of MS/FW, LTA Condition, 249.6 psig Pressure**



**Figure B-8-11 Concrete Shear Strain at MS/FW, LTA Condition, 217.6 psig Pressure**

#### **B-8.4 Analyses for Hydrogen Burn Conditions**

Figure B-8-12 illustrates the temperature distribution for the hydrogen burn accident condition. Figure B-8-13 provides a contour plot for plastic strain in the steel components at a pressure of 251.7 psig. Figure B-8-14 illustrates the distribution of shear strain in the concrete wall of the containment around the MS/FW penetrations for the hydrogen burn condition at a pressure of 229.7 psig. Similar to the normal operating and LTA scenarios the pressure capacity for the MS/FW penetration is limited by the concrete and anchorage characterized by a punching shear type failure.



**Figure B-8-12 Temperature Distribution in MS/FW, Hydrogen Burn Condition**



**Figure B-8-13 Plastic Strain in Steel Components of MS/FW, Hydrogen Burn Condition, 251.7 psig Pressure**



**Figure B-8-14 Concrete Shear Strains at MS/FW, Hydrogen Burn Condition, 229.7 psig Pressure**

### B-8.5 MS/FW Piping Penetrations Summary

Table B-8-1 provides a summary of the calculated pressure capacities for the various failure modes considered for the three thermal conditions for the MS and FW penetrations. The governing failure mechanism for the MS/FW penetrations is loss of anchorage due to excessive concrete shear strain. It is noted that tendon rupture due to high plastic strains develop just prior to meeting the criteria for concrete shear failure. Tendon failure in itself does not constitute a failure of the pressure boundary, but allows progressive and rapid failure in the anchorage which will breach the pressure boundary.

**Table B-8-1 Summary of Pressure Capacities for Main Steam and Feedwater Piping**

Failure Mode	Failure Pressure (psig), Followed by Factor on $P_d$		
	Normal Operating Conditions	Long Term Accident Conditions	Hydrogen Burning Conditions
MS/FW Steel Tearing	> 240.0	249.6	> 251.7
	> 3.53	3.67	> 3.70
MS/FW concrete shear/anchorage	236.0	217.6	229.7
	3.47	3.20	3.38
MS/FW Tendon Strain	226.0	211.6	225.7
	3.32	3.11	3.32

## **B-9 FUEL TRANSFER TUBE**

### **B-9.1 Model Description**

A local, detailed 3-D model of the FTT penetration including a portion of the PCCV wall is used to calculate the pressure capacities that are limited by the local performance of the FTT components. The local FTT model uses boundary conditions extracted from the global model to impose the global deformation response on the local model. The FTT closure cap is a pressure-seating design with a flat plate in contact with heavy flanges.

The local modeling for the FTT model, including a section of the PCCV wall around the penetration, is illustrated in the following figures. Figure B-9-1 and B-9-2 provide an overall view of the local model for the FTT viewed from inside and outside, respectively. The liner and anchorage system is modeled with plate membrane elements in the same way as the MS/FW local model. Figure B-9-3 provides a cut section view illustrating the details of the pressure boundary. Figure B-9-4 provides a view of the modeling used for the steel components of this penetration. Spring elements are used to provide support for the end extending into containment to represent the 3-point support provided by the containment internal structure. The seal is provided by a bolted connection holding the flat closure plate in contact with the mating flanges compressing O-ring type gaskets. A contact surface between the flanges is used to allow flange slippage or separation to develop as appropriate. The bolts were modeled with beam elements connected to the outer surfaces of the cover plate and the flange. An initial stress of 1187 psi was applied to these beam elements to develop a pre-load corresponding to a tightening torque of 30 N-m. Separation of the inner surface of the flanges is used as the metric in determining pressure capacity for seal leakage as a failure mechanism. The local model includes the main reinforcement with tie bars and tendons as discussed in Section 5-1 for the global model. Displacement boundary conditions, extracted from the global model, are imposed on the cut sections of the PCCV wall in the local model. This enforces the deformation patterns from the global response of the containment system on the local model while capturing more refinement in the structural response of the FTT components. A thermal analysis, using a more refined local thermal model consistent with that performed for the global model, is performed for the local model to establish the temperature distributions in the refined mesh of the local model. The thermal and pressure loads are incrementally applied in coordination with the displacement boundary conditions for the same loading states in the global model to evaluate the failure modes and failure pressure levels for the FTT components.



**Figure B-9-1 Illustration of FTT Local Model, View from Inside**



**Figure B-9-2 Illustration of FTT Local Model, View from Outside**



**Figure B-9-3 Illustration of FTT Local Model, Cut Section View**



**Figure B-9-4 Illustration of FTT Local Model, View of Steel Components**

## **B-9.2 Analyses for Normal Operating Conditions**

The temperature distributions associated with normal operating condition for the local FTT model are illustrated in Figure B-9-5. Figure B-9-6 illustrates the distribution of plastic strain in the steel components of the FTT for normal operating conditions at a pressure of 241 psig. Figure B-9-7 illustrates the distribution of shear strain in the concrete wall of the containment around the FTT for normal operating conditions at a pressure of 241 psig. Figure B-9-6 would indicate that the limiting pressure condition is in the anchor plate and in the sleeve but this develops concurrently with the large shear strain through the concrete wall. Thus, the limiting mechanism for this penetration is failure of the concrete section in a punching shear mode and loss of anchorage for the FTT.



**Figure B-9-5 Temperature Distribution in FTT, Normal Operating Condition**



**Figure B-9-6 Plastic Strain in Steel Components of FFT, Normal Operating Condition, 241 psig Pressure**



**Figure B-9-7 Concrete Shear Strain at FFT Penetration, Normal Operating Condition, 241 psig Pressure**

### **B-9.3 Analyses for Long Term Accident Conditions**

The temperature distributions associated with LTA conditions for the local FTT model are illustrated Figure B-9-8. Figure B-9-9 illustrates the distribution of plastic strain in the steel components of the FTT for LTA conditions at a pressure of 249.6 psig. Figure B-9-10 is a plot showing contours of the concrete shear strain around this anchorage at 239.6 psig. This plot indicates that the pressure capacity for the FTT penetration is limited by the concrete and anchorage. Figure B-9-11 is a plot showing contours contact pressure between the FTT cover plate and the blind flange at 249.6 psig. Positive contact pressure is maintained throughout the entire analysis indicating there is no leakage at this location.



**Figure B-9-8 Temperature Distribution in FTT, LTA Condition**



**Figure B-9-9 Plastic Strain in Steel Components of FTT, LTA Condition, 249.6 psig Pressure**



**Figure B-9-10 Concrete Shear Strain at FFT Penetration, LTA Condition, 239.6 psig Pressure**



**Figure B-9-11 FFT Flange Cover Contact Pressure, LTA Condition, 249.6 psig Pressure**

#### **B-9.4 Analyses for Hydrogen Burn Conditions**

Figure B-9-2 illustrates the temperature distribution for the hydrogen burn accident condition showing a slice through the section. Figure B-9-13 provides a contour plot for plastic strain in the steel components. Figure B-9-14 illustrates the distribution of shear strain in the concrete wall of the containment around the FTT for the Hydrogen Burn conditions at a pressure of 244.9 psig.



**Figure B-9-12 Temperature Distribution in FTT, Hydrogen Burn Condition**



**Figure B-9-13 Plastic Strain in Steel Components of FTT, Hydrogen Burn Condition, 244.9 psig Pressure**



**Figure B-9-14 Concrete Shear Strain around FTT, Hydrogen Burn Condition, 244.9 psig Pressure**

### B-9.5 Fuel Transfer Tube Summary

Table B-9-1 provides a summary of the calculated pressure capacities for the various failure modes considered for the three thermal conditions for the FTT. The pressure capacity for the LTA is due to concrete shear failure and loss of anchorage. This is attributed to the thick steel sections, relatively simple anchorage details, and the small diameter penetration that limits the shear area in the concrete. It is noted that tendon rupture develops just prior to meeting the criteria for concrete shear failure. Tendon failure in itself does not constitute a failure of the pressure boundary, but allows progressive and rapid failure in the anchorage which will breach the pressure boundary. These analyses show that the flanges remain in contact past the pressure where other leakage would result and thus leakage through the seal is not a limiting condition.

**Table B-9-1 Summary of Pressure Capacities for Fuel Transfer Tube**

Failure Mode	Failure Pressure (psig), Followed by Factor on $P_d$		
	Normal Operating Conditions	Long Term Accident Conditions	Hydrogen Burning Conditions
FTT Steel Tearing	241.0	> 249.6	244.9
	3.54	> 3.67	3.60
FTT Flange Leakage	> 251.6	> 249.6	> 251.6
	> 3.70	> 3.67	> 3.70
FTT Concrete Shear/Anchorage	241.0	239.6	244.9
	3.54	3.52	3.60
FTT Tendon Failure	240.0	235.6	237.5
	3.53	3.46	3.49

## **APPENDIX C**

# **Containment Pressure Evaluation for More Likely Severe Accident Challenges**

**TABLE OF CONTENTS**

<b>C-1 BACKGROUND .....</b>	<b>206</b>
<b>C-2 MORE LIKELY SEVERE ACCIDENT CHALLENGES .....</b>	<b>206</b>
<b>C-3 CONTAINMENT PRESSURE EVALUATION.....</b>	<b>207</b>
<b>C-3.1 Case 1: Containment Spray System Available .....</b>	<b>207</b>
<b>C-3.2 Case 2: Alternate Containment Cooling Available .....</b>	<b>207</b>
<b>C-4 CONCLUSION .....</b>	<b>213</b>
<b>C-5 REFERENCE .....</b>	<b>213</b>

**LIST OF FIGURES**

Figure C- 1	Containment pressure history within 10 hours after accident initiation (Case 1: Containment spray system available).....	209
Figure C- 2	Containment pressure history within 50 hours after accident initiation (Case 1: Containment spray system available).....	209
Figure C- 3	Containment temperature history within 10 hours after accident initiation (Case 1: Containment spray system available).....	210
Figure C- 4	Containment temperature history within 50 hours after accident initiation (Case 1: Containment spray system available).....	210
Figure C- 5	Containment pressure history within 10 hours after accident initiation (Case 2: Alternate containment cooling available).....	211
Figure C- 6	Containment pressure history within 50 hours after accident initiation (Case 2: Alternate containment cooling available).....	211
Figure C- 7	Containment temperature history within 10 hours after accident initiation (Case 2: Alternate containment cooling available).....	212
Figure C- 8	Containment temperature history within 50 hours after accident initiation (Case 2: Alternate containment cooling available).....	212

## **C-1 BACKGROUND**

The U.S. Nuclear Regulatory Commission (NRC) has issued Regulatory Guide (RG) 1.216 in August 2010(Reference C-5.1 ). This regulatory guide describes the methods that the NRC staff considers acceptable for predicting the internal pressure capacity for containment structures above the design-basis accident pressure.

This document provides the containment pressure evaluation results to satisfy the NRC staff's specification described in Reference C-5.1 .

## **C-2 MORE LIKELY SEVERE ACCIDENT CHALLENGES**

In Reference C-5.1 the NRC staff requires the applicant to provide the technical basis for identifying the more likely severe accident challenges. The NRC presents an example of an acceptable way to identify the more likely severe accident challenges in Reference C-5.1 as

*“to consider the sequences or plant damage states that, when ordered by percentage contribution, represent 90 percent or more of the core damage frequency.”*

The US-APWR probabilistic risk assessment (PRA) evaluation, documented in Reference C-5.2 , shows that the frequency of containment failure scenarios is approximately 10% of the frequency of core damage scenarios. This means that the containment is appropriately cooled and maintains its integrity for 90% of the severe accidents, i.e., the more likely severe accident challenges are the cases that containment cooling is functional.

For the US-APWR design, two diverse containment depressurization functions are provided, one is the containment spray system and the other is the alternate containment cooling. Therefore the more likely severe accident scenario can be considered either one of the containment depressurization functions are available.

### C-3 CONTAINMENT PRESSURE EVALUATION

#### C-3.1 Case 1: Containment Spray System Available

Following accident sequence is evaluated as the representative this likely severe accident case.

- Accident sequence: Small break LOCA (equivalent to 2in diameter break)
  - + 0/4 high head injection
  - + 4/4 accumulators
  - + 4/4 containment spray system
  - + reactor coolant system (RCS) depressurization valve (DV) open 30minutes after core damage

Containment pressure history within 10 hours and 50 hours are shown in Figure C-1 and Figure C-2, respectively. In addition, containment temperature history within 10 hours and 50 hours are shown in Figure C-3and Figure C-4, respectively.

Core damages at 2.1 hours and accordingly the RCS DVs are opened at 2.6 hours. Containment pressurization is accelerated due to opening the DVs because RCS inventory is released into the containment atmosphere. The containment pressure reaches the containment spray set point at 2.8 hours and the containment spray is initiated. Containment is depressurized accordingly. Containment is pressurized when molten core material relocates to the lower head at 4.7 hours and the reactor vessel fails at 7.6 hours, although these pressurizations are not significant to be a challenge against the containment integrity. After reactor vessel failure, containment pressure is maintained approximately 20 psia due to operation of the containment spray system. The containment temperature history shows very similar transition with the pressure history, in accordance with the occurrence of accidental events.

The containment pressure and temperature are maintained below the design pressure of 83 psia and design temperature of 300°F throughout the accident progression for this likely severe accident scenario.

#### C-3.2 Case 2: Alternate Containment Cooling Available

Following accident sequence is evaluated as the representative this likely severe accident case.

- Accident sequence: Small break LOCA (equivalent to 2in diameter break)
  - + 0/4 high head injection
  - + 4/4 accumulators
  - + 0/4 containment spray system
  - + reactor cavity injection initiated 10 minutes after core damage
  - + RCS DV open 30 minutes after core damage
  - + Alternate containment cooling initiated 30 minutes after containment exceeds the design pressure

Containment pressure history within 10 hours and 50 hours are shown in Figure C-5 and Figure C-6 respectively. In addition, containment temperature history within 10 hours and 50 hours are shown in Figure C-7 and Figure C-8, respectively.

Core damages at 2.1 hours so that the reactor cavity injection is initiated at 2.3 hours and the RCS DVs are opened at 2.6 hours. Containment pressurization is accelerated due to opening the DVs because RCS inventory is released into the containment atmosphere. Containment pressurization is slightly accelerated when molten core material relocates to the lower head at 4.7 hours, although this pressurization is not significant to be a challenge against the containment integrity. Containment pressure reaches the first peak at approximately 6.5 hours and then it gradually decreases. It is because the RCS inventory dries out at this time and hence no additional steam is released to the containment. Heat transfer to the containment heat sink becomes greater than heat generation because of the decay heat, so that containment is temporarily depressurized. Reactor vessel fails at 7.2 hours, although the depressurization trend is maintained until approximately 13 hours, containment heat sink is sufficiently heated up. After that, containment pressure again increases up to the set point of the alternate containment cooling, the design pressure of 83 psia, at 39 hours. After the alternate containment cooling is initiated, the containment pressure gradually decreases below the design pressure. The containment temperature history shows very similar transition with the pressure history, in accordance with the occurrence of accidental events.

For this likely severe accident scenario, the containment pressure is maintained below the design pressure of 83 psia and design temperature of 300°F before 24 hours following the onset of core damage. The containment pressure and temperature reaches slightly above the design pressure and temperature following the initial 24 hours after onset of core damage. However it is immediately reduced below the design pressure and temperature after initiating the alternate containment cooling. In addition, the alternate containment cooling can be initiated before the containment condition exceeds the design pressure and temperature, so that it is achievable to maintain the containment conditions below the design pressure and temperature for this accident scenario.

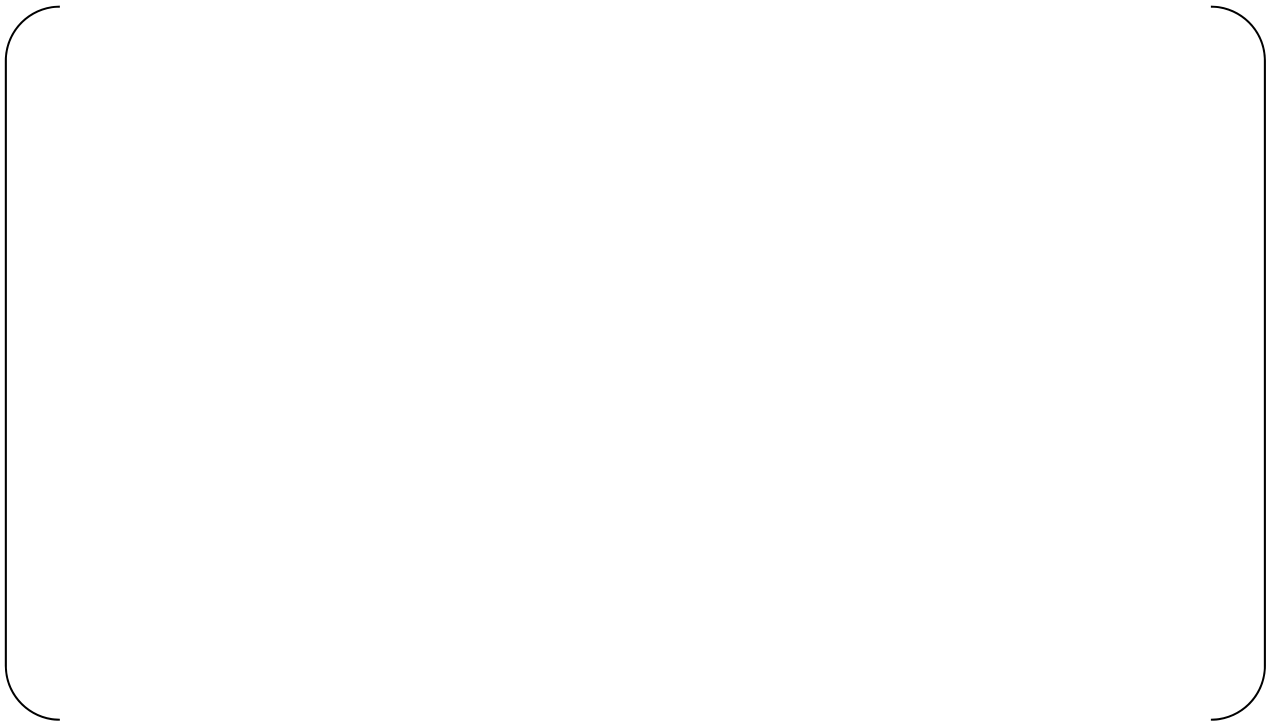


**Figure C-1** Containment pressure history within 10 hours after accident initiation  
(Case 1: Containment spray system available)



**Figure C-2** Containment pressure history within 50 hours after accident initiation  
(Case 1: Containment spray system available)



**Figure C-3** Containment temperature history within 10 hours after accident initiation  
(Case 1: Containment spray system available)



**Figure C-4** Containment temperature history within 50 hours after accident initiation  
(Case 1: Containment spray system available)

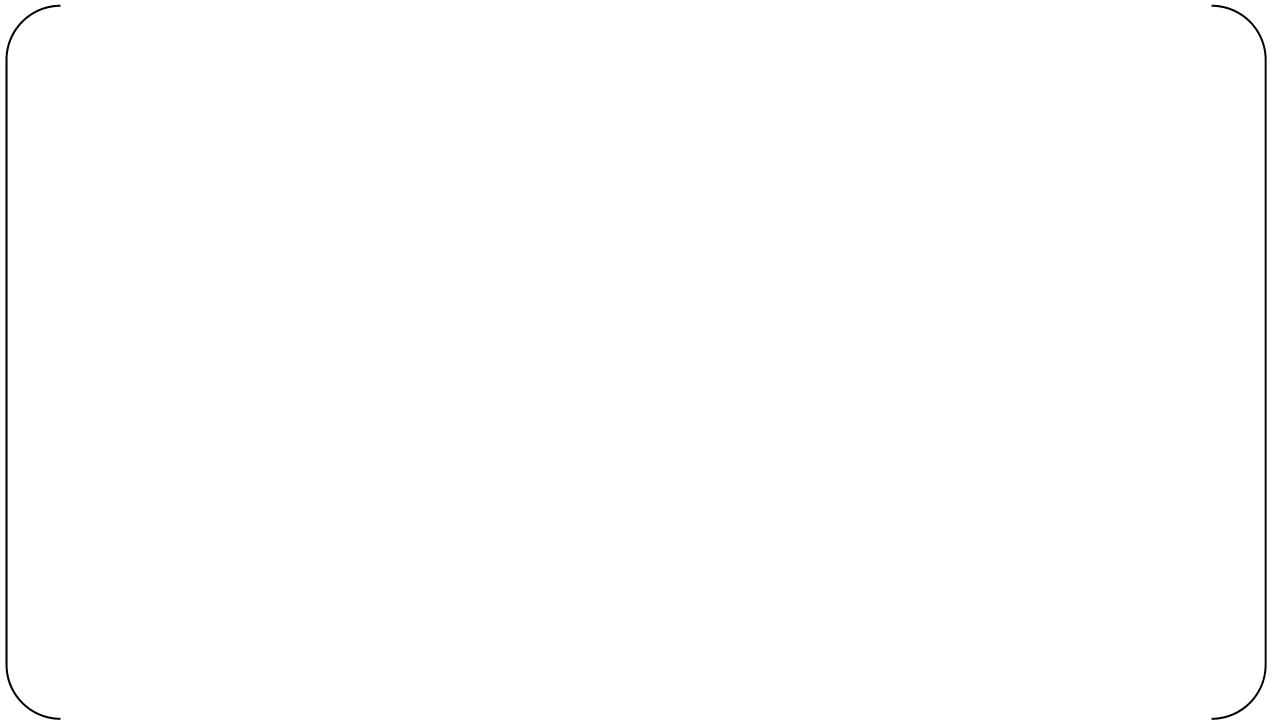


**Figure C-5** Containment pressure history within 10 hours after accident initiation  
(Case 2: Alternate containment cooling available)



**Figure C-6** Containment pressure history within 50 hours after accident initiation  
(Case 2: Alternate containment cooling available)



**Figure C-7** Containment temperature history within 10 hours after accident initiation  
(Case 2: Alternate containment cooling available)

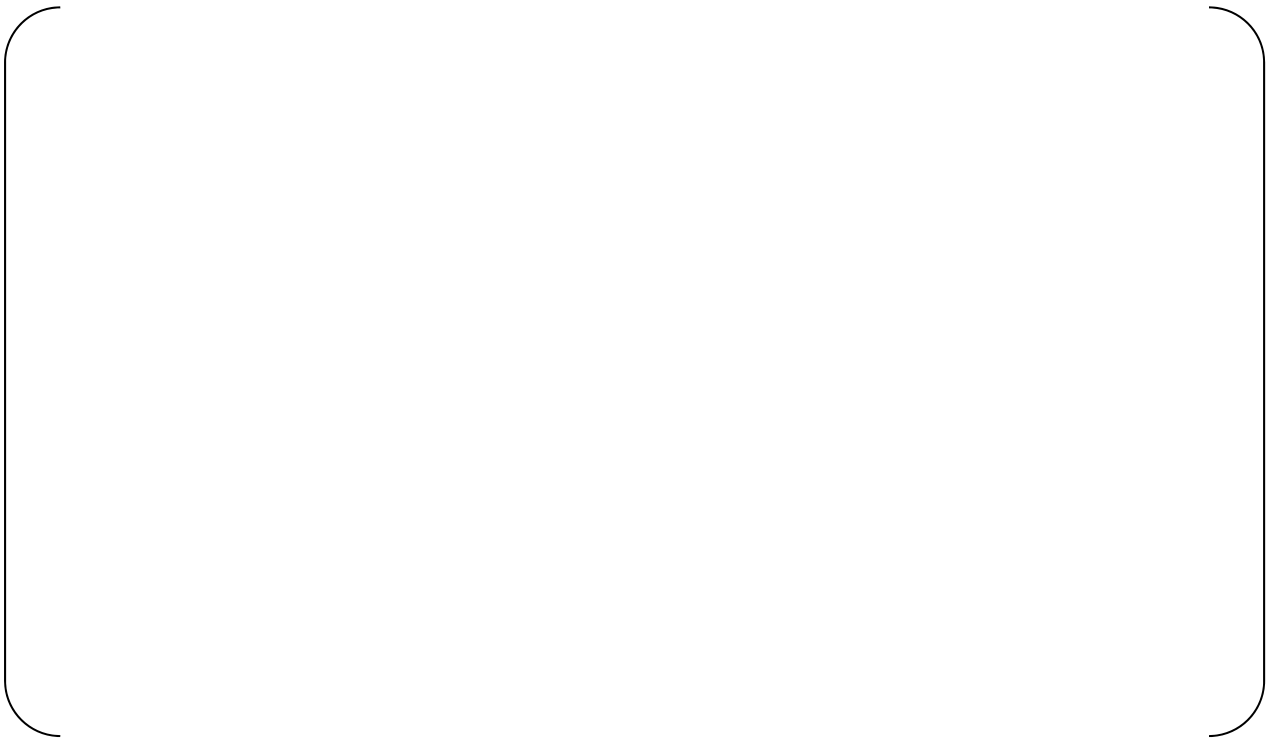


**Figure C-8** Containment temperature history within 50 hours after accident initiation  
(Case 2: Alternate containment cooling available)

**C-4 CONCLUSION**

The more likely severe accident challenges for the US-APWR are the cases that containment depressurization functions are available in accordance with the US-APWR PRA evaluation. The containment condition is maintained below the design pressure and temperature within the 24 hours after onset of core damage as well as the period following initial 24 hours after the onset of core damage for these more likely severe accident challenges.

**C-5 REFERENCES**

- C-5.1** Regulatory Guide 1.216, "Containment Structural Integrity Evaluation for Internal Pressure Loading above Design-basis Pressure," August 2010
- C-5.2** US-APWR Probabilistic Risk Assessment, MUAP-07030 Rev. 3, June 2011